ANALYSIS OF COLLISION CASCADES IN TITANIUM DEUTERIDE BY D–D FUSION

Thesis by

Thomas Wilson Workman

In Partial Fulfillment of the Requirements
for the Degree of
Doctor of Philosophy

California Institute of Technology
Pasadena, California

1992
(Defended May 18, 1992)

To Kimi

ACKNOWLEDGEMENT

First and foremost, I wish to thank Professor Marc-A. Nicolet. His support, inspiration, and guidance have made my undergraduate and graduate study at Caltech a very rewarding experience.

Dr. W. L. Johnson was instrumental in the conceptualization of the experiments leading up to this thesis. Dr. C. A. Barnes gave valuable guidance in the matters of nuclear physics and contributed ideas as to additional areas of exploration with D–D fusion.

I would like to thank the members of Professor Nicolet's group, past and present, especially Drs. Y-T. Cheng, and T. Banwell, who taught me the basics of ion-solid interactions; also Dr. E. Kolawa, Dr. G. Bai, and J.S. Chen, who have contributed, through either collaborations or casual conversations, to the completion of this thesis. Particular acknowledgments are due to Dr. H. Fecht, who helped with the early work in creating titanium hydride thin films and to Chang Liu, who lead me through the process of fabricating Si_3N_4 filters. For their technical assistance, I am indebted to B. Stevens, M. Easterbrook, D. Groseth, and most especially, R. Gorris, who built, modified, or cajoled into working every piece of equipment I have utilized in the performance of this work.

I am grateful for the encouragement and support of my parents, who pointed me in the right direction and then let me make my own decisions.

Finally, I wish to express my utmost appreciation to my wife, Kimi, for her unconditional love and support during my long study, her indulgence of my scientist's ways, and her great help in the preparation of this manuscript.

ABSTRACT

As a test of the linear binary collision cascade model for ion-solid interaction, theoretical models of D–D fusion induced by heavy ion irradiation of titanium deuteride are compared with experimental results. Thin-film titanium deuteride samples of composition $TiD_{1.7}$ were prepared by heating 320 nm titanium films on silicon dioxide in a static pressure of deuterium. The deuterium content of these films was inferred from changes in the titanium and oxygen contaminant signals measured by 3.05 MeV oxygen-resonance backscattering spectrometry.

The titanium deuteride samples were irradiated with beams of argon and xenon ions with energies ranging from 140 to 600 keV. The energy of the incident ion was transferred to atoms in the sample through a series of nuclear collisions, resulting in deuteron–deuteron collisions with energies up to tens of keV. The cross sections for D–D fusion at these energies are large enough for fusion events to be detected for doses above 10^{14} ions. A silicon surface-barrier detector placed at an angle of 130° with respect to the incident ion beam was used to monitor the 3.02 MeV protons and 1.01 MeV tritons from the D(d,p)T reaction and 0.82 MeV ^{3}He ions from the D(d,n)^{3}He reaction. Fusion yields (fusion events per incident ion) ranging from 10^{-14} to 10^{-10} were measured.

A linear binary collision cascade model is presented which predicts fusion yields which are in excellent agreement with the measured yields for all cases studied. The model predicts a distribution of deuteron–deuteron center-of-mass velocities which causes a distribution of Doppler shifts in the spectrum of the fusion products. The shape of the theoretical proton signals based on the model is a reasonably good fit to the experimental proton signals.

The use of D–D fusion induced by heavy-ion irradiation for measuring deuterium concentrations is compared with currently used methods and is found to be somewhat less sensitive than nuclear reaction analysis, but suitable for measuring deuterium concentrations as low as 2 atomic percent with ion beams producible by ion implanters with an energy range of a few hundred kV.

TABLE OF CONTENTS

Acknowledgement iii

Abstract iv

Table of Contents vi

List of Figures viii

List of Publications xiv

Chapter 1 Introduction 1

- 1.1 Origin of Experiment 1
- 1.2 The Collision Cascade 4
- 1.3 The D–D Reaction 9

Chapter 2 Sample Preparation and Characterization 19

- 2.1 Fabrication of TiD Thin Films 19
- 2.2 Backscattering Analysis of TiD Thin Films 27
  - 2.2.1 Oxygen Resonance for Determination of Oxygen Concentration 27
  - 2.2.2 Determination of Deuterium Concentration 34
- 2.3 X-ray Diffraction Analysis 38

Chapter 3 Experimental Procedures and Results 42

- 3.1 Experimental Setup 42
- 3.2 Experimental Procedures 48
- 3.3 Experimental Results 52
  - 3.3.1 Al Filter Results 52
  - 3.3.2 Si_3N_4 Results 57

Chapter 4 Binary Collision Cascade Model of Fusion Yield 64
4.1 Introduction 64
4.2 Representation of the Collision Cascade 65
4.3 Calculation of the Fusion Yield of a Chain 67
4.4 Algorithms Used to Compute Fusion Yields 70
4.5 Results and Comparison with Experiment 72
4.5.1 Model Results for Xe Irradiation 73
4.5.2 Model Results for Ar Irradiation 76
4.5.3 Comparison of Model with Experiment 78
Chapter 5 Doppler Analysis of Peak Shapes 83
5.1 Processes Affecting Peak Shape 84
5.2 Modeling the Deuteron Energy Spectrum 85
5.3 Model Results 89
5.4 Calculation of the Doppler Shift 94
5.5 Comparison with Experiment 98
Chapter 6 Considerations on Applications to Materials Analysis 102
6.1 Comparison with Existing Techniques 102
6.2 Optimum Parameters for Measuring Deuterium Concentration 104
Appendix 1 Fabrication of Thin Si_3N_4 Filters 111
Appendix 2 FORTRAN Program Used to Calculate Fusion Yields 114

LIST OF FIGURES

Fig. 1.1 The interatomic potential for D–D interaction. For $r < R$ the deep negative potential is due to the strong nuclear force. For $r > R$ the coulomb and centrifugal potentials present a barrier which must be penetrated for a reaction to occur (taken from [24]). 12

Fig. 1.2 Experimental $S(E)$-factor data for the reactions (a) D(d,p)T and (b) D(d,n)^{3}He. The solid curves are the results of polynomial fits to the data for E_{CM} $\leq$120 keV (taken from [25]). 14

Fig. 1.3 Angular distributions at representative energies for D(d,p)T and D(d,n)^{3}He reactions. The solid curves through the data points are the results of χ^2 analysis using even Legendre polynomials (taken from [25]). 15

Fig. 2.1 Pressure-composition isotherms for the Ti–H system. 21

Fig. 2.2 Schematic of furnace system used for hydiding and deuteriding Ti samples. 22

Fig. 2.3a 3.08 MeV He^{++} backscattering spectra of sample Ti10 before and after deuteridation, with the 3.05 MeV oxygen resonance occurring at a depth of 80 nm. 32

Fig. 2.3b Background subtracted oxygen signals (data points) and Gaussian fits to oxygen resonance signals (lines) for the spectra shown in Fig. 2.3a. 32

Fig. 2.4 Oxygen concentration as a function of (assumed) deuterium concentration for sample Ti10 based on the peak height of the oxygen resonance signal and Eq. 2.6. The two dashed lines delineate the range of uncertainty in y. 33

Fig. 2.5 2 MeV RBS spectrum of sample Ti10 (tilted 20°) before and after deuteridation. Ti signal height decreases and width increases due to the energy absorption of deuterium. 36

Fig. 2.6 Intersection of Eq. 2.6 and Eq. 2.10 which determines oxygen and deuterium concentrations for sample Ti10. The intersection point indicates a composition of $Ti_{0.36}D_{0.63}O_{0.01}$. The dashed lines delineate the range of uncertainty for each equation. 37

Fig. 2.7 Ti–H phase diagram. The hydrogen concentration as determined by backscattering analysis (61±2 at%) is near the border between the fcc δ phase and the fct ε phase. 39

Fig. 2.8a X-ray spectrum of pure Ti sample before hydridation. 40

Fig. 2.8b X-ray spectrum of Ti sample after hydridation to $TiH_{1.7}$. The peaks are consistent with an fcc structure with a lattice parameter of 4.530 Å. 40

Fig. 3.1 Schematic of 400MPR Ion Implanter used for ion irradiation. 43

Fig. 3.2 Top and side views of detector–sample geometry. 45

Fig. 3.3a Background spectrum taken with no beam and no $TiD_{1.7}$ sample over a duration of 14 hours. Background count rate = 18 counts/hour. 51

Fig. 3.3b Background spectrum taken during 250 keV Xe^+ irradiation of $TiH_{1.7}$. Total ion dose = 6.0×10^{16} ions over a duration of 75 minutes. Background count rate = 15 counts/hour. 51

Fig. 3.4 Spectrum obtained by irradiating $TiD_{1.7}$ with 5.12×10^{16} 400 keV Ar^{++} ions over a duration of 5.5 hours. A 5 μm Al filter was placed in front of the detector to block sputtered and backscattered particles. The detector was placed at an angle of 129° from the incident beam direction and subtended a solid angle of 44.1 mSr. 53

Fig. 3.5 Record of ion dose and proton and triton counts taken during 400 keV Ar^{++} irradiation of $TiD_{1.7}$. 55

Fig. 3.6 Spectrum obtained by irradiating $TiD_{1.7}$ with 1.53×10^{16} 500 keV Xe^{++} ions over a duration of 3 hours. A 540 nm Si_3N_4 filter was placed in front of the detector to block sputtered and backscattered particles. The filter was thin enough to allow the 0.82 MeV ^{3}He to reach the detector. The detector was placed at an angle of 130° from the incident beam direction and subtended a solid angle of 50.8 mSr. 58

Fig. 3.7 Record of ion dose and proton, triton, and ^{3}He counts taken during 500 keV Xe^{++} irradiation of $TiD_{1.7}$. 59

Fig. 3.8 Experimental fusion yields for Ar and Xe irradiation of $TiD_{1.7}$ using an Al filter (○) or a Si_3N_4 filter (△) in front of the detector. 62

Fig. 4.1a Theoretical fusion yields for the first three generations of recoils for Xe irradiation of $TiD_{1.7}$. The dotted line is the highest yield for 4th generation recoils ($Y_{\mathrm{XeTiTiTiDD}}$). 74

Fig. 4.1b The relative contributions ($>10^{-6}$) to the total fusion yield for the chains shown in Fig 4.1a. 74

Fig. 4.2a Theoretical fusion yields for the first three generations of recoils for Ar irradiation of $\mathrm{TiD}_{1.7}$. The dotted line is the highest yield for 4^{th} generation recoils ($Y_{\mathrm{ArTiTiTiDD}}$). 77

Fig. 4.2b The relative contributions ($>10^{-6}$) to the total fusion yield for the chains shown in Fig 4.2a. 77

Fig. 4.3a Comparison of theoretical fusion yields for six different interatomic potentials (lines) and experimental fusion yields (data points) for Ar irradiation of $\mathrm{TiD}_{1.7}$. 79

Fig. 4.3b Comparison of theoretical fusion yields for six different interatomic potentials (lines) and experimental fusion yields (data points) for Xe irradiation of $\mathrm{TiD}_{1.7}$. 79

Fig. 4.4 Comparison of theoretical (lines) and experimental (data points) fusion yields for Ar and Xe irradiation of $\mathrm{TiD}_{1.7}$. Theoretical yields were calculated using the Thomas-Fermi-Sommerfeld interatomic potential, which gives the best fit to the experimental data. 80

Fig. 5.1 Comparison of theoretical and experimental fusion spectra for 500 keV Xe^{++} irradiation of $\mathrm{TiD}_{1.7}$. Theoretical yields assume monoenergetic beams of 3.02 MeV protons, 1.01 MeV tritons, and 0.82 MeV ^{3}He ions emitted from the sample surface convoluted with the detected energy loss distribution of Table 5.1. The area under each theoretical signal is equal to the area under the corresponding experimental signal. 86

Fig. 5.2a Theoretical deuteron energy distributions for 600 keV Ar^{++} irradiation for the three chains giving the largest contribution to the total fusion yield. 91

Fig. 5.2b Theoretical deuteron energy distributions for 200 keV Xe^{+} irradiation for the three chains giving the largest contribution to the total fusion yield. The maximum deuteron energy for the Xe–D chain is 11.9 keV. 91

Fig. 5.3 Theoretical fusion yield as a function of deuteron energy at the time of fusion for Ar irradiation at the energies used in the experiment. Each peak is dominated by the Ar–D–D chain contribution to greater than 99.2%. 92

Fig. 5.4a Theoretical fusion yield as a function of deuteron energy at the time of fusion for Xe irradiation at the energies used in the experiment. The high energy tails are due to the Xe–Ti–D–D chain contribution. 93

Fig. 5.4b Enlarged view of the fusion yield for 200 keV Xe irradiation explicitly showing the contributions of the Xe–D–D and Xe–Ti–D–D chains. 93

Fig. 5.5a Comparison of unidirectional ($\theta = 130^\circ$) and distributed angle (with 33% Nuclear Stopping) models and the experimental proton signal for 600 keV Ar^{++} irradiation. 99

Fig. 5.5b Comparison of unidirectional ($\theta = 130^\circ$) and distributed angle (with 40% Nuclear Stopping) models and the experimental proton signal for 200 keV Xe^{+} irradiation. 99

Fig. 6.1 Comparison of theoretical fusion yields for irradiation of $TiD_{1.7}$ with various ions. 105

Fig. 6.2 Theoretical fusion yields as a function of deuterium concentration for 1 MeV and 500 keV Ar and Ne ions. The detection limit for 500 keV ions is 4 at%, and for 1 MeV, it is 3 at% for Ne and 2 at% for Ar. 108

Fig. A1.1 Procedure for fabricating thin Si_3N_4 filters. 113

LIST OF PUBLICATIONS

"D(d,p)T Fusion Induced by Heavy Ion Irradiation of $TiD_{1.7}$," T. W. Workman and M-A. Nicolet, submitted to Phys. Rev. Lett. 1991.

"Ion Mixing of Metal/Al Bilayers near 77 K," E. Ma, T. W. Workman, W. L. Johnson, and M-A. Nicolet, Appl. Phys. Lett. **54**, 413 (1989).

"Interfacial Reactions of Mo with Al: Ion Mixing Versus Thermal Annealing" E. Ma, A. J. Brunner, T. W. Workman, C. W. Nieh, X.-A. Zhao, and M-A. Nicolet, Mat. Res. Soc. Symp. Proc. **100**, 75 (1988).

"Ion Beam Mixing of Amorphous Cr-Nitride / Mo-Nitride and Polycrystalline Cr/Mo Bilayers," M. Thuillard, T. W. Workman, E. Kolawa, and M-A. Nicolet, Journal of Less-Common Metals **145**, 505 (1988).

"Studies of a Phenomenological Model of Ion Mixing" Y.-T. Cheng, T. W. Workman, M-A. Nicolet, and W. L. Johnson, Mat. Res. Soc. Symp. Proc. **74**, 419 (1987).

"Effect of Thermodynamics on Ion Mixing," T. W. Workman, Y.-T. Cheng, W. L. Johnson, and M-A. Nicolet, Appl. Phys. Lett. **50**, 1485 (1987).

"Correlation Between the Cohesive Energy and the Onset of Radiation-Enhanced Diffusion in Ion Mixing," Y.-T. Cheng, X.-A. Zhao, T. Banwell, T. W. Workman, M-A. Nicolet, and W. L. Johnson, J. Appl. Phys. **60**, 2615 (1986).

"Ion Beam Modification of Corrosion and Wear Properties of Metals and Ceramics," T. W. Workman (sponsored by ITT, presented Fall 1985).

Chapter 1

INTRODUCTION

1.1 Origin of Experiment

This body of work was born out of a study of ion mixing in metallic bilayers [1]. We had found that the mixing efficiency under ion irradiation by heavy ions (i.e., Ar and Xe) scaled with the (negative) heat of mixing of the bilayer (ΔH_{mix}) [2]. That is, the more exothermic the reaction between the two layers, the larger the spreading of the interface for a given ion dose. Thus, a chemical driving force with an energy on the order of 1 eV/atom profoundly affects the mixing caused by ions with an incident energy of several hundred keV. This result ran counter to the prevailing theory that ion mixing was a purely ballistic process depending only upon the masses of the atoms in the bilayer [3]. However, the results were consistent with those expected for "thermal spike" mixing.

The "thermal spike" model describes the evolution of the collision cascade produced in a solid by heavy ion irradiation from a linear binary collision cascade at high energies (keV and above) to a "space filling" cascade involving a majority of atoms in a localized region at low energies ($\sim$10 eV) [4]. The energies of atoms within this region are assumed to reach a roughly Boltzmann distribution equivalent to a temperature on the order of 10^4 K for a duration of approximately 1 ps [5] (thus, the name "thermal spike"). During this time, atoms within the region undergo random walk diffusion. When the thermal spike coincides with the interface, the diffusion will be biased by the gradient in chemical potential due to the heat of mixing of the bilayer. From our experimental results [1,2,6,7], it appears that mixing within the thermal spike is the dominant mechanism of mixing for heavy ion irradiation in bilayers of average atomic number > 20.

The titanium/platinum system has one of the largest negative heats of mixing ($\Delta H_{mix} = -122$ kJ/gr·atom [8]) of the systems we have studied, and, as expected, it has one of the highest mixing efficiencies. However, we found that the heat of mixing of the system could be changed from highly negative to positive by adding hydrogen to the Ti layer. This change comes about because hydrogen is insoluble in Pt, and TiH_2 has a lower free energy than any TiPt compound [9]. Because of this drastic change in ΔH_{mix} and the fact that the addition of hydrogen would have very little effect on the "ballistic properties" of the bilayer under heavy ion irradiation (due to hydrogen's low mass), we felt that a comparison of the ion mixing of Ti/Pt and TiH_2/Pt bilayers would be quite enlightening.

At the time that we were conceiving this experiment, Fleischmann and Pons announced the discovery of "cold fusion" [10]. In the rush of experiments that followed, "cold fusion" was reported to be detected in palladium deuteride and titanium deuteride samples under various conditions, such as in electrolytic cells [11] and in heating and cooling between room temperature and liquid nitrogen temperature [12]. It was theorized that putting these materials in non-equilibrium states could possibly lead to a huge increase in the D–D fusion rate [13].

Realizing that the conditions existing in the thermal spike regime of a collision cascade were extremely far from equilibrium, we saw a chance to do two experiments in one by changing the TiH_2/Pt samples to TiD_2, and looking for fusion products during ion mixing. After further thought on the collision cascade process, we determined that head-on collisions between incident ions (with energies of several hundred keV) and deuterons could transfer enough energy to a deuteron to give it a significant chance of colliding with another deuteron and fusing. This type of fusion event could be explained by the "normal" D–D fusion cross section, and therefore, would not require the existence of "cold fusion." Thus, any fusion events occurring could be due to either high energy deuterium recoils in the early stages of the collision cascade, or "cold fusion" in the later, thermal spike region of the cascade. If fusion events from the high energy deuterium recoils dominated, the fusion products could be used as a probe (similar to nuclear reaction analysis) of either the deuterium content of the sample or the collision cascade process itself. If the "cold fusion" contribution dominated, we could learn more about the thermal spike process. Even if no fusion events were detected, we would still have the ion mixing results. Therefore, the experiment had great potential.

Having decided on the aims of the experiment, the next step was to fabricate the TiD_2/Pt samples. This turned out to be much more difficult than first anticipated. An existing hydrogen furnace was used to deuteride thin films of Ti. The titanium deuteride films produced invariably had a thick (~30 nm) surface layer of TiO_2. This was unacceptable for the experiment because the Pt layer had to be deposited after the deuteridation process to avoid interdiffusion between the layers during deuteridation. Therefore, the TiD_2/Pt interface would be contaminated by the thick oxide layer, which would severely affect the ion mixing. (It would essentially be a study of the ion mixing of TiO_2/Pt instead of TiD_2/Pt.) Many attempts were made to improve the furnace to reduce the oxygen contamination and to backsputter off the oxide layer from the sample, but all were unsuccessful. Therefore, the Pt layer was put aside, and the aim of the experiment was changed to include just the search for fusion events due to the ion irradiation of titanium deuteride.

Later, a whole new hydridation furnace was built (see Section 2.1) that could produce titanium deuteride samples suitable for the TiD_2/Pt experiment. By that time, financial support for the project had been discontinued and that experiment was dropped.

1.2 The Collision Cascade

The chain of events that occur as an energetic ion penetrates a solid are of great interest to those studying ion implantation, ion mixing, and ion analysis techniques [14,15]. Direct observation of the collision cascade within the solid is difficult due to the extremely short time scale ($\sim 10^{-11}$ sec) and small distances (< 1 μm) involved. Direct observations of the collision cascade have so far been limited to sputtered particles [16]. The majority of information about the collision cascade has come from indirect observations.

Experimental data giving indirect information about the collision cascade include ion range and range straggling, concentration of defects produced by ion irradiation, and the spreading of an interface between two different atomic species (ion mixing). Each of these quantities is measured after ion irradiation. Electronic processes, such as Auger electron emission and x-ray emission, caused by the collision cascade can also be analyzed to give information about the cascade itself. For example, Auger electron emission from sputtered atoms or atoms in the near surface region (the first 3 nm) can be used to analyze the near surface portion of the cascade [17,18]. X-ray production during ion irradiation of thick targets has been compared to calculated x-ray cross sections using a simple model of the collision cascade [19]. However, analyzing the cascade by use of signals of electronic nature has two drawbacks. The first is that the processes that create these particles are indirect in relation to the nuclear collisions involved in the cascade. The second (which is especially important for Auger processes) is that the detected particles (electrons and x-rays) undergo capture or attenuation over the course from the point where they are created to the surface, where they are detected. As the depths at which these particles are created is unknown, correction of the attenuation factor is not straightforward.

Another measurement that gives information about the collision cascade is nuclear reaction analysis. Normally, nuclear reaction analysis involves irradiating a target with a high energy ion that undergoes a nuclear reaction with an atom in the target, creating a different particle with an energy characteristic of the reaction. Thus detecting the reaction product gives information about nuclear collisions between the primary ion and the target atoms. In the present investigation, the incident ion does not undergo a nuclear reaction with an atom in the target, but transfers energy to an atom in the target (possibly through any number of intermediate collisions) which then undergoes a nuclear reaction with another target atom. In this case, information can be obtained about primary and higher generation recoil atoms in the collision cascade. The particles detected (3.02 MeV protons) are produced directly from the nuclear collisions of the cascade and have sufficient energy to reach the surface from the depth at which they were created and be detected.

Even with the lack of direct observation of the collision cascade within a solid, enough indirect information has been collected to adjust theoretical descriptions of the cascade processes to match closely most observable effects of ion irradiation of solids. The important parameters which must be specified to account for experimental observations include the energy loss of the ion and energetic recoils, the cross sections for ion–atom and atom–atom collisions, and the number and types of defects produced during the cascade. The production of defects is not important to this study, and will not be discussed further. Knowledge of the scattering cross sections is necessary to determine the energy distribution of primary and higher generation recoils in the cascade. Knowledge of the mechanisms of energy loss are necessary to determine the fraction of the ion energy going towards nuclear displacements. In metals and semiconductors, ion–electron collisions do not contribute to atomic displacements; therefore, in terms of the chain of nuclear displacements, the energy loss from ion-electron collisions simply acts to attenuate the incident ion energy between nuclear collisions.

To calculate the differential scattering cross section $d\sigma/dT$ for ion–atom and atom–atom collisions (where T is the energy transferred to the target atom), the appropriate interatomic potential for the atomic masses and range of interaction energies must be known. The method of calculating the differential scattering cross section for a given interatomic potential is explained in detail in [20]. For ion energies in the keV range and above, the appropriate potential lies between the hard sphere and coulomb potentials. For the hard sphere potential, $d\sigma/dT$ is a constant, i.e., all energy transfers are equally likely. For the coulomb potential, $d\sigma/dT$ varies as $1/T^2$, i.e., low energy transfers dominate. In the limit of high incident ion energy (MeV range), the coulomb potential best fits experimental results. However, as the interaction energy decreases, the effect of electron screening of the nuclear charges becomes significant, and a correction becomes necessary.

The general method of correcting for electron screening is to multiply the coulomb potential by a screening function $\phi(r/a)$

$$V(r) = \frac{Z_1 Z_2 e^2}{r} \phi\left(\frac{r}{a}\right) , \tag{1.1}$$

where Z_1 and Z_2 are the atomic numbers of the incident ion and target atom, respectively, e is the electronic charge (3.79 x 10^{-7} $(\mathrm{MeV\,cm})^{1/2}$), and a is called the screening length, a commonly used value of which is the Firsov screening length, which is given by

$$a = \frac{0.8853 a_0}{({Z_1}^{1/2} + {Z_2}^{1/2})^{2/3}} , \tag{1.2}$$

where a_0 is the first Bohr radius (0.52917 Å). The forms of the six screening functions considered in this work are listed in Table 1.1. It is not possible to calculate the differential cross section for these potentials in terms of analytical functions;

therefore, fits to the differential scattering cross section involving analytic functions and three adjustable parameters have been calculated [21]. Each of these screening functions has been adjusted to agree with experimental observations for varying ranges of incident ion energy and ion and target masses. The differential scattering cross sections for any of these six interatomic potentials should be expected to accurately describe the ion–atom and atom–atom collisions for the relatively high energies involved in this work.

Table 1.1 The electron screening functions for the six screened coulomb potentials considered in this work [21].

Potential	Form	Constants
Thomas-Fermi-Sommerfeld	$\phi(x) = (1 + (x^3/144)^{-1/\lambda})^{\lambda}$	$\lambda = 0.2678$
Bohr	$\phi(x) = e^{-\lambda x}$	$\lambda = 1$
Lenz-Jensen	$\phi(x) = q(\lambda, x)e^{-\lambda\sqrt{x}}$	$\lambda = (875/253)^{1/2}$
Lindhard [c^2=1.8]	$\phi(x) = 1 - x/\sqrt{x^2 + c^2}$	$c^2 = 1.8$
Lindhard [c^2=3.0]		$c^2 = 3.0$
Molière	$\phi(x) = 0.35e^{-\lambda x} + 0.55e^{-4\lambda x} + 0.1e^{-20\lambda x}$	$\lambda = 0.3$

The energy loss of the incident ion and energetic recoils is the sum of the nuclear and electronic energy losses. The nuclear energy loss is the result of the discrete collisions described above. The electronic energy loss is normally approximated as a continuous process, as opposed to a series of discrete ion-electron collisions. For relatively low energy ions (~10 keV/amu) in metals, the electronic energy loss is reasonably well approximated by the Lindhard–Scharff formula [22], in which the energy loss is proportional to the ion velocity v

$$\left(\frac{dE}{dx}\right)_{LS} = k\frac{v}{v_0}\ , \qquad k = {Z_1}^{1/6}\frac{8\pi e^2 N a_0 Z_1 Z_2}{({Z_1}^{2/3} + {Z_2}^{2/3})^{3/2}}\ , \tag{1.3}$$

where Z_1 and Z_2 are the atomic numbers of the incident ion and target atom, respectively, N is the atomic density of the target, and v_0 is the Bohr velocity $(Z_1 e^2/\hbar)$. At higher energies, the electronic energy loss increases less rapidly with energy, reaches a peak value, and then decreases with increasing energy. The peak in electronic energy loss occurs at ion velocities slightly higher than the "Thomas–Fermi" velocity ${Z_1}^{-1/3} v_0$, which correspond to an energy of approximately (25 keV/amu) ${Z_1}^{4/3} M_1$ (50 keV for D, 47 MeV for Ar). At velocities greater than the "Thomas–Fermi" velocity, the electronic energy loss is well described by the Bethe–Bloch formula [23]

$$\left(\frac{dE}{dx}\right)_{BB} = \frac{8\pi {Z_1}^2 e^4}{I} \frac{\ln(\varepsilon_B + 1 + 5/\varepsilon_B)}{\varepsilon_B} , \quad \varepsilon_B = \frac{4 m_e E}{M_1 Z_2 I} , \tag{1.4}$$

where m_e is the electron mass and the energy I is an average of the various excitations and ionizations of the electrons in a target atom and is of the order of approximately 10 eV. The transition in electronic energy loss between Lindhard-Scharff and Bethe-Bloch regimes is well described by the harmonic mean [23]:

$$\left(\frac{dE}{dx}\right)_e = \left(\frac{1}{\left(\frac{dE}{dx}\right)_{LS}} + \frac{1}{\left(\frac{dE}{dx}\right)_{BB}}\right)^{-1} . \tag{1.5}$$

In compound targets (i.e., targets containing more than one element), the energy loss is the sum of the losses in the constituent elements, weighted according to their atomic concentration in the compound. This is known as Bragg's rule.

The irradiating ions in this work are Ar and Xe with energies up to 600 keV. The maximum energy transferrable T_{max} to the target atoms (Ti and D) by an ion with energy E is given by

$$T_{max} = \frac{4 M_1 M_2}{(M_1 + M_2)^2} E \equiv \gamma_{1,2} E , \tag{1.6}$$

where M_1 and M_2 are the ion and target atomic masses, respectively. Thus, the maximum fraction of ion energy transferred directly from the ion to a deuteron is

18.3% for Ar and 5.95% for Xe. For ion–Ti energy transfers, the maximum fractions are 99.2% (Ar) and 78.3% (Xe). Therefore, the maximum possible deuteron energy is 110 keV (for 600 keV Ar irradiation). This energy is high enough to require use of the Bethe-Bloch formula for determination of the electronic energy loss for the highest energy deuterons. The electronic energy loss of all other particles is adequately described by the Lindhard–Scharff formula.

The information above on differential scattering cross sections, electronic energy loss, and maximum energy transfer is sufficient to accurately describe the collision cascade caused by Ar and Xe irradiation of titanium deuteride. This information will be used in Chapter 4 to calculate the theoretically expected fusion yields for ion irradiation of titanium deuteride.

1.3 The D–D Fusion Reaction

Following the treatment of Clayton [24], a nuclear reaction occurs when a particle a strikes a nucleus X producing a nucleus Y and a new particle b is symbolized by

$$a + X \rightarrow Y + b, \quad \text{or} \quad X(a,b)Y.$$

In the course of this reaction, the total energy (kinetic energy plus rest-mass energy), momentum, and angular momentum are conserved. The conservation of mass and energy requires that for the reaction X(a,b)Y

$$E_{aX} + (M_a + M_X)c^2 = E_{bY} + (M_b + M_Y)c^2 \ , \tag{1.7}$$

where E_{aX} is the sum of the kinetic energies of a and X in the center-of-mass frame, E_{bY} is a similarly quantity for b and Y, M_a is the rest mass of a, etc. The energy liberated by a reaction in which the mass of the products is less than that of the reactants will be shared by the reaction products such that the total momentum in the center-of-mass frame remains zero:

$$E_Y = \frac{M_b E_{bY}}{M_b + M_Y} , \qquad E_b = \frac{M_Y E_{bY}}{M_b + M_Y} . \tag{1.8}$$

The D–D nuclear reactions of interest in this work are D(d,p)T and D(d,n)^{3}He. The atomic numbers (Z), numbers of nucleons (A), and atomic masses of the relevant particles are listed in Table 1.2. The energy liberated in the D(d,p)T reaction is 4.03 MeV, and that liberated in the D(d,n)^{3}He is 3.27 MeV. These energies are divided among the reaction products such that in the center-of-mass frame

$$\mathrm{D} + \mathrm{D} \rightarrow \mathrm{T}\,(1.01\ MeV) \ + \ \mathrm{p}\,(3.02\ \mathrm{MeV})$$

$$\mathrm{D} + \mathrm{D} \rightarrow {}^3\mathrm{He}\,(0.82\ MeV) \ + \ \mathrm{n}\,(2.45\ \mathrm{MeV}).$$

A third reaction,

$$\mathrm{D} + \mathrm{D} \rightarrow {}^4\mathrm{He} \ + \ \gamma\,(23.85\ \mathrm{MeV}),$$

is also possible, but has a cross section which is seven orders of magnitude smaller than the two reactions above and will not be mentioned further.

Table 1.2 Atomic masses and energy equivalents of reactants and products of D–D nuclear reactions (Information taken from Ref 24).

Element	Z	A	Mass (amu)	Energy Equivalent (MeV)
n	0	1	1.00867	939.549
H	1	1	1.00783	938.767
D	1	2	2.01410	1876.092
T	1	3	3.01605	2809.384
^{3}He	2	3	3.01603	2809.365
^{4}He	2	4	4.00260	3728.337

In order for two particles to undergo a nuclear reaction, the two nuclei must be brought close enough together to be within the range of the strong nuclear force, i.e., the center-to-center separation must be less than the range of the nuclear force ($\sim 10^{-15}$ m) plus the sum of the nuclear radii. This distance, known as the interaction radius R, is generally given as [24]

$$R = 1.4(A_1^{1/3} + A_2^{1/3}) \text{ fm} \ , \quad 1 \text{ fm} = 10^{-15} \text{ m} \ , \tag{1.9}$$

where A_1 and A_2 are the number of nucleons of the interacting particles. For D–D reactions, the interaction radius is approximately 3.5 fm. To achieve such a small separation, the particles must penetrate the coulomb barrier and (for non-zero quantized angular momentum) the centrifugal barrier.

The probability of finding the particles with a separation less than R, can be found by solving the radial component of the time-independent Schrödinger equation

$$-\frac{\hbar^2}{2\mu}\frac{d^2\chi(r)}{dr^2} + [V(r) - E]\,\chi(r) = 0 \ , \tag{1.10}$$

where $\chi(r)=r\psi(r)$, μ is the reduced mass of the interacting particles, and V(r) is defined by:

$$V(r) = \begin{cases} \frac{Z_1 Z_2 e^2}{r} + \frac{l(l+1)\hbar^2}{2\mu r^2} & r > R \ , \\ V_{nuc} & r < R \end{cases}$$

where the first term is the coulomb potential, the second is the centrifugal potential, V_{nuc} is the (attractive) nuclear potential. Z_1 and Z_2 are the atomic numbers of the interacting particles, and l is the orbital angular momentum quantum number. The form of this potential is shown in figure 1.1. The potential barrier reaches its maximum height at $r=R$. For the D–D reaction, the peak coulomb barrier is approximately 0.4 MeV and the peak centrifugal barrier is approximately 0, 3.4 MeV, and 10.0 MeV for the states l=0,1,2, respectively, at r=3.5 fm. It can be seen that for the case of D–D reactions, the effects of the centrifugal barrier are comparable

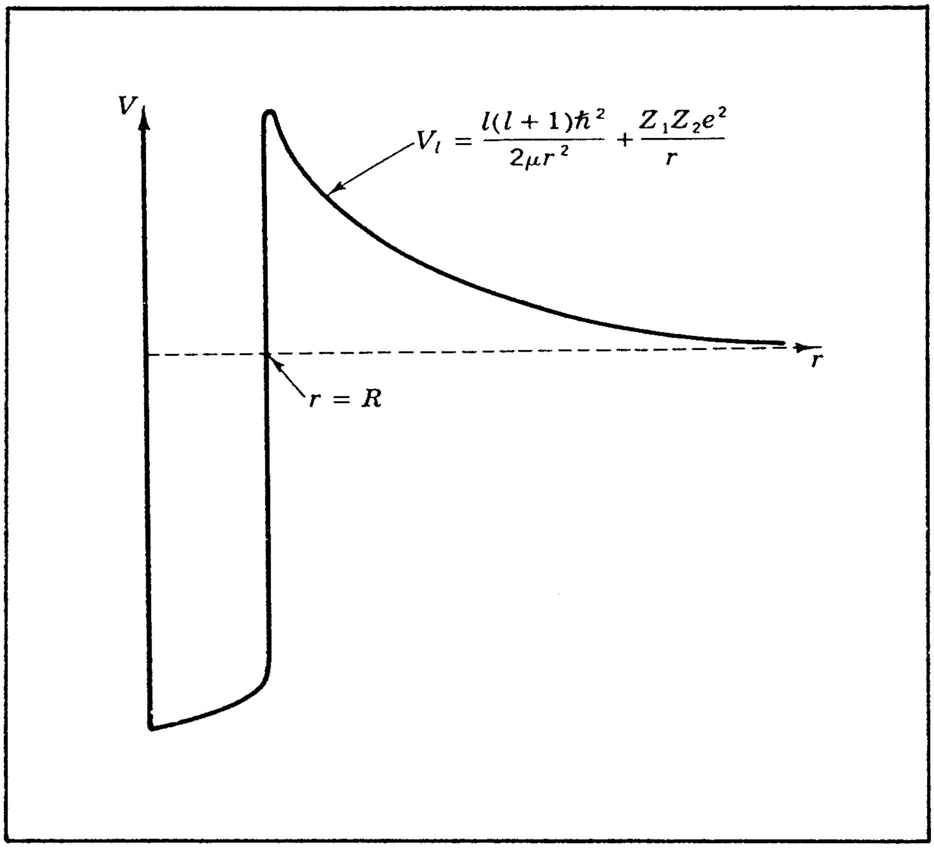

Figure 1.1 The interatomic potential for D–D interaction. For $r < R$ the deep negative potential is due to the strong nuclear force. For $r > R$ the coulomb and centrifugal potentials present a barrier which must be penetrated for a reaction to occur (taken from [24]).

to those of the coulomb barrier. The centrifugal barrier will inhibit increasingly higher orbital angular momentum states from participating in the reaction for low energy deuterons, resulting in nearly isotropic angular distributions of the reaction products at low energies.

In the present work, the energy E of the deuterons is significantly less than that of the coulomb barrier. Therefore, for fusion to occur, the deuterons must tunnel through the potential barrier. The reaction cross section for this case is of the form

$$\sigma(E) = \frac{S(E)}{E} \exp\left(-\frac{2\pi Z_1 Z_2 e^2}{\hbar v}\right) = \frac{S(E)}{E} \exp\left(-\frac{b}{E^{1/2}}\right) , \qquad (1.11)$$

where E is the energy of the interacting particles in the center-of-mass frame, v is the relative velocity of the particles, $S(E)$ is the astrophysical S factor, and b=31.29 $Z_1 Z_2 \mu^{1/2}$ keV$^{1/2}$, where μ is the reduced mass in units of amu. The S factor is normally a slowly varying function of energy away from the vicinity of resonances. The exact forms of the nuclear wave functions and the interaction potential are not known well enough to determine $S(E)$, and thus $\sigma(E)$, from theoretical calculations. Therefore, experimentally normalized cross sections are relied upon in the present work.

The D(d,p)T and D(d,n)^{3}He reactions were investigated for center-of-mass energies of 2.98 to 162.5 keV by irradiating a deuteron gas target with energetic deuterons [25] and have been studied at energies above 10 keV by many authors. Absolute cross sections and angular distributions have been reported for both reactions. The values of $S(E)$ calculated from the measured cross sections [25] are shown in figure 1.2. These values are from angle integrated data. The angular distributions of the reaction products are shown in figure 1.3. As expected, because of the relatively large centrifugal barrier, the angular distribution is nearly isotropic for energies less than approximately 30 keV.

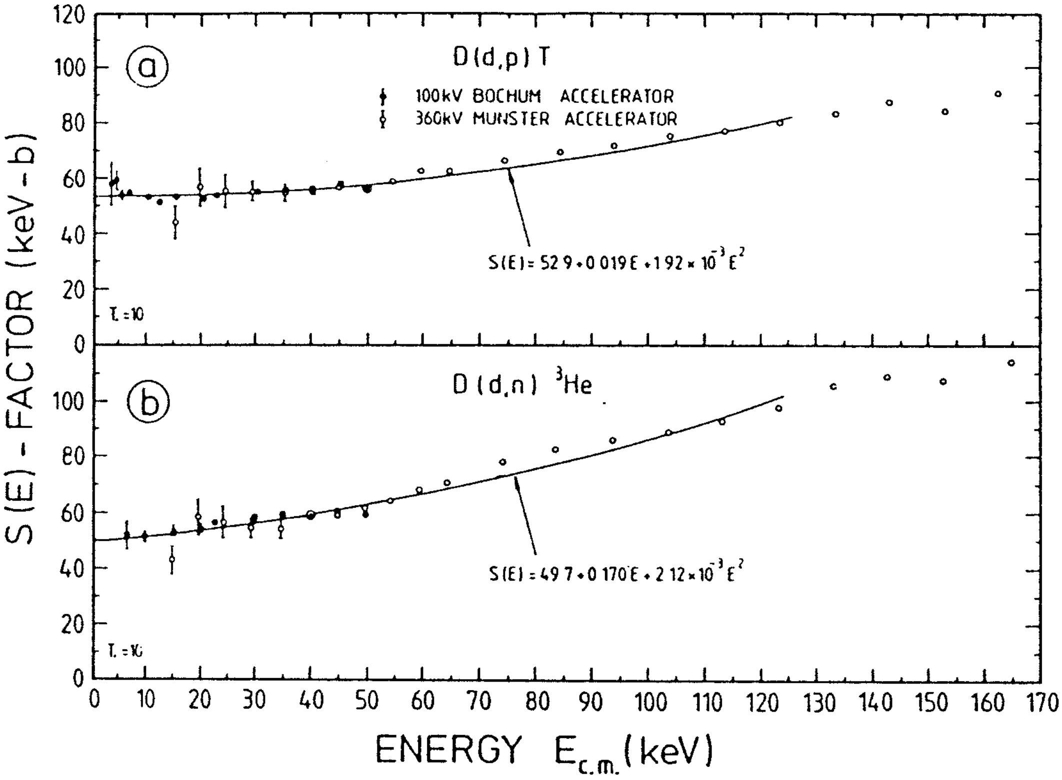

Figure 1.2 Experimental $S(E)$-factor data for the reactions (a) D(d,p)T and (b) D(d,n)^{3}He. The solid curves are the results of polynomial fits to the data for $E_{CM} \leq 120$ keV (taken from [25]).

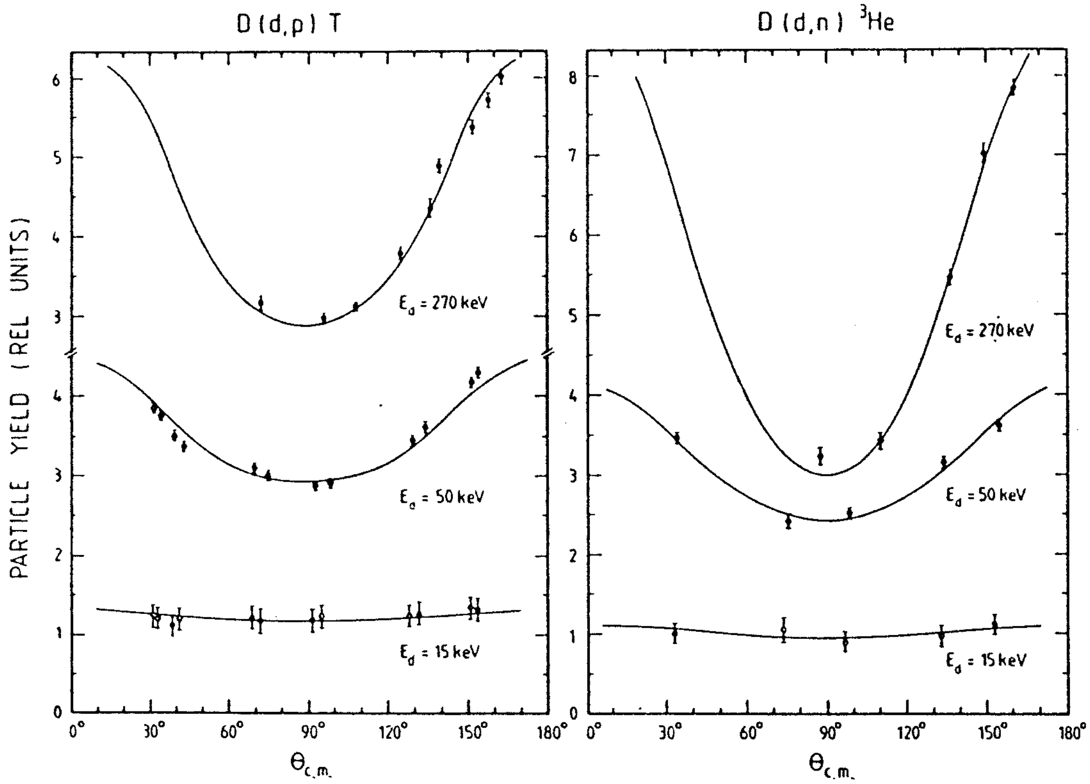

Figure 1.3 Angular distributions at representative energies for D(d,p)T and D(d,n)^{3}He reactions. The solid curves through the data points are the results of χ^2 analysis using even Legendre polynomials (taken from [25]).

Another study measured fusion cross sections for center-of-mass energies of 1.5 to 3 keV by irradiating thin foils of TiD_2 with energetic deuterons [26]. The cross sections obtained are in good agreement with those calculated using $S(E)$ determined from the experiment above. Thus, fusion cross sections for deuterium in gaseous form and in solids (where it is possible that electron shielding could affect the cross section) are roughly equivalent.

In this thesis, D–D fusion within titanium deuteride was studied. The mean center-of-mass energy at which fusion occurred was estimated to be less than 25 keV for all irradiations. Therefore, the assumption of an isotropic distribution of fusion products is a relatively good one. In addition, the angle at which fusion products were detected (130° in the lab frame) was near the angle of average fusion yield ($\approx$125° in the center-of-mass frame), resulting in a deviation of less than 4% from the angle integrated cross section for the highest energy deuterons produced in this experiment.

References

[1] T. W. Workman, Y. T. Cheng, W. L. Johnson, and M-A. Nicolet, Appl. Phys. Lett. **50**, 1485 (1987).

[2] Y. T. Cheng, M. Van Rossum, M-A. Nicolet, and W. L. Johnson, Appl. Phys. Lett. **45**, 185 (1984).

[3] P. Sigmund and A. Gras-Marti, Nucl. Instrum. Methods **182/183**, 25 (1981).

[4] Y. T. Cheng, M-A. Nicolet, and W. L. Johnson, Phys. Rev. Lett. **58**, 2083 (1987).

[5] T. Diaz de la Rubia, R. S. Averback, R. Benedek, and H. Hsieh, J. Mater. Res. **4**, 579 (1989).

[6] M. Van Rossum, Y. T. Cheng, M-A. Nicolet, and W. L. Johnson, Appl. Phys. Lett. **46**, 610 (1985).

[7] E. Ma, T. W. Workman, W. L. Johnson, and M-A. Nicolet, Appl. Phys. Lett. **54**, 413 (1989).

[8] A. R. Miedema, Philips Tech. Rev. **36**, No. 8, 217 (1976).

[9] J. J. Reilly, Z. Phys. Chem. NF **117**, 155 (1979).

[10] M. Fleischmann and S. Pons, J. Electroanal. Chem. **261**, 301 (1989).

[11] S. E. Jones, E. P. Palmer, J. B. Czirr, D. L. Decker, G. L. Jensen, J. M. Thorn, S. F. Taylor, and J. Rafelski, Nature **338**, 737 (1989).

[12] A. De Ninno, A. Frattolillo, G. Lollobattista, L. Martinis, M. Martone, L. Mori, S. Podda, and F. Scaramuzzi, Europhys. Lett. **9**, 221 (1989).

[13] S. E. Koonin,"Enhancement of cold fusion rates by fluctuations," April 17, 1989 (unpublished report).

[14] P. D. Townsend, J. C. Kelly, and N. E. W. Hartley, *Ion Implantation, Sputtering and their Applications* (Academic, London, 1976).

[15] R. S. Averback, Nucl. Instrum. Methods **B 15**, 675 (1986).

[16] R. Behrisch (ed.), *Sputtering by Particle Bombardment I*, Topics Appl. Phys. **47** (Springer-Verlag, Berlin, 1981).

[17] T. D. Andreadis and J. Fine, Nucl. Instrum. Meth. **209**, 495 (1983).

[18] O. Grizzi and R. A. Baragiola, Phys. Rev. **A 35** 135 (1987).

[19] K. Taulbjerg and P. Sigmund, Phys. Rev. **A 5**, 1285 (1972).

[20] S. Geltman, *Topics in Atomic Collision Theory* (Academic, New York, 1969).

[21] K. B. Winterbon, Rad. Effects **13**, 215 (1972).

[22] J. Lindhard and M. Scharff, Phys. Rev. **124**, 128 (1961).

[23] J. P. Biersack, E. Ernst, A. Monge, and S. Roth, *Tables of Electronic and Nuclear Stopping Powers and Energy Straggling for Low Energy Ions* (Hahn-Meitner-Institut, Berlin, 1975) pp. 3–5.

[24] D. D. Clayton, *Principles of Stellar Evolution and Nucleosynthesis* (McGraw-Hill, New York, 1968), Ch. 4.

[25] A. Krauss, H. W. Becker, H. P. Trautvetter, and C. Rolfs, Nucl. Phys. **A 465**, 150 (1987).

[26] J. Roth, R. Behrisch, W. Möller, and W. Ottenberger, Nucl. Fusion **30**, 441 (1990).

Chapter 2

SAMPLE PREPARATION AND CHARACTERIZATION

2.1 Fabrication of Titanium Deuteride (TiD) Thin Films

The desired sample composition and configuration was determined by the requirements of the experiment. Since the fusion yield from ion irradiation was expected to be quite small, possibly at the limit of detectability, the samples needed to be designed to maximize the number of fusion events produced. In terms of composition, this meant maximizing the deuterium concentration. (A collision between two deuterons is necessary to create a fusion event; therefore, the fusion yield varies quadratically with deuterium concentration.) In terms of sample configuration, the TiD layer had to be thick enough so that the entire collision cascade caused by the ion with the largest projected range would remain entirely within the TiD layer. This was planned to be 300 keV Ar^+, with a projected range of 200 nm and a range straggling of 80 nm; therefore, the minimum TiD thickness would be about 300 nm. Finally, the area of the sample had to be large enough so that the maximum ion beam current could be applied to it, yet still be able to fit in the hydrogen furnace. The beam in our ion implanter cannot be focussed to a size smaller than approximately 1 cm square, while the furnace cannot accommodate samples wider than 1.2 cm. Therefore, a sample size of 1.2 cm x 1.2 cm was chosen.

Thin films of Ti were prepared by electron-beam evaporation in an oil-free vacuum system pumped with an ion pump. The base pressure of the system was 3×10^{-8} Torr, and the pressure remained below 2×10^{-7} Torr during evaporation at a rate of 2 - 2.5 nm/s. The substrate used was a 2 inch $\langle 111 \rangle$ Si wafer with a 500 nm thermally-grown SiO_2 surface layer. After the Ti evaporation, the wafer was cut into 1.2 cm squares for the deuteridation process. Backscattering analysis showed the thickness of the Ti layer to be 325 nm, with a variation of less than 5% over the entire wafer, Also revealed was a ~1.4 at% oxygen contamination in the bulk and a surface layer of TiO_2 approximately 3 nm thick.

To produce titanium deuteride, titanium was heated in a deuterium ambient at a temperature high enough to allow deuterium to penetrate the surface oxide layer and for a time long enough for a homogeneous TiD layer to form. The optimum temperature and deuterium pressure for creating TiD with the highest deuterium concentration were found by consulting the pressure-composition isotherms for the Ti-H system (Fig. 2.1) [1]. From the figure, it is clear that, for a given hydrogen pressure, the hydrogen concentration increases with decreasing temperature. For a given temperature, the hydrogen concentration increases with increasing pressure. Therefore, to maximize the hydrogen (or deuterium) concentration, a combination of low temperature and high pressure must be used. For a composition of TiD_2, a pressure of ~20 ATM is necessary at 500°C, ~2 ATM at 400°C, or ~0.1 ATM at 300°C.

Considering the need for a pressure of a few atmospheres, the relatively high cost of deuterium (~$2 per liter), and safety, a furnace with a static D ambient (as opposed to one with flowing D) was used for deuteriding of the Ti films. Also, because of the cost of deuterium, hydrogen (^1H) was used initially, until good quality TiH films were produced, only then was the system switched to deuterium.

The system used for deuteriding the samples is composed of a quartz tube (part of which is enclosed in a furnace) connected to a metal tube with connections for introducing hydrogen or deuterium, loading the samples, rough pumping, and measuring the pressure (Fig. 2.2). The quartz tube is roughly 1 inch in diameter, 28 inches long, and is sealed to a 2.75 inch Conflat-type flange. This is connected

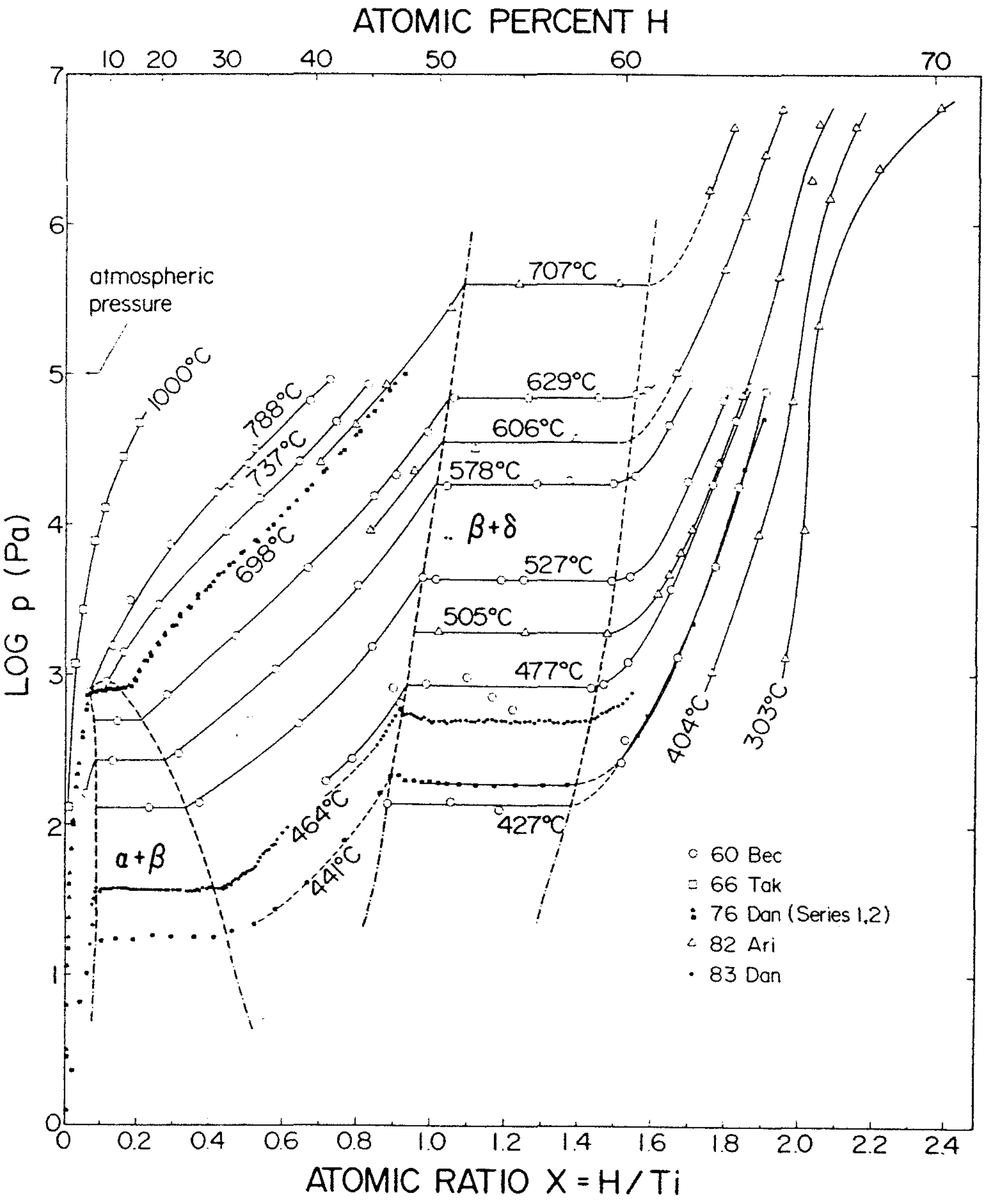

Figure 2.1 Pressure-composition isotherms for the Ti–H system.

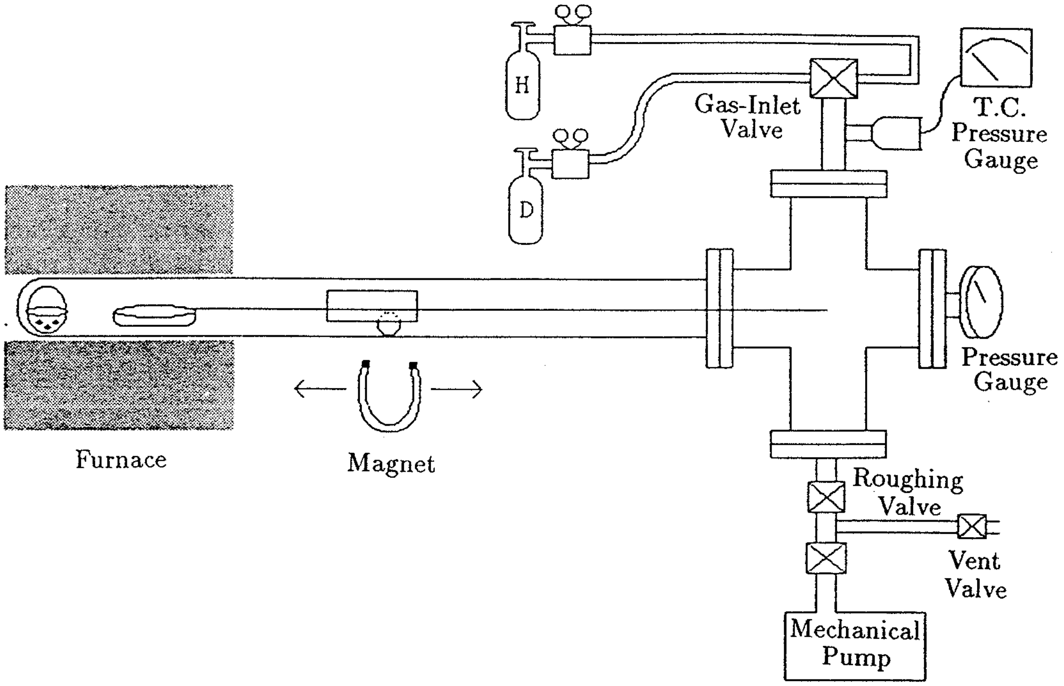

Figure 2.2 Schematic of furnace system used for hydiding and deuteriding Ti samples.

to a 4-way cross. Samples are loaded from the opposite side of the cross, which is sealed with a blank flange using a viton O-ring. Copper gaskets were used for the other three arms of the cross. The lower arm of the cross is used for rough pumping and venting. The roughing pump used is a rotary-vane mechanical pump with a pumping speed of 20 ℓ/s and ultimate vacuum of 5 mTorr. The upper arm is used for introducing hydrogen or deuterium. A three-position gas-inlet valve selects between hydrogen, deuterium, or closed. This arm also contains a thermocouple pressure gauge for measuring vacuum during roughing. A second gauge, attached to the sample loading flange, is used for measuring pressures of -30 inches of Hg to +60 psig during deuteridation. Stainless steel tubing is used between the regulators on the gas bottles and the gas-inlet valve. The total volume of the system (between the roughing valve and the gas inlet valve) is approximately 550 ml. The base pressure of the system is 40 mTorr, and the system is able to maintain a pressure of under 200 mTorr for 24 hours without being pumped. It will hold a positive pressure indefinitely without a noticeable loss of pressure.

A quartz boat (with a capacity of four 1.2 cm square samples) is used to hold the Ti samples. The boat is attached to a quartz rod, which in turn is attached to an aluminum housing. The aluminum housing contains an iron roller which can be manipulated with a magnet from the outside of the system in order to move the boat in and out of the furnace. A small quartz basket containing 99.8% pure Ti sponge is placed at the end of the quartz tube. The sponge is used to getter any oxygen before the samples are moved into the furnace. The purity of the hydrogen and deuterium gases used was 99.95%.

The procedure for hydriding the samples was as follows: A quartz basket containing Ti sponge was placed at the far end of the quartz tube. Ti samples were loaded into the quartz boat, and the boat assembly was loaded into the system and positioned so that the samples remained outside of the furnace. The system was sealed and roughed down to the base pressure. The system was then filled with hydrogen (or deuterium) to a pressure of 10 psi above atmospheric pressure (10 psig) and then roughed to the base pressure again. This purge cycle was repeated 3 times to minimize the residual air content in the system. After the purge cycles, the system was filled to the desired pressure and the gas inlet valve was closed. At this point, all valves were closed, and the amount of hydrogen in the system was fixed at this level.

The furnace was turned on and set at 700°C. A temperature of 700°C was maintained for approximately 2 hours in order for the Ti-sponge to getter any residual oxygen. Next, the temperature was lowered to that desired for the deuteridation process and the Ti samples were moved into the furnace and annealed for the desired time. Finally, the temperature was lowered to 250°C and the samples were annealed for about 16 hours to form a homogeneous layer. The samples were removed only after the furnace had reached room temperature so that oxygen contamination was minimized.

The parameters modified between different runs were hydriding pressure, temperature, and time. A log of temperature and pressure versus time was kept for each run. Temperatures of 250, 300, 350, 400, 425, 450, and 500°C were used; however, only those above 400°C produced a measurable amount of hydridation. Hydridation times were varied from 30 minutes to 20 hours. The pressure was set from 20 - 30 psig at room temperature, producing pressures of 15 - 35 psig during hydridation. As the furnace temperature was raised and lowered, the pressure varied (since it was a closed system). However, only a fraction of the tube volume was heated, making it difficult to anticipate the pressure for a given furnace temperature. Also, the Ti getter absorbed hydrogen as well as oxygen, with the amount of hydrogen absorbed dependent on the amount of getter used. Therefore, no effort was made to predict the hydriding pressure from the pressure set at the beginning of the experiment, rather, the pressure was measured during the experiment. It was found that the above variation in hydriding pressure did not significantly affect the hydrogen content of the titanium hydride films produced.

Hydrides could not be produced at temperatures below 400°C due to the presence of a native oxide on the Ti films. The same behavior was exhibited by the Ti getter. A steady increase in pressure occurred as the furnace was initially heated up. However, a sharp drop in pressure (~4 psi) occurred as the furnace temperature rose above ~400°C indicating the absorption of hydrogen by the Ti getter. While increasing the temperature at ~1°C/min, this sudden drop occurred at 401±2°C. Reference 2 indicates that at approximately 400°C TiO_2 dissolves into the bulk, removing the barrier to the absorption of hydrogen.

Titanium samples annealed at 350°C for 20 hours at a hydrogen pressure of 35 psig showed no measurable intake of hydrogen. Also, samples annealed at 425°C for 30 minutes and then at 250°C for 16 hours contained roughly the same amount of hydrogen as those annealed only at 425°C for 30 minutes. The only effect of the 250°C anneal was to uniformly distribute the hydrogen throughout the Ti layer. Therefore, it appears that heat treatment above 400°C does not permanently remove the barrier to hydrogen absorption, but only removes it during the time the film temperature exceeds 400°C. This interpretation is consistent with a surface oxide layer which acts as a barrier to hydrogen absorption below 400°C but is dissolved into the bulk at higher temperatures.

Experiments at temperatures above 400°C (i.e., 425, 450, and 500°C) with fixed H pressure and anneal duration produced TiH films that had decreasing H concentrations with increasing temperature, just as predicted by the pressure-composition isotherms. Also, it was found that increased annealing temperature lead to thicker surface oxide layers and higher oxygen concentrations in the TiH films. The source of the oxygen is unclear, but since a getter was used, it may be posited that oxygen or water vapor are outgassing from the quartz boat and push rod when they and the samples are first placed into and heated by the furnace. From these results, the optimum temperature that maximizes the hydrogen concentration and minimizes the oxygen contamination is located just above the point at which the surface oxide layer dissolves. For the experiment, a temperature of 425°C was chosen.

Titanium hydride samples were produced at a hydridation temperature of 425°C and a pressure of 35 psig for times of 30, 90, and 180 minutes. Resulting hydrogen concentrations increased from $TiH_{1.65}$ to $TiH_{1.85}$ with increasing annealing duration. However, increasing anneal duration also increased surface oxide thickness and oxygen concentration in the bulk of the film. For example, the surface TiO_2 layer thickness was 6 nm after 30 minutes and 15 nm after 180 minutes. Changes in the 250°C annealing duration after the higher temperature hydridation anneal did not appear to affect the oxygen contamination. From these results, it appears that oxygen enters the sample only in combination with hydrogen. Therefore, in order to minimize the oxygen contamination, the hydridation time must be decreased, which also has the effect of decreasing the hydrogen content of the TiH films. The best compromise was deemed to be a 30 minute hydridation time.

The optimum hydridation process was found to be a 30 minute anneal at 425°C and 15 - 35 psig followed by a 16 hour anneal at 250°C. This process was repeated using deuterium (instead of hydrogen) at a pressure of 16 psig. Eight titanium deuteride samples were produced in two runs. The samples had a composition of approximately $TiD_{1.7}$ and a surface TiO_2 layer 6 nm thick.

2.2 Backscattering Analysis of TiD Thin Films

Backscattering spectrometry (RBS) was performed on the titanium deuteride films in order to determine the precise sample composition. A tandem-mode NEC 3SDH (1 MV) Pelletron accelerator was used to produce beams of 2.0 - 3.10 MeV He^{++} ions. The scattering geometry was such that the single axis of rotation of the sample was coplanar with the incident and scattered beam directions and perpendicular to the incident beam direction. A scattering angle of 170° was used. The backscattered particles were detected using a Si surface barrier detector, which subtended a solid angle of approximately 8 mSr. Signal processing was accomplished using an Ortec 142 Charge-sensitive preamplifier, an Ortec 572 spectroscopy amplifier (using a 1 μs shaping time), a Canberra 8075 100 MHz ADC, and a Canberra S100 multichannel analyzer (MCA). A detector bias of 50 V was provided through the preamplifier by an Ortec 428 detector bias supply. The energy resolution of the detection system was typically 18 keV (FWHM).

2.2.1 Oxygen Resonance for Determination of Oxygen Concentration

Without the use of 3.05 MeV $^{16}O(\alpha,\alpha)^{16}O$ resonance, it is difficult to determine by backscattering analysis the oxygen concentration in bulk of the titanium deuteride layer. This is due to the fact that the small oxygen signal is superimposed over the much larger Si signal of the Si substrate and is lost in the statistical fluctuations. The height of the oxygen signal can be increased by as much as a factor of 25 over its Rutherford value [3,4] by use of the resonance energy, allowing the detection of as little as 0.2 at% oxygen in Ti (for the given sample configuration). Below is a brief explanation of how the oxygen concentration of the sample is determined by the height of the oxygen signal. The analysis is valid for backscattering with or without the resonant condition.

Assuming a composition of $\mathrm{Ti}_{1-x-y}\mathrm{D}_x\mathrm{O}_y$ (where $0 \leq x, y, < 1$), the height of the oxygen signal is [5]:

$$H_O^{TiDO} = y\sigma_O(E)\Omega Q \frac{\mathcal{E}}{[\varepsilon(E)]_O^{TiDO} \cos\theta_T}, \tag{2.1}$$

where Ω is the detector solid angle, Q is the integrated charge, $\sigma_O(E)$ is the differential scattering cross section for oxygen scattering a He^{++} ion of energy E through an angle of 170°, $\mathcal{E}$ is the energy per channel of the MCA, $[\varepsilon(E)]_O^{TiDO}$ is the stopping cross section factor for He^{++} of energy E in $\mathrm{Ti}_{1-x-y}\mathrm{D}_x\mathrm{O}_y$ assuming it is backscattered by an oxygen atom, and θ_T is the tilt angle of the sample normal in relation to the incident beam direction.

The integrated charge, Q, is obtained by integrating the ion beam current (using a BIC 1000 Current Integrator); however, there is an uncertainty of about 10% due to secondary electrons and neutral beam effects. The detector solid angle, Ω, also has a significant uncertainty due to the difficulty in measuring it precisely. Therefore, the quantity ΩQ was obtained using the height ($H_{Si}^{SiO_2}$) of the Si signal from the $\mathrm{SiO_2}$ layer as a reference. This method is quite reliable, since there is no channelling in the amorphous $\mathrm{SiO_2}$ layer, and its composition and stopping power are well known. Using the Si in $\mathrm{SiO_2}$ height as a reference, the formula for the height of the oxygen signal becomes:

$$H_O^{TiDO} = y\left(3H_{Si}^{SiO_2}\right)\frac{\sigma_O(E)}{\sigma_{Si}(E)}\frac{[\varepsilon(E)]_{Si}^{SiO_2}}{[\varepsilon(E)]_O^{TiDO}}, \tag{2.2}$$

where the factor of 3 comes from the fact that Si atoms make up only one third of the atoms in $\mathrm{SiO_2}$.

The stopping cross section factor, $[\varepsilon(E)]$, is a description of the energy loss of the He ion along both its inward and outward paths in the material. For the general compound A_mB_n, the stopping cross section factor is (assuming our scattering geometry):

$$[\varepsilon(E)]_X^{AB} = \sec\theta_T\Big(K_X\varepsilon^{A_nB_m}(E) + \sec\theta_D\varepsilon^{A_nB_m}(K_XE)\Big), \tag{2.3}$$

where θ_T is the sample tilt angle, θ_D is the scattering (or detector) angle, $\varepsilon^{A_nB_m}(E)$ is the stopping cross section (in units of eV cm^2 per atom) of a He ion of energy E in the material A_nB_m, and K_X is the kinematic factor for He scattering at an angle of 170° from atom X (i.e., a He ion with energy E immediately before striking atom X will have energy K_XE immediately after striking atom X). X may be either A, B, or any impurity atom that happens to be in the compound. Using Bragg's rule, the stopping cross section $\varepsilon^{A_nB_m}$ can be expressed as

$$\varepsilon^{A_nB_m} = \left(\frac{n}{n+m}\right)\varepsilon^A + \left(\frac{m}{n+m}\right)\varepsilon^B, \tag{2.4}$$

where ε^A and ε^B are the stopping cross sections for atoms A and B, respectively. These values can be found in tables such as Table VI and Table VII of Ref. 5.

The above analysis can be performed on the stopping cross section factor for the TiDO layer to explicitly show its dependence on the oxygen concentration, y. For simplicity, but without losing generality, assume $\theta_T = 0$; therefore,

$$\begin{aligned}
[\varepsilon(E)]_O^{TiDO} &= K_O\varepsilon^{TiDO} + \sec\theta_D\varepsilon^{TiDO}(K_OE) \\
&= K_O\Big((1-x-y)\varepsilon^{Ti}(E) + x\varepsilon^D(E) + y\varepsilon^O(E)\Big) \\
&\qquad + \sec\theta_D\Big((1-x-y)\varepsilon^{Ti}(K_OE) + x\varepsilon^D(K_OE) + y\varepsilon^O(K_OE)\Big) \\
&= (1-x-y)[\varepsilon(E)]_O^{Ti} + x[\varepsilon(E)]_O^D + y[\varepsilon(E)]_O^O,
\end{aligned} \tag{2.5}$$

where $[\varepsilon]_O^{Ti}$ can be thought of as the stopping cross section factor for an ion scattering off a solitary oxygen atom in a pure Ti matrix. Substituting this result into equation (2.2), we can now solve for y explicitly as a function of deuterium concentration x:

$$y = \frac{\eta\Big\{(1-x)[\varepsilon(E)]_O^{Ti} + x[\varepsilon(E)]_O^D\Big\}}{1+\eta\Big\{[\varepsilon(E)]_O^{Ti} - [\varepsilon(E)]_O^O\Big\}}, \qquad \eta = \frac{1}{3}\frac{H_O^{TiDO}}{H_{Si}^{SiO_2}}\frac{\sigma_{Si}(E)}{\sigma_O(E)}\frac{1}{[\varepsilon(E)]_{Si}^{SiO_2}}. \tag{2.6}$$

The heights are determined experimentally and the stopping cross section factors are easily calculated. For Rutherford scattering, the ratio $\sigma_{Si}(E)/\sigma_O(E)$ can be approximated as Z_{Si}^2/Z_O^2 (where Z is the atomic number), or the individual scattering cross section values can be found in tables (such as Table X. of Ref. 5). However, when the oxygen signal is due to 3.05 MeV resonant scattering, $\sigma_O(E)$ becomes system dependent and is more difficult to calculate.

The 3.05 MeV oxygen resonance has a HWHM of ~10 keV [4,6]. However, energy straggling along the incoming and outgoing paths and the detector resolution can significantly broaden the resonance peak, with the additional effect of reducing the peak yield value. (The total resonance peak area is conserved for a homogeneous material.) By using a standard, such as SiO_2 the effective HWHM and peak $\sigma_O(E)$ value for a given incident beam energy can be determined for the system. SiO_2 on Si is an excellent standard because it has a well defined oxygen concentration and the Si signal is relatively flat in the region of the oxygen signal, making Si background subtraction easy. The peak oxygen signal height can be compared to the height of the Si signal in the SiO_2 layer on the same spectrum to determine the effective peak scattering cross section:

$$\frac{\{\sigma_O(E_R)\}_{eff}}{\sigma_{Si}(E_R)} = \frac{H_O^{SiO_2}}{2H_{Si}^{SiO_2}} \frac{[\varepsilon(E_R)]_O^{SiO_2}}{[\varepsilon(E_R)]_{Si}^{SiO_2}}, \tag{2.7}$$

where E_R =3.05 MeV, $H_O^{SiO_2}$ is the peak height of the oxygen signal after subtraction of the Si background, $H_{Si}^{SiO_2}$ is the Si height corresponding to He ions with 3.05 MeV immediately before scattering, and the factor of 2 is due to the fact that there are twice as many oxygen atoms as Si atoms in SiO_2. The value of $\sigma_O(E_R)_{eff}/\sigma_{Si}(E_R)$ determined by the SiO_2 standard can then be substituted into Eq. 2.6 for spectra taken under the same conditions (i.e., same incident beam energy and detector resolution).

To determine the bulk oxygen concentration in the titanium film, an incident beam energy of 3.077 MeV was used, corresponding to an oxygen resonance at a depth of 80 nm in pure Ti. To determine the bulk oxygen concentration in the film after deuteridation, a beam energy of 3.084 MeV was used, corresponding to a depth of 80 nm in $TiD_{1.7}$ (my best guess of the composition, based on the results from the titanium hydride samples). Spectra of two of the samples (one from each deuteridation run) and the $\langle Si\rangle/SiO_2$ standard were taken before and after the deuteridation process. Comparing the signal heights from the standard, it was determined that $\sigma_O(E_R)_{eff}/\sigma_{Si}(E_R)$=4.38±0.05, which is 14.6 times the value for pure Rutherford scattering. Figure 2.3a shows the spectra for sample Ti10 before and after deuteridation. Figure 2.3b shows the oxygen signals with the Si background subtracted. (The small peak at higher energy is the non-resonant oxygen signal from the surface TiO_2 layer.) The height of Gaussian fits to the oxygen signals were used to determine the peak oxygen height, since the statistics of the peak were too poor (for these 20 minute, 88 μC He^{++} spectra) to allow a direct measurement of the height.

To calculate the oxygen content of the Ti samples before deuteridation, Eq. 2.6 is used with $x = 0$ since the deuterium concentration is assumed to be zero. For the two samples analyzed, the oxygen concentration was calculated to be 1.37±0.25 at%. The uncertainty is indicative of the uncertainties involved in subtracting the Si background, determining the oxygen peak height, and uncertainties in the stopping cross section factors. Stopping cross section values were calculated using the polynomial fit coefficients given in Table VI. of Ref. 5, except for that for oxygen, which was calculated using the "corrected" values for oxygen in solids given in Ref. 7. For the deuterided samples, the deuterium concentration x is not yet precisely known. However, y can be plotted as a function of x (Fig. 2.4 for sample Ti10 after deuteridation) and determined precisely when x has been determined.

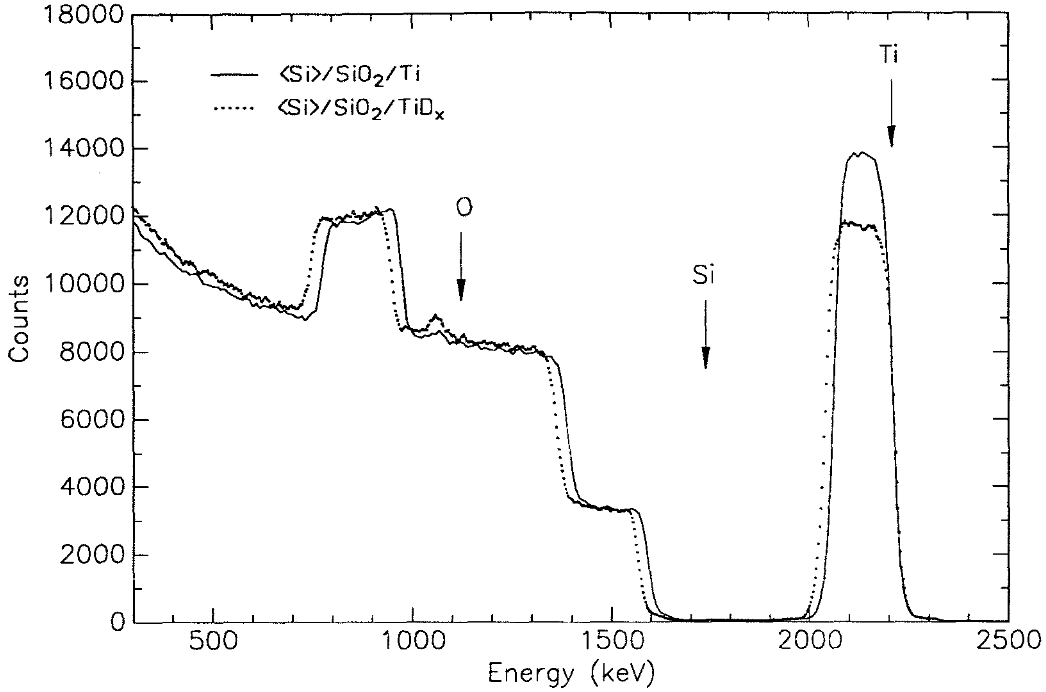

Figure 2.3a 3.08 MeV He^{++} backscattering spectra of sample Ti10 before and after deuteridation, with the 3.05 MeV oxygen resonance occurring at a depth of 80 nm.

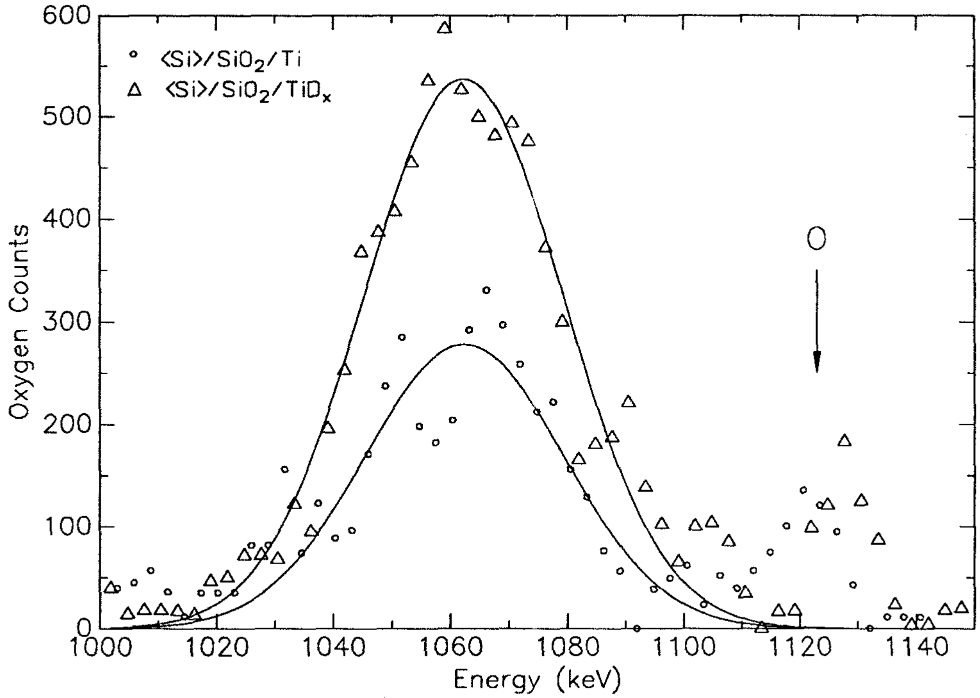

Figure 2.3b Background subtracted oxygen signals (data points) and Gaussian fits to oxygen resonance signals (lines) for the spectra shown in Fig. 2.3a.

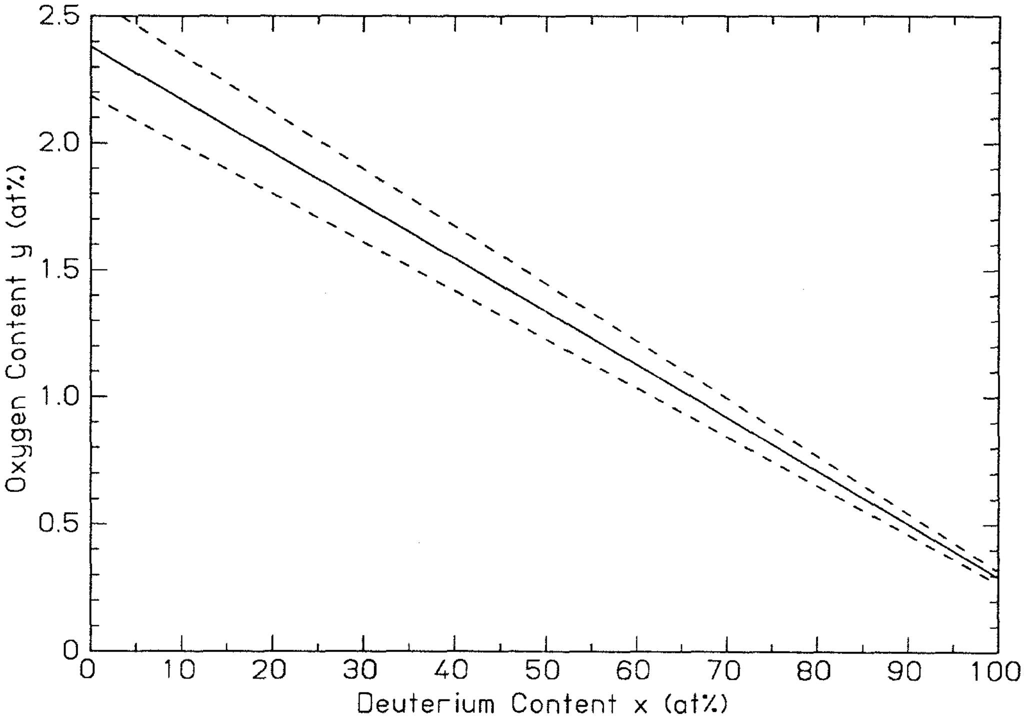

Figure 2.4 Oxygen concentration as a function of (assumed) deuterium concentration for sample Ti10 based on the peak height of the oxygen resonance signal and Eq. 2.6. The two dashed lines delineate the range of uncertainty in y.

2.2.2 Determination of Deuterium Concentration

Deuterium cannot be directly detected by He ion backscattering since its mass is less than that of He, and only atoms with mass greater than that of He will backscatter He. However, the presence of a sufficient quantity of deuterium in the Ti film can produce measurable changes in the Ti signal from that of pure Ti. The presence of deuterium decreases the Ti signal height and increases its width. The increase in width is caused by the additional electronic energy loss on both incoming and outgoing paths due to the deuterium. The height of the Ti signal is proportional to the areal density of Ti atoms encountered by the incident beam per unit energy loss. Any impurity atom which contributes to the energy loss will decrease the Ti signal height in proportion to the amount of energy loss it produces. Therefore, if the change in the Ti signal height is to be used to determine the deuterium concentration, the effects of all other impurity atoms in the sample must be taken into account.

From backscattering analysis, it appears that the only significant impurity is oxygen. Assuming the Ti film had the composition $Ti_{1-z}O_z$ before deuteridation and $Ti_{1-x-y}D_xO_y$ after deuteridation, the Ti signal heights will be

$$H_{Ti}^{TiDO} = (1-x-y)\sigma_{Ti}(E)\Omega Q \frac{\mathcal{E}}{[\varepsilon(E)]_{Ti}^{TiDO}\cos\theta_T} \tag{2.8a}$$

$$H_{Ti}^{TiO} = (1-z)\sigma_{Ti}(E)\Omega Q \frac{\mathcal{E}}{[\varepsilon(E)]_{Ti}^{TiO}\cos\theta_T}. \tag{2.8b}$$

If the same energy, energy calibration, tilt angle, and integrated charge are used for both samples, the ratio of the heights is simply

$$\frac{H_{Ti}^{TiDO}}{H_{Ti}^{TiO}} = \frac{1-x-y}{1-z}\,\frac{[\varepsilon(E)]_{Ti}^{TiO}}{[\varepsilon(E)]_{Ti}^{TiDO}}, \tag{2.9}$$

where $[\varepsilon(E)]_{Ti}^{TiDO}$ can be replaced by its form in Eq. 2.5 to explicitly show its dependence on x and y. Once the heights have been determined experimentally, and assuming z, and therefore $[\varepsilon(E)]_{Ti}^{TiO}$, is known, the relationship between x and y can be found using the formula

$$y = \frac{1 - x - \eta'\Big\{(1-x)[\varepsilon(E)]_{Ti}^{Ti} + x[\varepsilon(E)]_{Ti}^{D}\Big\}}{1 - \eta'\Big\{[\varepsilon(E)]_{Ti}^{Ti} - [\varepsilon(E)]_{Ti}^{O}\Big\}}, \quad \eta' = (1-z)\frac{H_{Ti}^{TiDO}}{H_{Ti}^{TiO}}\frac{1}{[\varepsilon(E)]_{Ti}^{TiO}}. \tag{2.10}$$

As expected, in this relation y decreases with increasing x. This function is clearly independent of Eq. 2.6; therefore, these two curves should intersect. The intersection point on the x-y plane indicates the deuterium and oxygen concentration of the sample.

Backscattering spectra using 2 MeV He^{++} were obtained for the same two Ti samples that were used to determine the oxygen content. Spectra were taken before and after the deuteridation process. All four spectra had the same energy calibration and the target tilt angle was 20° for all samples. The height of the Si signal from the SiO_2 layer of the substrate was used as a reference to insure that all spectra had the same integrated charge. A comparison of the spectra for sample Ti10 before and after deuteridation is shown in figure 2.5. The ratio $H_{Ti}^{TiDO}/H_{Ti}^{TiO}$ was determined to be 0.831 ± 0.004 for both samples.

Figure 2.6 is a plot of Eq. 2.10 using the values for sample Ti10, assuming z=1.37 (the value determined in the oxygen resonance analysis) and Eq. 2.6 (also for sample Ti10). The two curves intersect at x=62.8±2.3 at%, y=1.1±0.1 at%. The intersection point for the second sample is almost identical. Therefore, backscattering analysis shows the composition of the titanium deuteride samples to be $Ti_{0.36}D_{0.63}O_{0.01}$, or, ignoring the oxygen contamination, $TiD_{1.7\pm0.2}$.

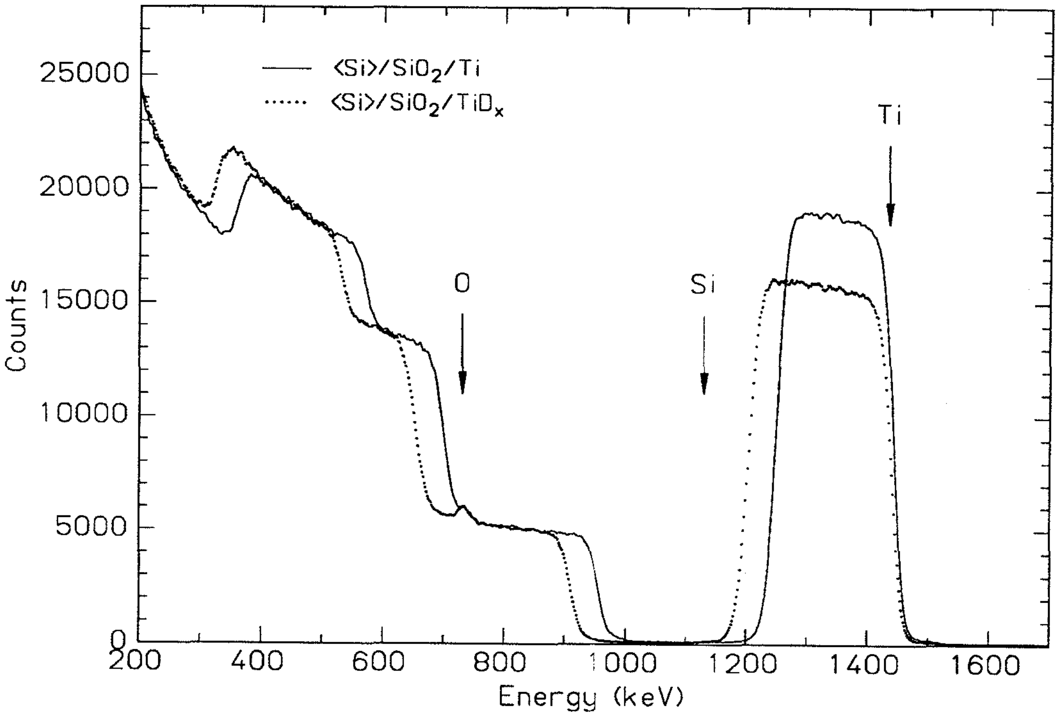

Figure 2.5 2 MeV RBS spectrum of sample Ti10 (tilted 20°) before and after deuteridation. Ti signal height decreases and width increases due to the energy absorption of deuterium.

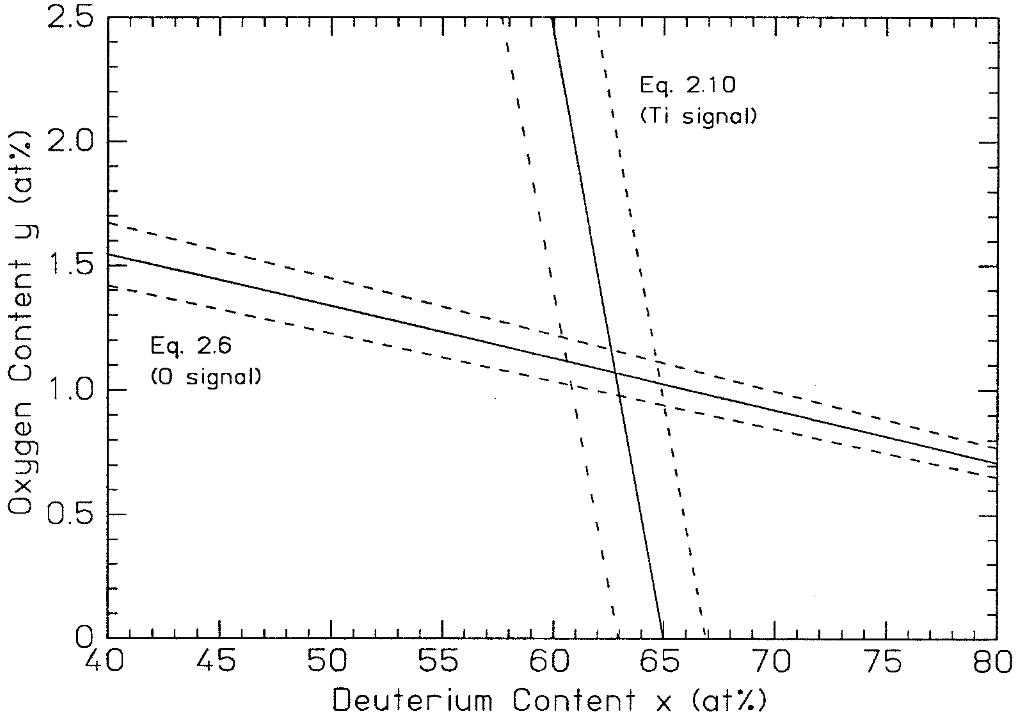

Figure 2.6 Intersection of Eq. 2.6 and Eq. 2.10 which determines oxygen and deuterium concentrations for sample Ti10. The intersection point indicates a composition of $Ti_{0.36}D_{0.63}O_{0.01}$. The dashed lines delineate the range of uncertainty for each equation.

2.3 X-Ray Diffraction Analysis of TiH Thin Films

X-ray diffraction was used to analyze a Ti sample before and after hydridation. The sample was hydrided with the exact procedure used for the titanium deuteride samples, except that hydrogen instead of deuterium was used. Backscattering analysis of the titanium hydride sample showed it to have a concentration nearly identical to that of the deuteride samples (i.e., $TiH_{1.7}$).

The hydride sample was analyzed instead of the deuteride sample so that a better comparison could be made to existing X-ray data. As can be seen on the Ti-H phase diagram (Fig. 2.7 [1]), the composition determined by backscattering analysis is within 1 at% H of the border between the fcc δ phase and the fct ε phase. From Ref. 1, at room temperature, the lattice parameter (a_0) increases linearly from 4.40 Åfor 60 at% H (the $(\alpha+\delta)/\delta$ boundary) to 4.44 Åfor 64 at% H (the δ/ε boundary). For the ε phase, a=4.51 Åand c=4.37 Åat room temperature for 65 at% H.

X-ray diffraction was performed using Co K_α (λ=1.7902Å) and a position sensitive detector [8]. The incident beam direction was 80° from the sample normal. Spectra were taken of the titanium hydride and an unhydrided Ti sample (Fig. 2.8). In the pure Ti spectrum, the <002> and <103> peaks of the pure Ti are seen, and indicate lattice spacings 0.5% larger than the tabulated values [1]. In the titanium hydride spectrum, there is one large peak, which is most likely the <111> peak, and three small peaks, which most likely correspond to <200>, <220>, and <311> reflections. The average lattice parameter calculated for the four peaks is 4.530±0.01 Å. This is 2% larger than that expected for the fcc δ phase, and 0.4% larger than the a spacing for the fct ε phase [9]. The peaks appear to be more consistent with the δ than the ε phase. The larger than expected lattice parameter may be due to the oxygen contamination.

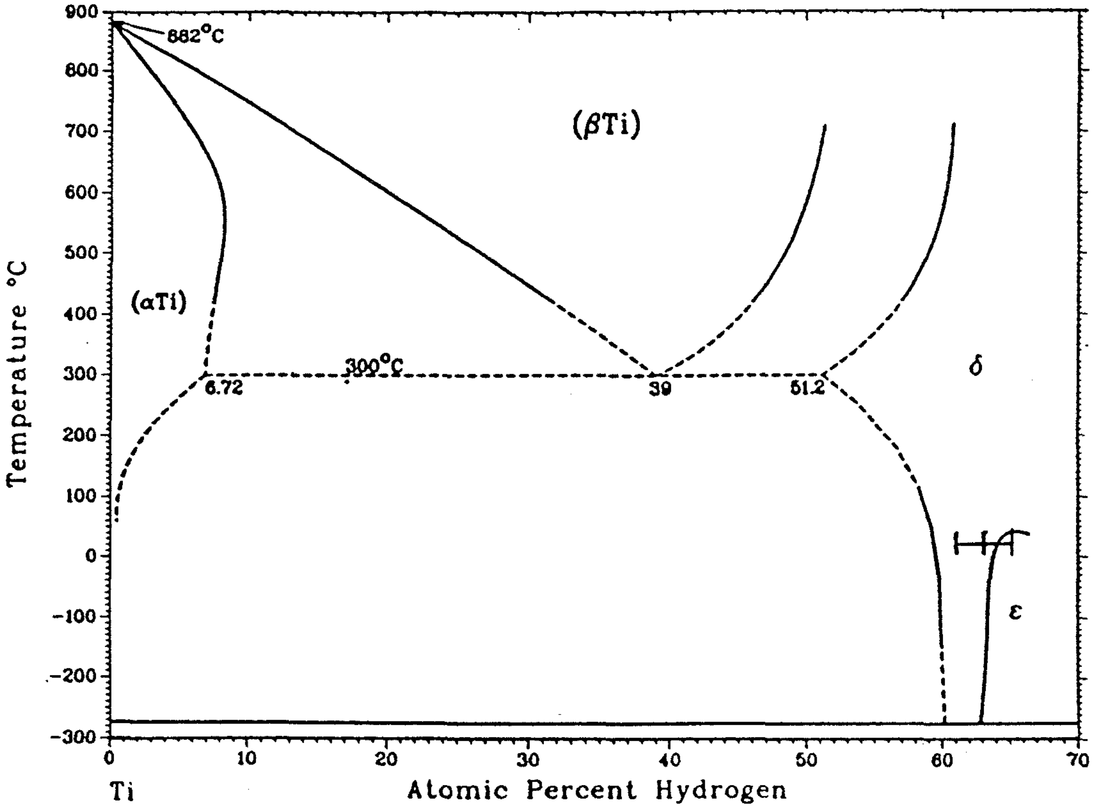

Figure 2.7 Ti–H phase diagram. The hydrogen concentration as determined by backscattering analysis (61±2 at%) is near the border between the fcc δ phase and the fct ε phase.

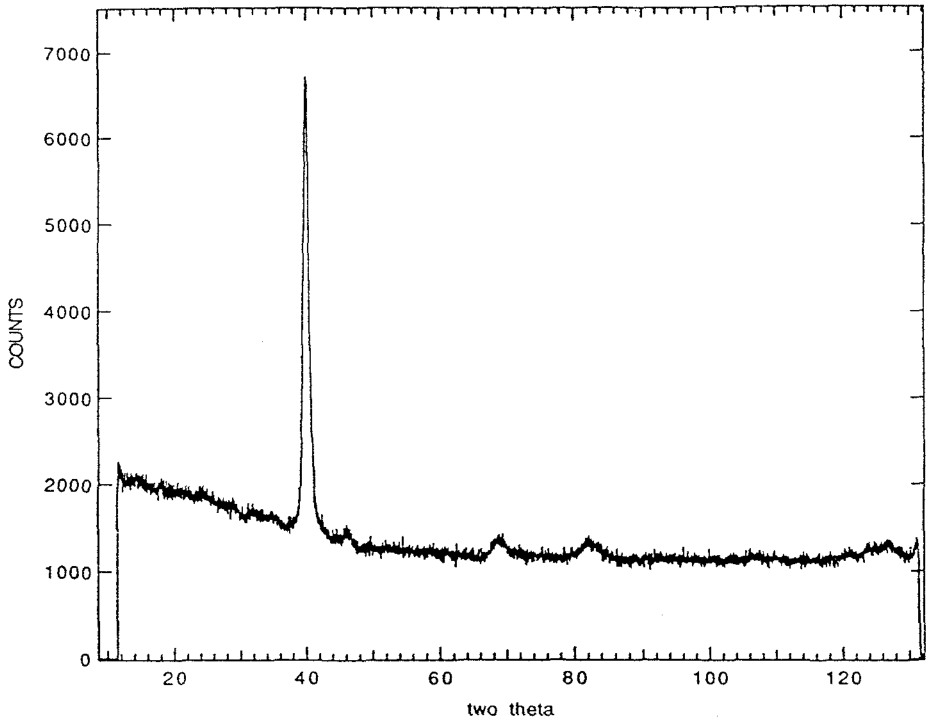

Figure 2.8a X-ray spectrum of pure Ti sample before hydridation.

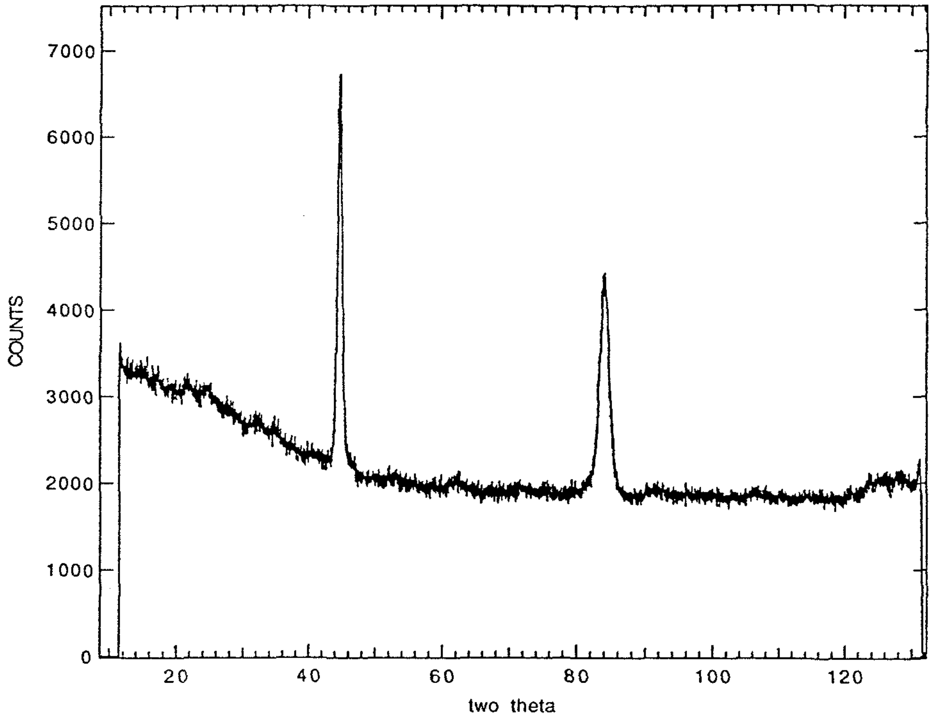

Figure 2.8b X-ray spectrum of Ti sample after hydridation to $TiH_{1.7}$. The peaks are consistent with an fcc structure with a lattice parameter of 4.530 Å.

References

[1] A. San-Martin and F. D. Manchester, Bull. Alloy Phase Diagrams **8**, 30 (1987).

[2] T. Smith, Surface Sci. **38**, 292 (1973).

[3] G. Mezey, J. Gyulai, T. Nagy, E. Kotai. and A. Manuada, *Ion Beam Surface Layer Analysis*, Vol. 1, O. Meyer, G. Linker, and F. Kappeler, eds., (Plenum Press, New York, 1976) p. 303.

[4] J. R. Cameron, Phys. Rev. **90**, 839 (1953).

[5] W. K. Chu, J. W. Mayer, and M-A. Nicolet, *Backscattering Spectrometry* (Academic Press, New York, 1978).

[6] B. Blanpain, P. Revesz, L. R. Doolittle, K. H. Purser, and J. W. Mayer, Nucl. Instrum. Methods **B 34**, 459 (1988).

[7] J. F. Ziegler and Y. K. Chu, J. Appl. Phys. **47**, 2239 (1976).

[8] J. Ballon, V. Comparat, and J. Pouxe, Nucl. Instrum. Methods **217**, 213 (1983).

[9] R. L. Crane and S. C. Chattoraj, J. Less-Common Met. **25**, 225 (1971).

Chapter 3

EXPERIMENTAL PROCEDURES AND RESULTS

The concept of the experiment is to irradiate a sample of titanium deuteride with a beam of heavy ions (Xe and Ar) with energies of a few hundred keV and to detect any fusion products (p, T, $^3He^+$, or n) of the D-D fusion reaction. By determining the number of fusion events per incident ion and the distribution of energies of the fusion products, information about the nature of the processes occurring during ion irradiation of titanium deuteride can be inferred. A silicon surface barrier detector was used to detect the protons, tritons, and ^3He. (It could not detect the neutrons since it detects only charged particles.) A neutron detector could have been used as well, but it would have been placed outside the target chamber, at a considerable distance from the sample. Also, the background neutron count rate (with no beam) was quite large (10–40 counts/minute) and highly variable. Therefore, the neutron detector was not used.

3.1 Experimental Setup

An Accelerators Incorporated 400MPR (400kV) ion implanter with a hot cathode source was used for the ion irradiation (Fig. 3.1). The ions are fully accelerated before mass analysis by a 30° analyzing magnet. Quadrupole lenses before and after the magnet provide beam focusing. After the second quadrupole lens, a 6° bend in the beamline removes neutral atoms. A two-stage x-y beam scanner raster scans the beam through a set of vertical and horizontal beam-defining slits onto the target. A bias of +275 V is applied to the target holder for secondary-electron

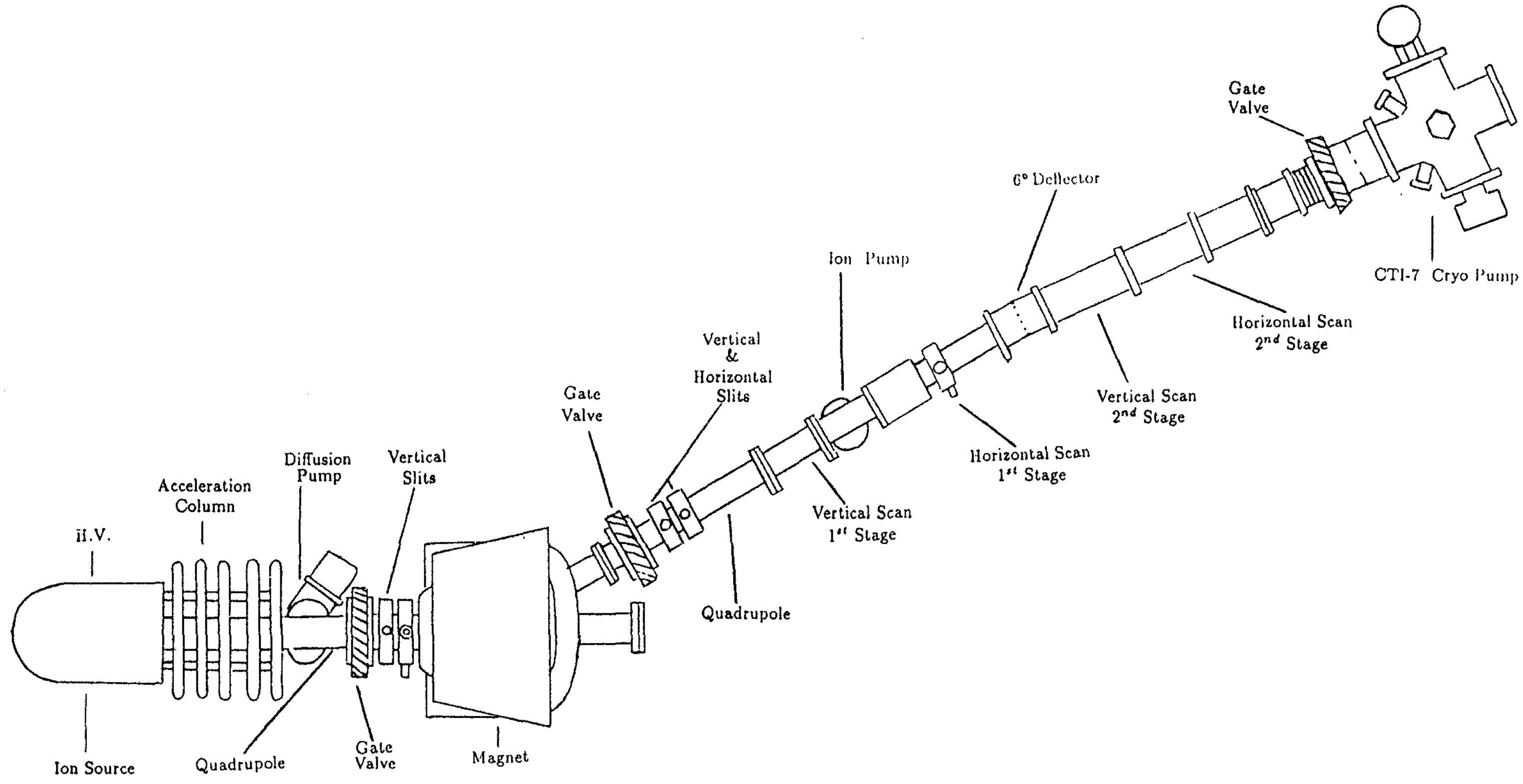

Figure 3.1 Schematic of 400MPR Ion Implanter used for ion irradiations.

suppression. The ion dose is measured by integrating the ion current hitting the sample using a BIC 1000C current integrator. The target chamber is pumped with a CTI-7 cryopump and liquid nitrogen cold shroud to a pressure of 1 x 10^{-7} Torr. The target holder contains a central cavity that can be filled with liquid nitrogen for sample cooling.

An Ortec silicon surface barrier detector with an active area of 0.25 cm^2 was used for detection of the fusion products. An Ortec 428 detector bias supply was used to provide a +50 V detector bias. Signal processing was accomplished using an Ortec 124A charge-sensitive preamplifier. an Ortec 572 spectroscopy amplifier (using a 1 μs shaping time), a Canberra 8075 100 MHz ADC, and a Canberra S100 multichannel analyzer (MCA).

The entire detection system was calibrated by placing the detector into the target chamber of the Pelletron 1 MV ion accelerator in a 170° backscattering configuration. Alpha particles of 2.814, 2.614, 2.328, and 1.725 MeV obtained by backscattering 3.05 MeV He^{++} ions from Au. Rh, Co, and Si samples, respectively, were used for the calibration. The incident beam energy was determined to within ~2 keV by maximizing the 3.05 MeV $^{16}O(\alpha,\alpha)^{16}O$ resonance signal from a ~6.5 nm surface SiO_2 layer on Si. The system energy resolution (FWHM) was determined to be 21.9 keV by measuring the 12%–88% width of the high energy edge of the backscattering spectrum of a thick (200 nm) gold layer. For the electronics chain settings used throughout the experiment, the energy calibration was determined to be 5.463 keV per channel with an offset of 23.345 keV.

The detector–sample geometry for the fusion experiment is shown in Figure 3.2. Samples were mounted on 0.125" thick aluminum plates using silicone heat conducting paste. The plates were bolted onto the hexagonal target holder, which could be rotated to choose between the six possible positions. The 1.2 x 1.2 cm sample

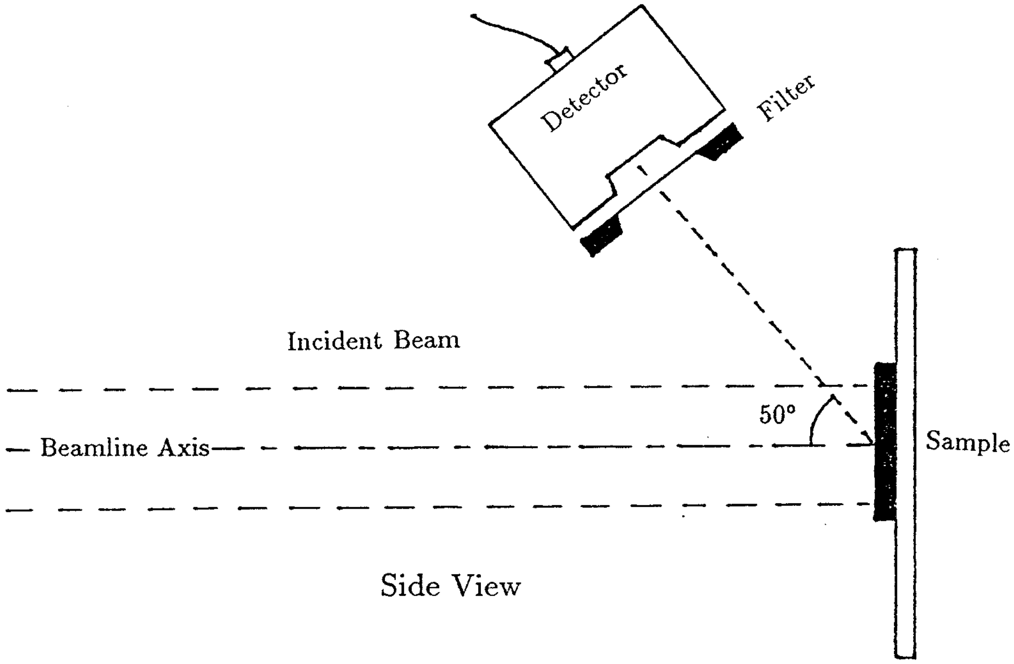

Side View

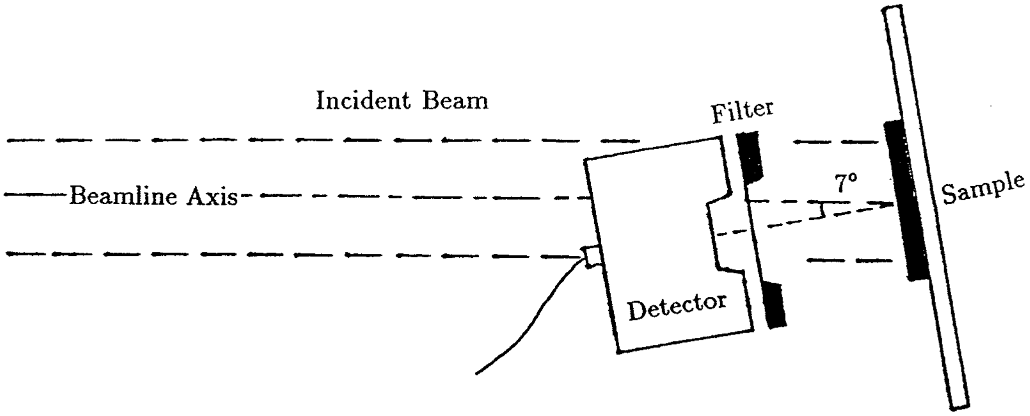

Top View

Figure 3.2 Top and side views of detector–sample geometry.

was positioned so that the center of the sample was on the beamline axis, with the sample normal tilted horizontally 7° from the beamline axis. The beam-defining slits were adjusted to irradiate a 1 x 1 cm region of the sample centered around the beamline axis. The detector was mounted on an assembly fixed to the top of the target chamber, i.e., it did not rotate along with the target holder. Two slightly different detector positions were used over the course of the experiment. In the first position, the center of the detector was 2.38±0.03 cm from the center of the sample, at an angle of 51° above the sample normal resulting in a 128.6° angle from the incident beam direction. In the second position, the center of the detector was 2.22±0.03 cm from the center of the sample. at an angle of 50° above the sample normal resulting in a 129.6° angle from the incident beam direction.

The detector solid angle was calculated as accurately as possible because the conversion from particles detected to particles emitted (assuming isotropic distribution) is inversely proportional to detector solid angle. Since the particles were not emitted from a point source, but over an area of 1 cm^2, the effective solid angle is the average of the solid angles over every point within the area emitting particles. For simplicity, it was assumed that the ion beam current was uniform over the entire sample area, so that no weighting was involved in the averaging process. The calculation was done by computer, with a grid size decreasing until no significant change in the solid angle resulted (1/80th cm x 1/80th cm). The calculated effective detector solid angle was 50.8±1.1 mSr for the first detector position and 44.1±1.0 mSr for the second detector position.

It was necessary to place a filter between the sample and the detector to prevent backscattered and sputtered ions from reaching the detector. If these particles were allowed to reach the detector, they would cause a low energy background signal which could overlap with the ^{3}He and T signals and cause noise in the detector that could affect the shape of all the peaks. The optimum filter thickness is one which minimally distorts the spectrum of the fusion products while stopping the maximum possible fraction of "undesired" particles (i.e., the thinnest filter able to stop all the "undesired" particles). The most penetrating of these particles is a sputtered deuteron. The maximum possible energy of a scattered deuteron is a function of the irradiating ion mass and energy. Of the irradiations studied in this experiment, 600 keV Ar^{++} produced the highest energy deuterons (109 keV). Considering that a deuteron can be reflected at any angle by a Ti atom and retain at least 85% of its energy, the maximum energy of a sputtered deuteron was approximately 90 keV.

Two different filters were used during the course of the experiment. The first was a 1.35 mg/cm^2 (5 μm) aluminum foil, which was far thicker than necessary to stop all undesired particles, but was readily available. In fact, it was so thick that it stopped the ^{3}He ions as well. However, the spectra obtained with this filter were absolutely assured of being free of background due to the sputtered and backscattered particles.

The second filter was a thin window of (LPCVD) Si_3N_4 in a $\langle Si \rangle$ substrate, designed to be optimally thin for 600 keV Ar^{++} irradiation. The process by which this filter was made is described in Appendix 1. The composition and thickness of the Si_3N_4 filter were determined by 2 MeV He^{++} backscattering analysis to be $Si_3N_{3.32}$ and 5.57 x 10^{18} atoms/cm^2 (190 μg/cm^2), respectively. Assuming a value of 3.44 g/cm^3 [1] for the specific gravity, this translates into a thickness of 540 nm. This thickness is thinner than that calculated necessary to stop all sputtered deuterons, but the fraction of sputtered deuterons with enough energy ($\sim$60 keV) to get through the filter is so small that their effect on the spectrum should be negligible. Moreover, the maximum energy of a deuteron after passing through the filter is $\sim$10 keV, which is significantly less than the system resolution, and much lower than the energy necessary to be counted by the MCA (due to the setting of the lower level discriminator on the ADC). Since this filter was not optically opaque, all viewports in the target chamber were closed to prevent light from reaching the detector, and it was visually verified that no target luminescence occurred during ion irradiation.

3.2 Experimental Procedures

Two sets of experiments were performed: one with the thick Al foil filter, and the other with the thin Si_3N_4 filter. The titanium deuteride samples were irradiated with 140, 250, 400, and 500 keV Ar, and 250 keV Xe while using the Al filter; and 150, 300, 450, and 600 keV Ar. and 200, 300, and 500 keV Xe while using the Si_3N_4 filter. Ion doses ranged from 1.5 x 10^{16} to 5.2 x 10^{17} ions/cm^2 for irradiation durations of 1 to 7.5 hours. Beam currents ranged from 0.4 to 12.0 μA for the 1 cm^2 area irradiated. During irradiation, the samples were kept at liquid nitrogen temperature to minimize any radiation-enhanced diffusion or desorption of deuterium from the sample surface. The accuracy of the current integration was checked by implanting the beam into a piece of Si immediately before and after the experiment and later measuring the dose by backscattering spectrometry.

Each titanium deuteride sample was loaded onto the target holder along with two pieces of $\langle 111 \rangle$ Si of similar size. The target chamber was pumped down to the base pressure of 1 x 10^{-7} Torr, and the target holder (containing all three samples) was cooled to liquid nitrogen temperature ($\sim -180°$C). A beam of the desired ion and energy was obtained, maximized, and checked for stability. Once a stable beam was achieved, the first Si calibration sample was irradiated to a dose of 1.0 x 10^{16} ions/cm^2. After the first calibration, the titanium deuteride sample was moved into place. Windows (regions of channels) were set up on the MCA where the fusion products were expected to appear. During the first 10 minutes of irradiation, these windows were modified (if necessary) to minimize background counts within the windows while insuring that all legitimate fusion products were within the window boundaries. Once the irradiation started, the integrated charge and counts within the proton, triton, and (for the Si_3N_4 filter) ^{3}He windows, were recorded at five minute intervals for the duration of the experiment. Also, the fusion spectrum was saved at 30 minute intervals so that comparisons of peak shapes over the course of the experiment could be made. The irradiation was continued until sufficient statistics were collected to accurately determine the fusion yield or until the fusion yield dropped significantly (indicating that most of the titanium deuteride layer had been sputtered away).

After the irradiation of the titanium deuteride sample was completed, the second Si calibration sample was moved into place and irradiated to a dose of 1×10^{16} ions/cm^2 under the same beam conditions as the titanium deuteride sample. The target holder was warmed up to room temperature, and the samples were removed. When all samples for the given run (Al filter or Si_3N_4 filter) had been completed, all samples (titanium deuteride and Si calibration) were analyzed by 2 MeV and 3 MeV backscattering spectrometry. The RBS measurement of the ion dose in the Si samples was used to correct the ion dose determined by the integrated charge, and the fusion yield was calculated for each irradiation.

In all, twelve irradiations were performed on seven $TiD_{1.7}$ samples. Table 3.1 below lists the irradiations performed for each sample (in the order that they occurred), ion dose for each irradiation, and filter used. For samples which were irradiated more than once, the higher energy. lower dose irradiation was performed first to minimize the effect of the previous irradiations on the subsequent ones.

Table 3.1 Ion Irradiations performed on each $TiD_{1.7}$ sample.

Sample	Ion	Energy (keV)	Dose (ions/cm^2)	Duration (hours)	Filter
Ti4	Xe	250	5.20×10^{17}	7.0	Al
Ti5	Ar	250	3.78×10^{17}	4.0	Al
Ti6	Ar	500	5.20×10^{16}	5.5	Al
	Ar	400	6.26×10^{16}	5.5	Al
Ti7	Ar	140	5.20×10^{17}	6.0	Al
Ti9	Ar	600	1.95×10^{16}	2.0	Si_3N_4
	Ar	450	2.45×10^{16}	2.0	Si_3N_4
	Ar	300	2.69×10^{17}	1.0	Si_3N_4
	Ar	150	3.05×10^{17}	2.0	Si_3N_4
Ti10	Xe	200	4.47×10^{17}	7.5	Si_3N_4
Ti11	Xe	500	1.53×10^{16}	3.0	Si_3N_4
	Xe	300	2.09×10^{17}	3.0	Si_3N_4

Two types of measurements were made to determine the background spectrum. The first type of measurement was to take a spectrum without ion irradiation for a duration of 7 to 40 hours. (A typical spectrum is shown in Fig. 3.3a.) This background measurement indicates the background due to detection-system noise. There was no discernable difference between the "no-beam" spectra taken with and without the titanium deuteride sample present. The number of background counts increased linearly with acquire duration, with a count rate of 17±3 counts per hour. Almost all counts had an energy of less than 700 keV, and no background count was ever detected with an energy greater than 2 MeV.

The second type of measurement was to take a spectrum during the irradiation of titanium hydride (not deuteride) with 250 keV Xe^+. No nuclear reactions are expected from this irradiation. One irradiation of 6.0×10^{16} ions/cm^2 over a duration of 75 minutes was performed (Fig. 3.3b). There was no significant difference between this spectrum and a spectrum taken for a similar duration with no beam. Therefore, the ion irradiation itself did not appear to contribute to the background.

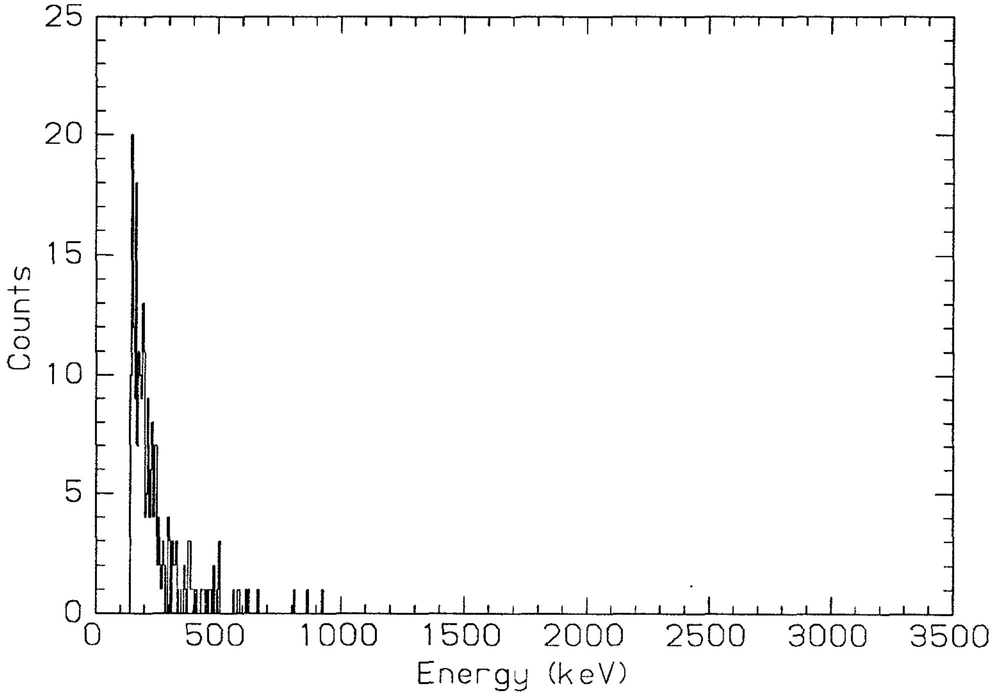

Figure 3.3a Background spectrum taken with no beam and no $TiD_{1.7}$ sample over a duration of 14 hours. Background count rate = 18 counts/hour.

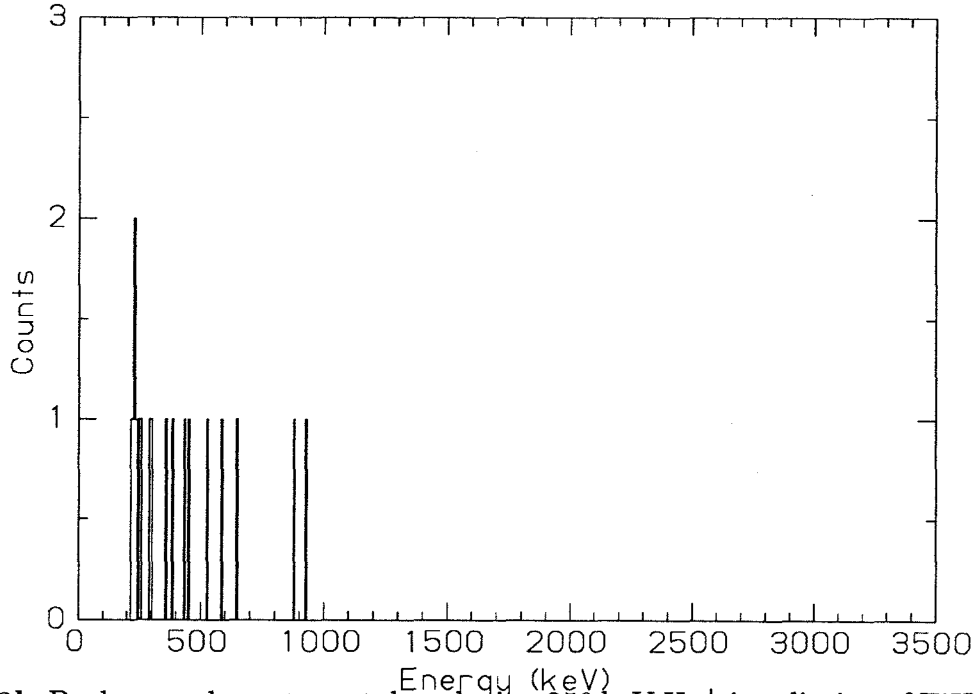

Figure 3.3b Background spectrum taken during 250 keV Xe^{+} irradiation of $TiH_{1.7}$. Total ion dose = 6.0×10^{16} ions over a duration of 75 minutes. Background count rate = 15 counts/hour.

3.3 Experimental Results

3.3.1 Al Filter Results

Spectra obtained using the 5 μm Al filter contained two broad peaks with roughly equal areas corresponding to 3.02 MeV protons and 1.01 MeV tritons from the D(d,p)T nuclear reaction. The energies of the detected protons and tritons are reduced from these values by a few hundred keV due to the energy lost in the Al filter and due to a Doppler shift (since the center of mass velocity of the deuterons usually contains a component into the sample and thus away from the detector). The 0.82 MeV ^{3}He ions produced by the D(d,n)^{3}He reaction did not have enough energy to penetrate the Al filter, and so were not detected. The spectrum obtained by irradiating $TiD_{1.7}$ with 400 keV Ar^{++} ions to a dose of 5.12 x 10^{16} ions is shown in figure 3.4. It can be seen that the low energy edge of the triton peak is cut off. This is due to the lower level discriminator (of the ADC), which was set to cut off the majority of the background counts caused by noise in the detector and preamplifier.

The region between the proton and triton peaks contains a uniform background that scaled linearly with the counts in the proton peak. This background was not present in the spectrum obtained by irradiation of the titanium hydride sample, and is, therefore, due to the fusion events. The most likely source of this background is protons created by the fusion reaction that were either scattered before entering the detector or entered the detector through a varying amount of epoxy surrounding the central area of the detector. Since these particles were not originally emitted toward the direction of the detector solid angle, this background was not included in the number of protons detected that was used to calculate the fusion yield.

The information obtained by recording the ion dose, proton counts, and triton counts (within their respective windows) at five minute intervals can best be

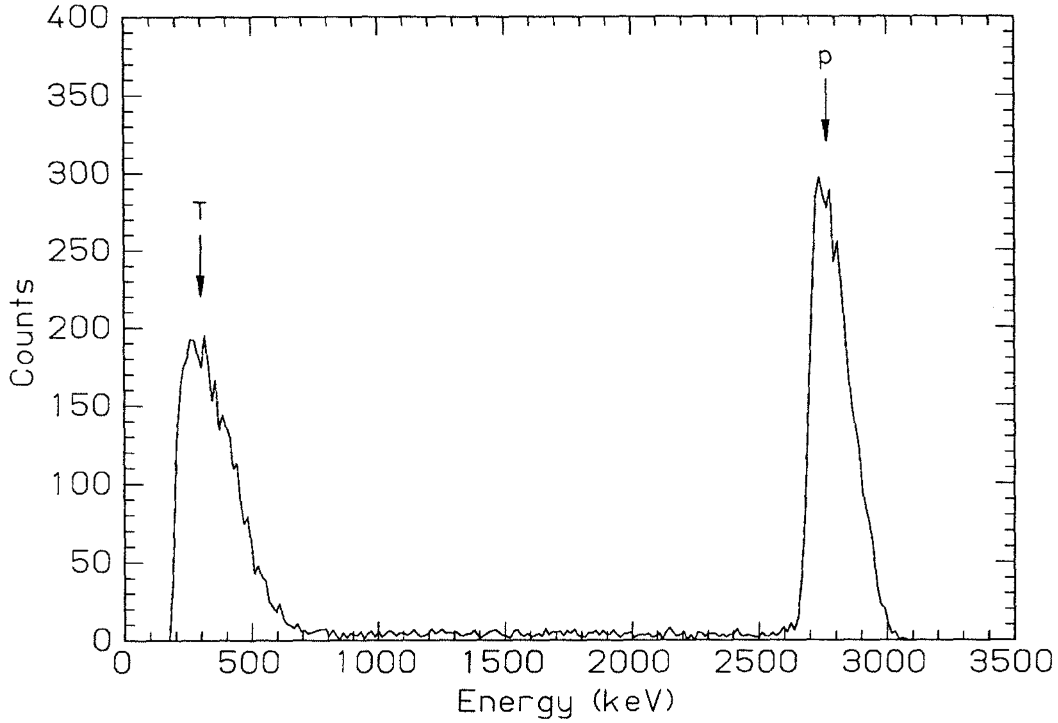

Figure 3.4 Spectrum obtained by irradiating $TiD_{1.7}$ with 5.12×10^{16} 400 keV Ar^{++} ions over a duration of 5.5 hours. A 5 μm Al filter was placed in front of the detector to block sputtered and backscattered particles. The detector was placed at an angle of 129° from the incident beam direction and subtended a solid angle of 44.1 mSr.

conveyed in graphic form. Figure 3.5 contains the recorded values for the case of 400 keV Ar^{++} irradiation. Proton and triton counts are plotted versus ion dose instead of time because it is the ratio of proton counts to incident ions (not time) that is used to determine the fusion yield. Also plotted are the computed time derivative of the ion dose (instantaneous ion current), and the derivative of the proton and triton counts with respect to ion dose (instantaneous detected fusion yield). These plots were used to determine if any significant change in the fusion yield occurred over the course of the irradiation (which would indicate a change in the sample composition).

In two of the five irradiations there was a significant drop in the number of proton and triton counts per incident ion over the course of the irradiation. These two irradiations were 250 keV Xe^{+} and 140 keV Ar^{+}, which had the highest sputtering coefficients and shortest projected ranges of the five irradiations. Both displayed a drop in fusion yield at the beginning of the irradiation, a leveling off, and a drop to nearly zero at the end of the irradiation. The drop at the end of the experiment could be definitely related to the near complete removal of the titanium deuteride layer by sputtering. It is conjectured that the initial drop in the fusion yield was due to the dilution of the deuterium concentration by the addition of the irradiating species, and that the leveling off occurred when a steady-state concentration profile was achieved. No significant drop in fusion yield occurred in the other three irradiations because the samples were not irradiated to the point where the deuterium concentration was significantly diluted. Enough statistics were obtained to calculate the fusion yield before this point was reached. A second possibility is that ion irradiation caused the desorption of deuterium in the cases where the fusion yield decreased; however, current models of heavy-ion-induced desorption of deuterium from titanium [2,3] do not explain the results observed in this experiment.

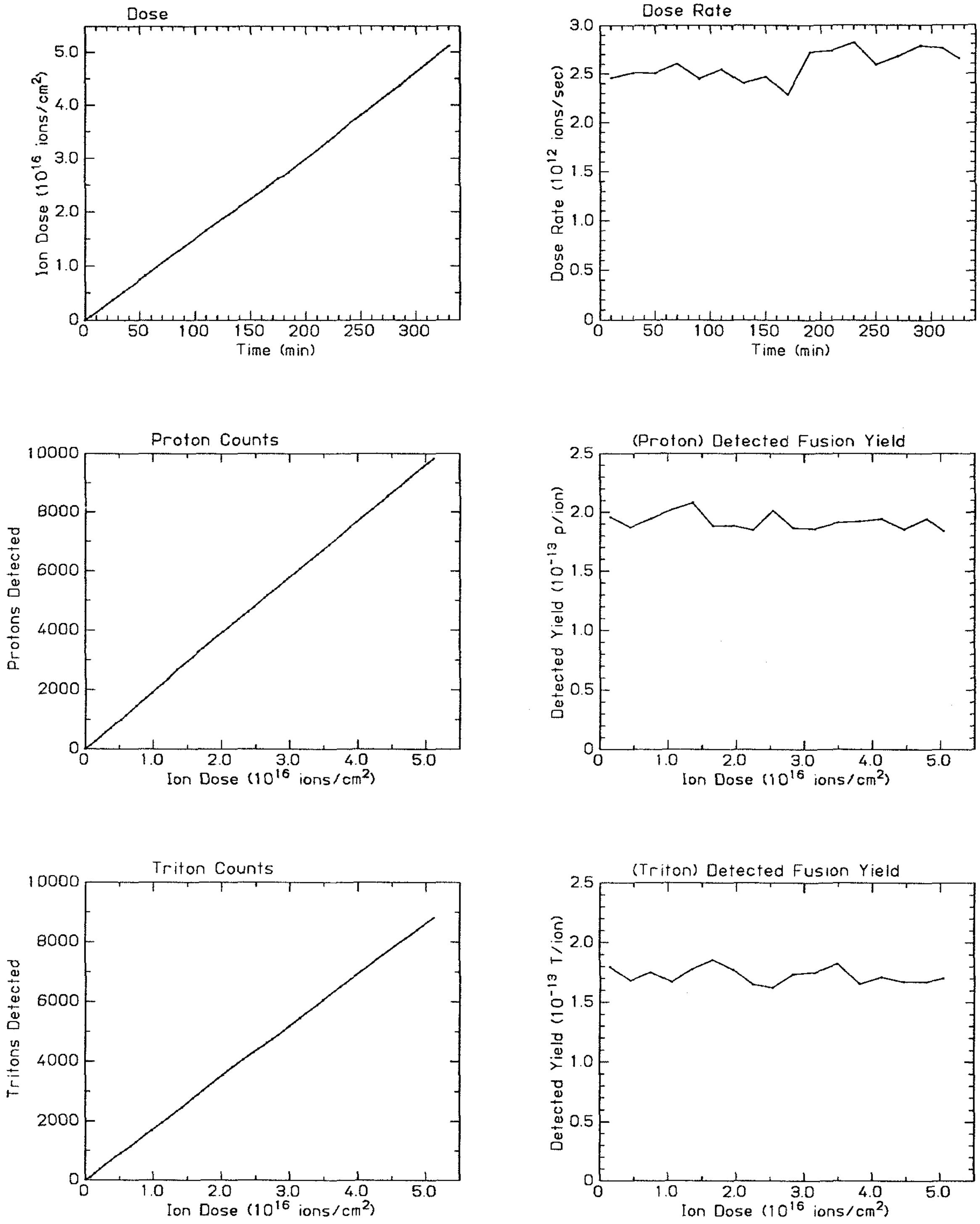

Figure 3.5 Record of ion dose and proton and triton counts taken during 400 keV Ar^{++} irradiation of $TiD_{1.7}$.

The fusion yield (fusion events per incident ion) for each irradiation was calculated using the formula

$$Y = \frac{Y_{det}}{I_{corr}}\frac{4\pi}{\Omega_{det}}, \tag{3.1}$$

where Y is the fusion yield, Y_{det} is the detected fusion yield (i.e., fusion events detected per incident ion), I_{corr} is the correction to the ion dose as determined by backscattering analysis of the Si calibration samples, and Ω_{det} is the detector solid angle (44.1 mSr for these irradiations). The formula assumes that the angular distribution of reaction products is isotropic. This assumption is reasonable for deuteron energies $\lesssim$30 keV (Lab frame) [4]. The ion dose in the Si calibration samples was measured using 3 MeV He^{++} backscattering analysis. A target tilt angle of 7° was used to avoid channeling. The ion dose measured by backscattering analysis was 5±3 percent greater than that measured by charge integration for all Si calibration samples. Therefore, a value of I_{corr}=1.05 was used in Eq. 3.1 for all irradiations.

In calculating the detected fusion yield (Y_{det}), only the proton peak was considered. Using the triton peak could not have yielded as accurate a result as using the proton peak because the triton peak was partially cut off and the region of the triton peak also contained background from both deflected protons and detection-system noise. For the cases where the detected fusion yield remained fairly constant throughout the irradiation, the precise value of Y_{det} was determined by the slope of the least-squares fitted line to the number of protons detected as a function of the number of incident ions. For the cases where the fusion yield dropped over the course of the irradiation, only the portion of the irradiation before the drop in detected fusion yield was used in the least-squares fitting procedure. The fusion yields calculated using Eq. 3.1, along with experimental parameters, are shown in Table 3.2.

Table 3.2 Experimental fusion yields for irradiations using the 5μm (1.35 mg/cm^2) Al filter, determined using Eq. 3.1. Ion dose and proton counts are listed to show the statistics available for the calculation.

Ion	Energy (keV)	Dose (ions/cm^2)	Proton Counts	Fusion Yield (fusion events/ion)
Xe	250	4.04 x 10^{16}	69	(4.82±0.72) x 10^{-13}
Ar	140	1.38 x 10^{17}	570	(1.35±0.14) x 10^{-12}
Ar	250	3.78 x 10^{17}	16643	(1.29±0.13) x 10^{-11}
Ar	400	6.26 x 10^{16}	9827	(5.32±0.54) x 10^{-11}
Ar	500	5.20 x 10^{16}	23712	(1.03±0.10) x 10^{-10}

3.3.2 Si_3N4 Filter Results

The spectra obtained using the thin Si_3N4 filter differed from those obtained using the Al filter in that the ^{3}He ions were also detected and that the reduction of the peak energies was smaller due to the smaller energy loss in travelling through the Si_3N4 filter. Even though the energy loss and energy straggling in traversing the Si_3N_4 filter was only ~15% of that for the Al filter, the proton and triton peak shapes (FWHM) were quite similar to those obtained with the Al filter for irradiations of the same ion and similar energy.

The spectrum obtained during irradiation with 500 keV Xe^{++} (which is typical of all spectra obtained using the Si_3N_4 filter) is shown in figure 3.6. The region between the proton and triton windows contains a uniform background similar to that obtained with the Al filter. Figure 3.7 contains plots of the recorded values of the ion dose, and proton, triton, and ^{3}He counts, and their respective derivatives over the course of the 500 keV Xe^{++} irradiation.

Of all the irradiations with the Si_3N_4 filter, only the 150 keV Ar^+ and 300 keV Xe^+ irradiations displayed a decrease in the detected fusion yield over the course of

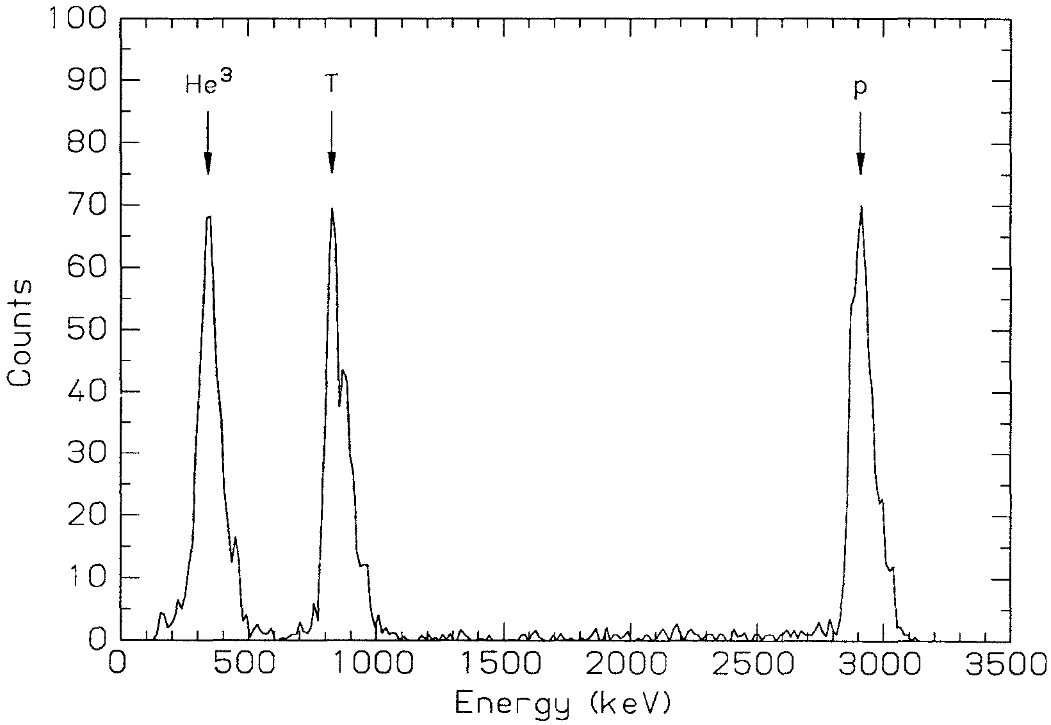

Figure 3.6 Spectrum obtained by irradiating $TiD_{1.7}$ with 1.53×10^{16} 500 keV Xe^{++} ions over a duration of 3 hours. A 540 nm Si_3N_4 filter was placed in front of the detector to block sputtered and backscattered particles. The filter was thin enough to allow the 0.82 MeV ^3He to reach the detector. The detector was placed at an angle of 130° from the incident beam direction and subtended a solid angle of 50.8 mSr.

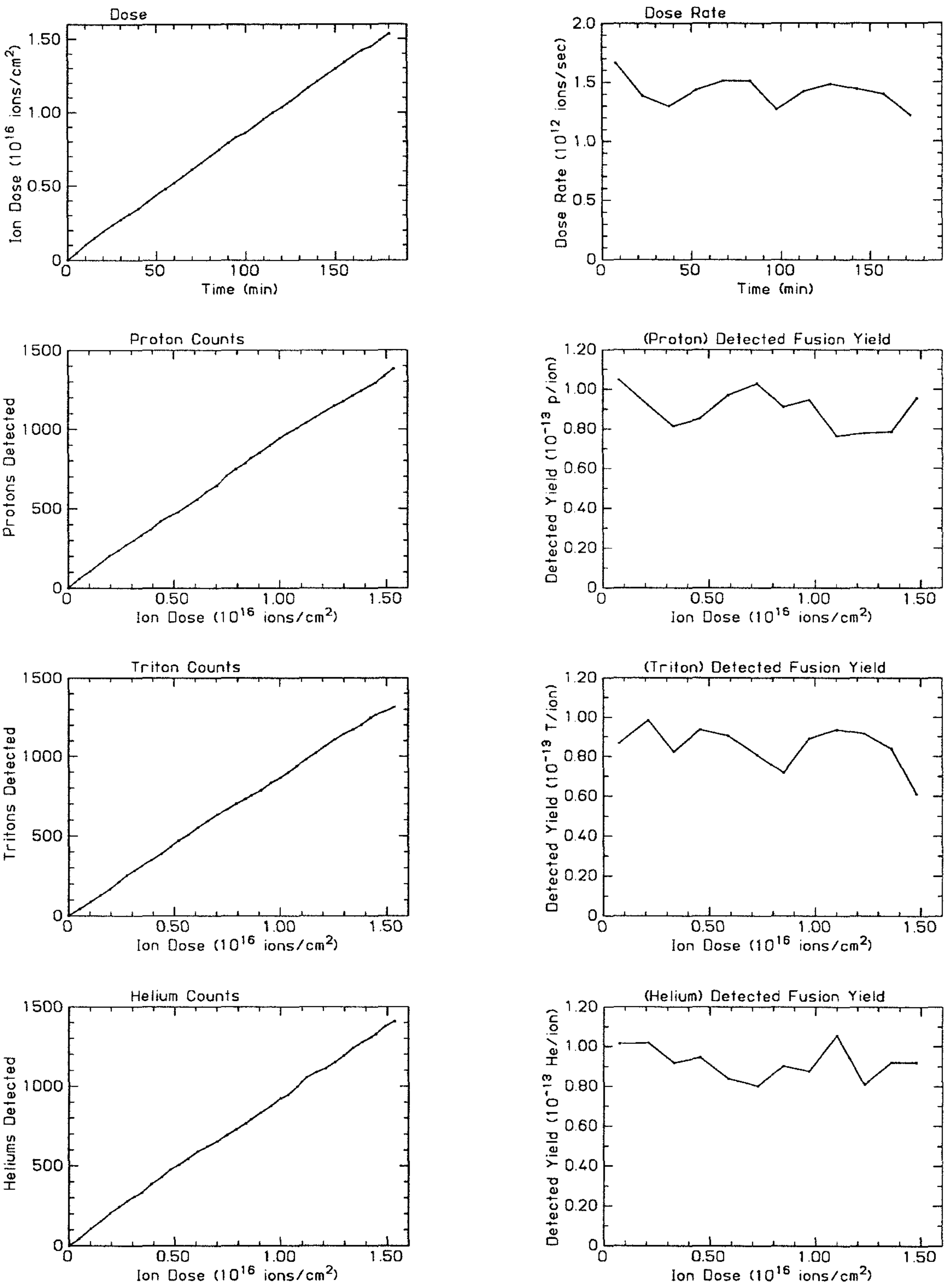

Figure 3.7 Record of ion dose and proton. triton, and ^{3}He counts taken during 500 keV Xe^{++} irradiation of TiD$_{1.7}$.

the irradiation. It is suspected that the detected fusion yield of the 200 keV Xe^+ irradiation also decreased, since both the 250 and 300 keV Xe^+ irradiations did, but the poor proton count statistics made this difficult to determine.

In calculating the detected fusion yield (Y_{det}), again, only the proton peak was considered. Although the triton and ^{3}He peaks were not cut off (except for ^{3}He for 600 keV Ar^{++}), the regions of those peaks still contained background from both deflected protons and detection-system noise. Just as for the Al filter, when the detected fusion yield remained fairly constant throughout the irradiation, the precise value of Y_{det} was determined by the slope of the least-squares fitted line to the plot of the number of protons detected as a function of the number of incident ions; and when the fusion yield dropped over the course of the irradiation, only the portion of the irradiation before the drop in detected fusion yield was used in the least-squares fitting procedure. The correction to the ion dose (I_{corr}) varied from 1.02 (for all Ar irradiations) to 1.14–1.26 (for the Xe irradiations). The fusion yields calculated using Eq. 3.1 are listed in Table 3.3, and plotted, along with the fusion yields obtained using the Al filter, in figure 3.8.

Table 3.3 Experimental fusion yields for irradiations using a 540 nm (190 $\mu g/cm^2$) Si_3N_4 filter, determined using Eq. 3.1. Ion dose and proton counts are listed to show the statistics available for the calculation.

Ion	Energy (keV)	Dose (ions/cm^2)	Proton Counts	Fusion Yield (fusion events/ion)
Xe	200	4.47×10^{17}	174	$(8.3 \pm 1.7) \times 10^{-14}$
Xe	300	3.70×10^{16}	219	$(1.24 \pm 0.18) \times 10^{-12}$
Xe	500	1.53×10^{16}	1381	$(1.80 \pm 0.18) \times 10^{-11}$
Ar	150	1.84×10^{17}	1315	$(1.73 \pm 0.17) \times 10^{-12}$
Ar	300	2.69×10^{17}	32291	$(2.96 \pm 0.30) \times 10^{-11}$
Ar	450	2.45×10^{16}	7943	$(7.94 \pm 0.80) \times 10^{-11}$
Ar	600	1.95×10^{16}	15346	$(1.92 \pm 0.20) \times 10^{-10}$

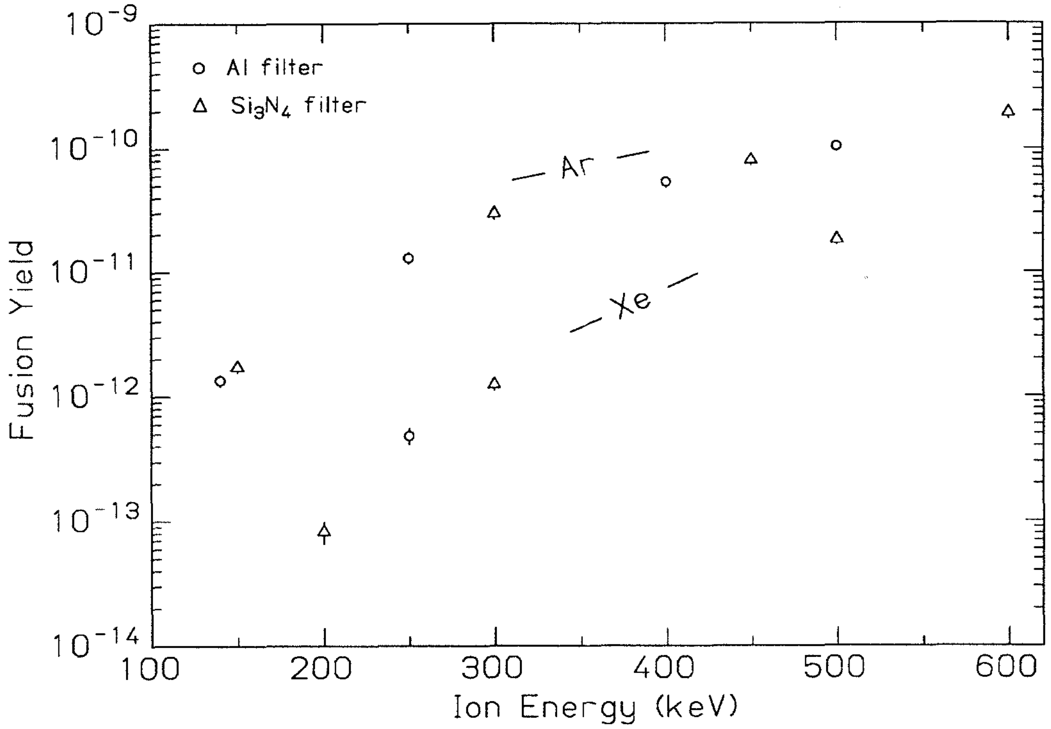

Figure 3.8 Experimental fusion yields for Ar and Xe irradiation of $TiD_{1.7}$ using an Al filter (○) or a Si_3N_4 filter (△) in front of the detector.

References

[1] R. C. Weast, ed., *CRC Handbook of Chemistry and Physics* **59** (CRC Press, Florida, 1978) p. B-161.

[2] M. Schluckebier, Th. Pfeiffer, K. Muskalla, W. Schmülling, and D. Kamke, Appl. Phys. **A 42**, 19 (1987).

[3] M. Schluckebier, Th. Pfeiffer, K. Muskalla, W. Schmülling, and D. Kamke, Appl. Phys. **A 42**, 179 (1987).

[4] A. Krauss, H. W. Becker, H. P. Trautvetter, and C. Rolfs, Nucl. Phys. **A 465**, 150 (1987).

Chapter 4

BINARY COLLISION CASCADE MODEL OF FUSION YIELD

4.1 Introduction

To identify the processes which cause the fusion events during ion irradiation, the experimental fusion yield must be compared to predictions based on the different processes suspected of causing the fusion events. At the outset of the experiment, two possible mechanisms for producing fusion events were considered: high energy deuteron recoils in the early stages of the collision cascade and, although unlikely, "cold fusion" processes in the thermal spike regime at the end of the cascade. As no models of the "cold fusion" processes or values of "cold fusion" cross sections are available, no realistic predictions of fusion yields for "cold fusion" processes can be made. On the other hand, the early stages of the collision cascade caused by an energetic ion (>1 keV) are believed to be well understood (see Section 1.2). Well established models exist [1,2], and are regularly used to predict implanted ion profiles (projected range and straggling), sputtering coefficients, and defect concentration profiles [3,4]. Therefore, the first step is to calculate the fusion yields expected based on a binary collision cascade model and compare them with the experimental fusion yields. Only if the experimental yields are significantly higher than those predicted by the binary collision cascade model would there be any need to consider additional processes (such as "cold fusion") to account for the experimental results.

Given that it is the collision cascade process that is to be modelled, there are several possible methods that can be used to calculate the fusion yield. Perhaps the simplest method would be to use a Monte-Carlo simulation. I have already written such a code for the calculation of ion ranges and energy deposition profiles, which could have been modified (with only some small difficulties) to include the fusion cross sections. However, the fact that the experimental fusion yields are on the order of 10^{-10}–10^{-14} fusion events per incident ion makes the task of collecting sufficient statistics quite daunting. Therefore, a method of calculating the fusion yields analytically is preferable.

I have used two analytical methods for calculating the fusion yield. The fusion yield is expressed as a finite sum of integrals, which can be solved numerically. The first method begins with the D–D reaction and works backwards through the collision cascade until the incident ion is reached. The second begins with the incident ion and follows the collisions until a D–D reaction occurs. Both give identical values for the fusion yield for a given irradiation and take about the same time to compute (~2 hours on the μVAX). The first method allows calculation of the fusion yields for all incident ion energies up to the desired value in a single run, while the second method gives the fusion yield for only one incident energy per run. However, the second method can be used to obtain information about the distributions of energies for each type of atom in the sample for every generation in the collision cascade. In this chapter, the first method will be discussed. The second method will be discussed briefly in chapter 5.

4.2 Representation of the Collision Cascade

As the incident ion penetrates the target material, it transfers its energy to target atoms and electrons in nuclear and electronic collisions until it comes to rest. The first generation recoils (those atoms struck by the incident ion) undergo a similar energy loss in transferring their energy to the second generation recoils, and so on. Each atom involved in the collision cascade can be labelled by starting with the incident ion and listing the atoms from each generation leading directly to the transfer of energy to the atom to be labelled. Therefore, for Xe ion irradiation of titanium deuteride, all first generation recoils are labelled either Xe–Ti or Xe–D, no matter how many collisions the Xe ion had undergone before striking the labelled atom. Second generation recoils are labelled Xe–D–D, Xe–D–Ti, Xe–Ti–D, or Xe–Ti–Ti. Third and higher generation recoils are labelled similarly. The label can be thought of as either a label of the atom or a label of the chain of collisions that directly led to the transfer of energy to the atom. Each chain label is general in that it does not specifically state the amount of energy transferred in each collision; it represents all possible energy transfers for that series of collisions. Therefore, a generalized collision cascade which encompasses all possible collision cascades for the given ion and target combination can be described as a set of these chains.

For a fusion event to occur, energy must be transferred to a deuteron, which in the course of its displacement must strike a second deuteron and cause a fusion reaction. Therefore, each collision chain resulting in a fusion reaction must begin with the incident ion and end with a deuteron striking another deuteron. For Xe irradiation of titanium deuteride, the simplest chain leading to fusion is Xe–D–D. More complicated chains include Xe–Ti–D–D, Xe–D–D–D, Xe–Ti–Ti–D–D, Xe–D–Ti–D–D, and so on, where the final D–D indicates the fusion reaction. If the fusion yield for each chain can be found, the total fusion yield due to the incident ion is found by summing the fusion yields of each type of chain:

$$Y_{\mathrm{Xe}} = Y_{\mathrm{XeDD}} + Y_{\mathrm{XeTiDD}} + Y_{\mathrm{XeDDD}} + Y_{\mathrm{XeTiTiDD}} + Y_{\mathrm{XeTiDDD}} + \ \ldots\ , \qquad (4.1)$$

where Y_{Xe} is the total fusion yield, and $Y_{\mathrm{Xe}\cdots}$ is the fusion yield for the chain $Xe\cdots$. The chains are listed in order of simplicity, starting with the chain involving the fewest generations (or intermediate collisions).

If the fusion yield for a chain did not decrease with the number of intermediate collisions, the sum would be over a very large number of chains. However, collisions between unlike atoms can transfer only a fraction of the original atom's energy to the next atom, and in collisions between like atoms, the likelihood of a 100% energy transfer is quite small. Therefore, as the number of intermediate collisions increases, the energy transferred to the penultimate deuteron becomes smaller and smaller. Since the D(d,p)T fusion cross section decreases extremely rapidly with decreasing energy (for the range of deuteron energies produced in this experiment), increasing the number of intermediate collisions in a chain will decrease the fusion yield of the chain. There is one special case (which will be explained later) where adding one intermediate collision can increase the fusion yield of the chain, but, for all others,

$$Y_{Xe\Sigma DD} > Y_{Xe\Sigma\Sigma' DD} \ , \ Y_{Xe\Sigma'\Sigma DD} \ , \tag{4.2}$$

where Σ and Σ' are any intermediate chains of collisions. So, if the contribution from $Y_{Xe\Sigma DD}$ is negligible, all chains of the type $Y_{Xe\Sigma\Sigma' DD}$ or $Y_{Xe\Sigma'\Sigma DD}$ will also have negligible contributions to the total fusion yield. Therefore, only a finite number of chains need to be computed in order to establish that the contributions from all other chains are negligible.

4.3 Calculation of the Fusion Yield of a Chain

To calculate the fusion yield for a given chain, one starts with the D–D fusion reaction at the end of the chain and works backwards through the chain to the incident ion. For example, for the chain Xe–Ti–Ti–D–D, the fusion yield $Y_{\mathrm{DD}}(E_{\mathrm{D}})$ for the chain segment D–D is calculated as a function of the initial energy of the penultimate deuteron, E_{D}, after being struck by the last Ti atom. Next, the fusion yield $Y_{\mathrm{TiDD}}(E_{\mathrm{Ti}})$ for the chain segment Ti–D–D is calculated as a function of the initial energy of the Ti atom. This process is continued until the yield for the entire chain, $Y_{\mathrm{XeTiTiDD}}(E_{\mathrm{Xe}})$, has been calculated.

Given a deuteron with energy E_{D} (in the laboratory frame) in a titanium deuteride sample, the fusion yield, $Y_{\mathrm{DD}}(E_{\mathrm{D}})$, is [5]

$$Y_{\mathrm{DD}}(E_{\mathrm{D}}) = \int_R^0 n_{\mathrm{D}}\sigma_f(E_{CM})dx = \frac{n_{\mathrm{D}}}{n_{\mathrm{D}}+n_{\mathrm{Ti}}}\int_0^{E_{\mathrm{D}}} \frac{dE}{\varepsilon_{\mathrm{D}}(E)}\sigma_f(E/2)\ , \qquad (4.3)$$

where x is the path length of the deuteron, R is its range, n_{D} and n_{Ti} are, respectively, the atomic densities of deuterons and titanium atoms in the target, ε_{D} is the sum of the nuclear and electronic stopping power of D in $\mathrm{TiD}_{1.7}$, and σ_f is the fusion cross section for the center of mass energy $E_{CM} = E_{lab}/2$ for the reaction D(d,p)T. (Note that $n_{\mathrm{D}}/(n_{\mathrm{D}}+n_{\mathrm{Ti}})$ is the atomic fraction of deuterons in $\mathrm{TiD}_{1.7}$, which can be labelled η_{D}). This integral is simply the integral of the number of deuterons the incident deuteron encounters times the fusion cross section for the energy at which the incident deuteron encounters each deuteron in its path. The first integral is in physical space, the second is in energy space. It is easier to work in terms of energy rather than depth because the fusion cross section is a function of energy and the natural limits of integration are from the initial energy E_{D} to the point where no further interactions occur (i.e., E=0).

Given a Ti atom with energy E_{Ti}, the fusion yield for the chain segment Ti–D–D is calculated by determining the energy distribution of energetic deuterons produced by Ti–D collisions, and summing the fusion yield for each of the energetic deuterons. The number of deuterons per unit energy with energy U created by the Ti atom before it comes to rest is given by

$$\nu_{\mathrm{D}}(U) = \eta_{\mathrm{D}}\int_0^{E_{\mathrm{Ti}}} \frac{d\sigma(E,U)}{dU}\frac{dE}{\varepsilon_{\mathrm{Ti}}(E)}\ , \qquad (4.4)$$

where η_{D} is the atomic fraction of deuterons in the target, $d\sigma(E,U)/dU$ is the differential scattering cross section for a Ti atom of energy E to transfer an energy

U to a deuteron and $\varepsilon_{\mathrm{Ti}}$ is the stopping cross section for Ti in $\mathrm{TiD}_{1.7}$. The fusion yield for this distribution of energetic deuterons created by the Ti atom of energy E_{Ti} is

$$\begin{aligned} Y_{\mathrm{TiDD}}(E_{\mathrm{Ti}}) &= \eta_{\mathrm{D}} \int_0^{U_{max}(E_{\mathrm{Ti}})} \nu_{\mathrm{D}}(U) Y_{\mathrm{DD}}(U) dU \\ &= \eta_{\mathrm{D}} \int_0^{E_{\mathrm{Ti}}} \frac{dE}{\varepsilon_{\mathrm{Ti}}(E)} \int_0^{\gamma_{\mathrm{Ti,D}} E} Y_{\mathrm{DD}}(U_{\mathrm{D}}) \frac{d\sigma(E, U_{\mathrm{D}})}{dU_{\mathrm{D}}} dU_{\mathrm{D}} \ , \end{aligned} \tag{4.5}$$

where $U_{max}(E_{\mathrm{Ti}}) = \gamma_{\mathrm{Ti,D}} E_{\mathrm{Ti}} = \big(4M_{\mathrm{Ti}} M_{\mathrm{D}} / (M_{\mathrm{Ti}} + M_{\mathrm{D}})\big) E_{\mathrm{Ti}}$ is the maximum energy transferrable from a Ti atom of energy E_{Ti} to a deuteron. The second equation is obtained by substituting Eq. 4.4 for $\nu_{\mathrm{D}}(U)$ and reversing the order of integration. The integral in Eq. 4.5 sums all possible Ti–D collisions during the slowing down of the Ti, weighted by the differential cross section.

Note that Y_{TiDD} is a function of the fusion yield of the next smaller chain segment, Y_{DD}. This is true for any size chain segment, and Eq. 4.5 can be generalized to the form

$$Y_{ab\ldots DD}(E) = \eta_b \int_0^{E} \frac{dE_a}{\varepsilon_a(E_a)} \int_0^{\gamma_{a,b} E_a} Y_{b\ldots DD}(U_b) \frac{d\sigma(E_a, U_b)}{dU_b} dU_b \ , \tag{4.6}$$

where a,b can be Ti, D, or the irradiating ion, η_b is the atomic fraction of atom b in the target, and $d\sigma/dU_{\mathrm{D}}$ is the differential scattering cross section for a–b collisions.

To continue the calculation of the fusion yield for the chain Xe–Ti–Ti–D–D, the yield for the chain segment Ti–Ti–D–D is calculated using Eq. 4.6 with a=Ti, b=Ti, $Y_{b\ldots DD}=Y_{\mathrm{TiDD}}$ and $Y_{ab\ldots DD}=Y_{\mathrm{TiTiDD}}$. Finally, the incident ion is added to the front of the chain, and the fusion yield for the entire chain, $Y_{\mathrm{XeTiTiDD}}(E_{\mathrm{Xe}})$, is found using Eq. 4.6 with a=Xe, b=Ti, and $Y_{b\ldots DD}=Y_{\mathrm{TiTiDD}}$. The fusion yields for all other chains are calculated in a similar manner.

4.4 Algorithms Used to Compute Fusion Yields

To calculate the values of the integrals in Eqs. 4.3 and 4.6, the following functions must be known: the fusion cross section for the D(d,p)T reaction as a function of the center-of-mass energy of the fusing deuterons ($\sigma_f(E_{CM})$); the differential scattering cross section for all possible a–b collisions as a function of incident energy, E_a, and energy transferred, U_b ($d\sigma(E_a,U_b)/dU_b$), where a,b=Ti, D, and Xe or Ar (the irradiating ion); and the stopping cross section in $\mathrm{TiD}_{1.7}$ as a function of energy ($\varepsilon_a(E)$) for all a.

The D(d,p)T fusion cross section is given by [6]

$$\sigma_f(E) = \frac{S(E)}{E} e^{-b/E^{1/2}} , \tag{4.7}$$

where E is the center of mass energy, b=31.39 keV$^{1/2}$, and $S(E)$ is a polynomial fit to the astrophysical S factor determined experimentally in [6]. The differential scattering cross section is of the Lindhard form [2]

$$\frac{d\sigma(E,U)}{dU} = \frac{\pi}{2} a^2 \lambda \frac{t^{-m}}{U} \left[1 + (2\lambda t^{1-m})^q\right]^{-1/q} , \qquad t = \frac{c_r^2}{\gamma} EU , \tag{4.8}$$

where a is the Firsov screening length [7], γ is the maximum fraction of energy transferable between the two atoms in the collision, c_r is the conversion factor from energy to the dimensionless "reduced" energy [2], and λ, m, and q are fitting parameters dependent on the type of interatomic potential assumed. The values of λ, m, and q for six commonly used potentials are given in Ref. 8. The nuclear and electronic stopping powers are calculated using the formulas in Ref. 7, except for the electronic stopping power of deuterons, which is calculated from a fit to experimental data [9].

Because of the complexity of the functional forms of the parameters above, an analytical solution to Eqs. 4.3 and 4.6 is not possible. Therefore, the integrals must be solved by numerical integration. This converts the integral to sums. Equation 4.3 then becomes

$$Y_{\mathrm{DD}}(E_{\mathrm{D}}) = Y_{\mathrm{DD}}(n\Delta E) = \eta_{\mathrm{D}} \sum_{i=0}^{n} \frac{\sigma_f(i\Delta E/2)}{\varepsilon_{\mathrm{D}}(i\Delta E)} \Delta E$$

$$= Y_{\mathrm{DD}}\big((n-1)\Delta E\big) + \eta_{\mathrm{D}} \frac{\sigma_f(n\Delta E/2)}{\varepsilon_{\mathrm{D}}(n\Delta E)} \Delta E. \qquad (4.9)$$

Similarly, Eq. 4.6 becomes

$$Y_{ab\ldots DD}(E) = Y_{ab\ldots DD}(n\Delta E) = \eta_b \sum_{i=0}^{n} \left[\sum_{j=0}^{m_i} Y_{b\ldots DD}(j\Delta U) \frac{d\sigma(i\Delta E, j\Delta U)}{dU} \right] \frac{\Delta U \Delta E}{\varepsilon_a(i\Delta E)}$$

$$= Y_{ab\ldots DD}\big((n-1)\Delta E\big) +$$

$$\eta_b \left[\sum_{j=0}^{m_n} Y_{b\ldots DD}(j\Delta U) \frac{d\sigma(n\Delta E, j\Delta U)}{dU} \right] \frac{\Delta U \Delta E}{\varepsilon_a(n\Delta E)}, \qquad (4.10)$$

where $\Delta U = i\gamma_{a,b}\Delta E/m_i$, where m_i is an integer. This choice of ΔU is made to avoid roundoff error in the calculation. Similarly, ΔE is chosen so that $\Delta E = E/n$, where E is the initial energy and n is an integer. Typically, calculations were made using n=1000 ($\Delta E \leq$600 eV), and m_i varying so that $\Delta U \sim$500 eV.

To calculate the total fusion yield for a given ion (for example, Xe) with an incident energy E_{Xe}, one begins by calculating the fusion yield Y_{DD} as a function of energy for the chain segment D–D. Using Y_{DD}, one next calculates Y_{DDD}, Y_{TiDD}, and Y_{XeDD}, the first two being chain segments and the last one being a complete chain (since it includes the incident ion). Xe–D–D is the first-generation-recoil fusion chain, since the penultimate deuteron is a first-generation recoil.

Next, D, Ti, and Xe are added to the front of each of the two chain segments above, and the fusion yields for those chains are calculated, giving Y_{DDDD}, Y_{TiDDD}, Y_{XeDDD}, Y_{DTiDD}, Y_{TiTiDD}, and Y_{XeTiDD}. At this point, the fusion yields of the second-generation recoils (Y_{XeDDD} and Y_{XeTiDD}) have been calculated.

To calculate the fusion yields for the next higher generation, D, Ti, and Xe are added to the front of the chain segments of the current generation, and the fusion yields for those chains are calculated. In general, there are 2^{n-1} n^{th} generation fusion chains, and to calculate the fusion yields for the first n generations of recoils, one must calculate the fusion yields of $2^{n+1}-2$ chains and chain segments.

The FORTRAN program used to calculate the fusion yields of the first three generations of recoils is listed in Appendix 2. Fusion yields were calculated for both Ar and Xe irradiation of 600 keV using each of the six interatomic potentials given in Ref. 8 (Thomas-Fermi-Sommerfeld, Bohr, Lenz-Jensen, Lindhard [c^2=1.8], Lindhard [c^2=3], and Molière). This gives the fusion yields for Ar and Xe as a function of energy for all energies up to 600 keV. The fusion yield for each chain (segment) took approximately 7 minutes to calculate on the μVAX used. Therefore, the fusion yields of the first three generations of recoils could be computed in about 100 minutes.

4.5 Results and Comparison to Experiment

The theoretical calculations of the total fusion yield did not depend strongly on interatomic potential for either Ar or Xe irradiation. In both cases, the total yield at a given energy varies by less than a factor of two over all six potentials. It was not necessary to calculate past the third generation recoils for either Ar or Xe irradiation to obtain all significant contributions to the total fusion yield, although the fusion yields of the fourth generation recoils were calculated to determine how the fusion yields decreased with increasing generation.

For both Ar and Xe, the fusion yield increases with increasing energy, with the increase being fastest at low energies and slowing at higher energies. The fusion yields appear to have a behavior similar to that of the D–D fusion cross section. For an irradiation at a given energy, the fusion yield for Ar is about an order of magnitude greater than that for Xe. This is because Ar is able to transfer a larger fraction of its energy (18.3% maximum) to the deuteron than Xe can (5.95% maximum). This results in higher energy deuterons, which have significantly higher fusion cross sections.

4.5.1 Model Results for Xe Irradiation

The most significant contributions to the total fusion yield for Xe irradiation from 50 to 600 keV come from the Xe–D–D and Xe–Ti–D–D chains, which together account for approximately 99.8% of the total yield. The Xe–Ti–Ti–D–D chain is the next most significant, contributing approximately 0.2% of the total. All other chains combined give less than 0.005%. The magnitude of the fusion yields for each chain calculated (using the Thomas-Fermi-Sommerfeld interatomic potential) is shown in figure 4.1a. The relative contribution of each chain to the total fusion yield is shown in figure 4.1b. The fusion yields for all chains of up to third generation are shown, except for that of Xe–D–Ti–D–D, which was too small to be calculated even using double precision variables. The dotted line represents the highest fusion yield from a fourth generation recoil chain ($Y_{\mathrm{XeTiTiTiDD}}$).

It is interesting to note that for Xe energies of less than 115 keV the fusion yield of Xe–Ti–D–D is greater than that of Xe–D–D. Also, the yield of Xe–Ti–D–D–D is greater than that of Xe–D–D–D for energies less than 105 keV. These are two examples of the case where adding one intermediate collision in a chain *increases* the fusion yield. The addition of the Ti in the chain increases the fusion yield because its mass is between that of Xe and D, which means that more energy can be transferred from the Xe to the deuteron through the Ti than can be transferred

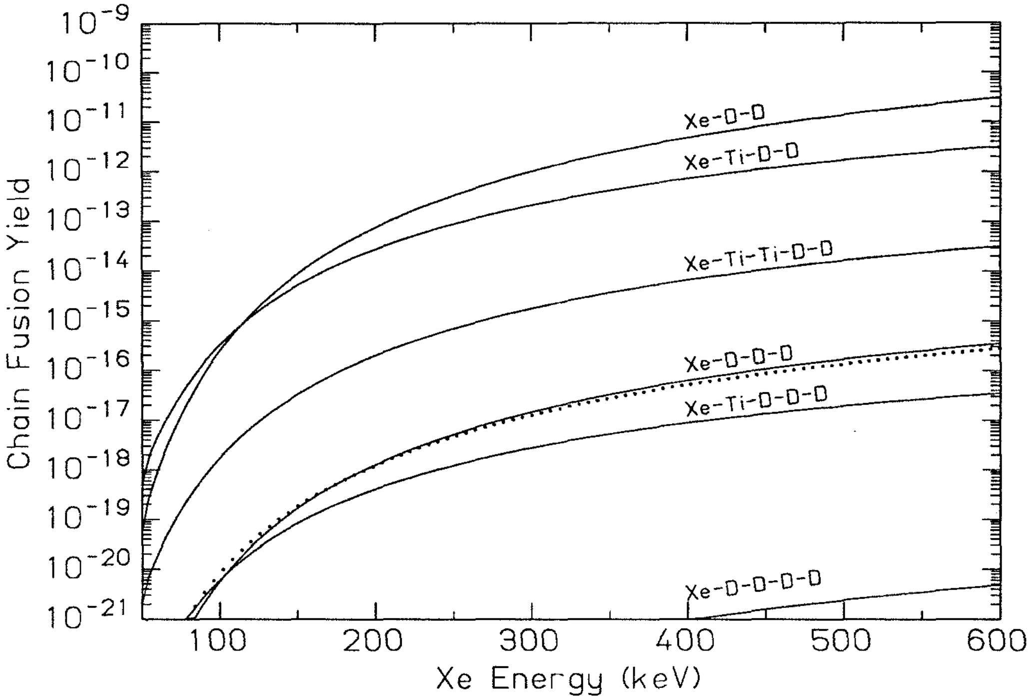

Figure 4.1a Theoretical fusion yields for the first three generations of recoils for Xe irradiation of $TiD_{1.7}$. The dotted line is the highest yield for 4^{th} generation recoils ($Y_{XeTiTiTiDD}$).

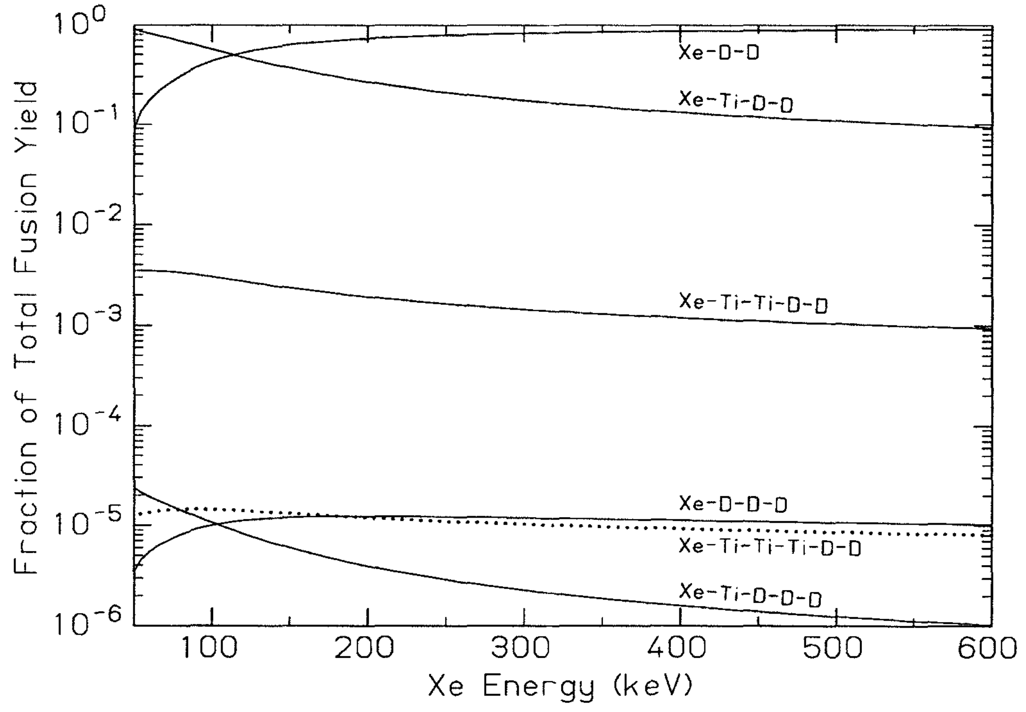

Figure 4.1b The relative contributions ($>10^{-6}$) to the total fusion yield for the chains shown in Fig 4.1a.

by a direct Xe–D collision (i.e., $\gamma_{\mathrm{Xe,Ti}} \times \gamma_{\mathrm{Ti,D}} > \gamma_{\mathrm{Xe,D}}$). Higher energy deuterons have larger fusion cross sections, and therefore, the fusion yield of the chain can be increased by adding the Ti. However, as the energy of the Xe increases, the probability of the high-energy-transfer Xe–Ti and Ti–D collisions becomes smaller and smaller until the increase in deuteron energy is offset by the decrease in the probability of creating an energetic deuteron. Above this energy, the normal order is returned (i.e., $Y_{\mathrm{XeDD}} > Y_{\mathrm{XeTiDD}}$).

In general, in order for the addition of an intermediate collision to increase the fusion yield of a chain, two conditions must be met. The first is that the mass of the intermediate atom be between that of the two atoms it collides with, so that there is an increase in the maximum energy transferred to the deuteron with the additional collision. The second is that the energy of the incident ion be low enough so that the increase in the fusion cross section due to the increase in deuteron energy is high enough to offset the decrease in the probability of creating an energetic deuteron. Since the fusion cross section increases most rapidly with increasing energy at low energies, the increase in fusion cross section due to the intermediate collision is most pronounced at low energies. Also, the decrease in probability of head-on (high energy transfer) collisions is least pronounced at low energies. Therefore, if the additional collision does increase the fusion yield, the increase will be most pronounced at low energies.

For the general case of irradiating material $M\mathrm{D}_x$ with ion I, it is possible to transfer the greatest fraction of the incident ion energy to the deuteron through M when the mass of M is the geometric mean of the masses of D and I, i.e., $m_M=(m_I \times m_{\mathrm{D}})^{1/2}$. For the case of Xe irradiation of $M\mathrm{D}_x$, the optimum mass of M for energy transfer is 16 amu (oxygen), with a 2.6 times increase in the energy transfer over that for direct Xe–D collisions (from 5.95% to 15.4%). For the case of Xe irradiation of Ti-deuteride, the maximum energy transferred by Xe–Ti–D is 2.0 times higher than that for Xe–D.

4.5.2 Model Results for Ar Irradiation

In the case of Ar irradiation, the total fusion yield is dominated by the Ar–D–D contribution. The Ar–Ti–D–D chain accounts for a little under 1% of the total yield, and all other chains combined contribute less than 0.01%. The magnitude of the fusion yields for each chain calculated (using the Thomas-Fermi-Sommerfeld interatomic potential) is shown in figure 4.2a. The relative contribution of each chain to the total fusion yield is shown in figure 4.2b. The fusion yields for all chains of up to third generation are shown, except for that of Ar–D–Ti–D–D, which has a fusion yield of $\sim$3 x 10^{-29} at 600 keV. The dotted line represents the highest fusion yield from a fourth generation recoil chain ($Y_{\mathrm{ArTiTiTiDD}}$).

Although the mass of Ti is greater than that of Ar, which indicates that it cannot increase the energy transferred from Ar to D, the chains involving Ti have higher fusion yields than those of the same generation that involve only Ar and D. This is because the mass of Ti is close to that of Ar and high-fraction energy transfers are much more likely for Ar–Ti and Ti–Ti collisions than they are for D–D collisions. For n^{th} generation chains, the highest fusion yield is from the chain Ar–$(\mathrm{Ti})_{(n-1)}$–D–D; the second highest from Ar–$(\mathrm{Ti})_{(n-2)}$–$(\mathrm{D})_{(2)}$–D, and so on. The chain with the lowest fusion yield for a given generation is that which alternates the most times between heavy and light atoms (i.e., Ar–D–Ti–D–Ti$\cdots$). This is because each Ti–D or D–Ti collision cannot involve an energy transfer of more than 16%.

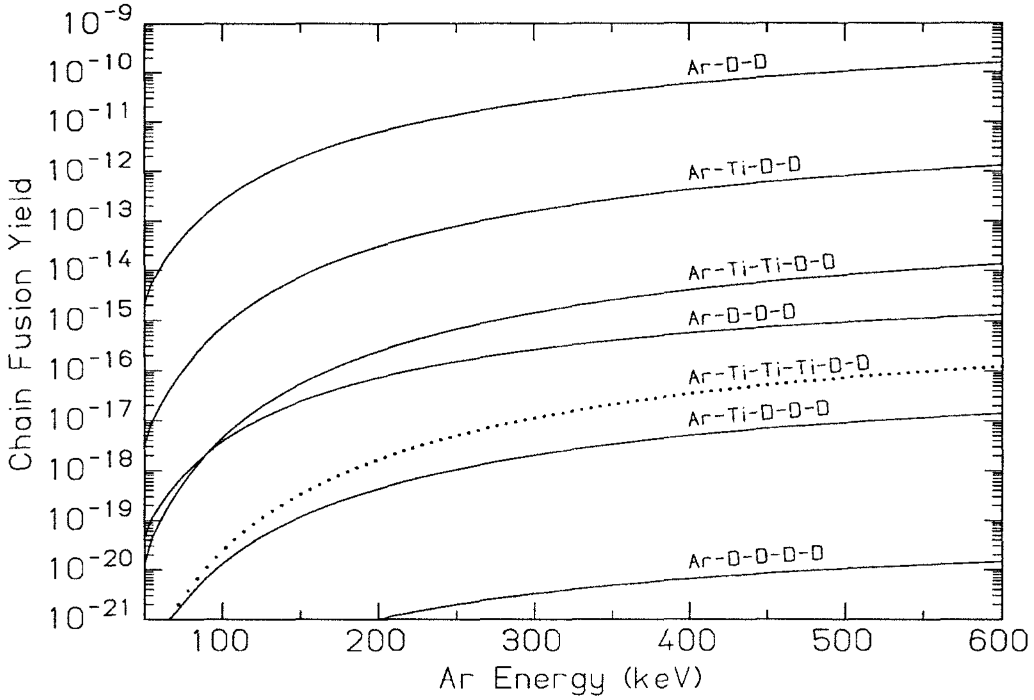

Figure 4.2a Theoretical fusion yields for the first three generations of recoils for Ar irradiation of $TiD_{1.7}$. The dotted line is the highest yield for 4^{th} generation recoils ($Y_{ArTiTiTiDD}$).

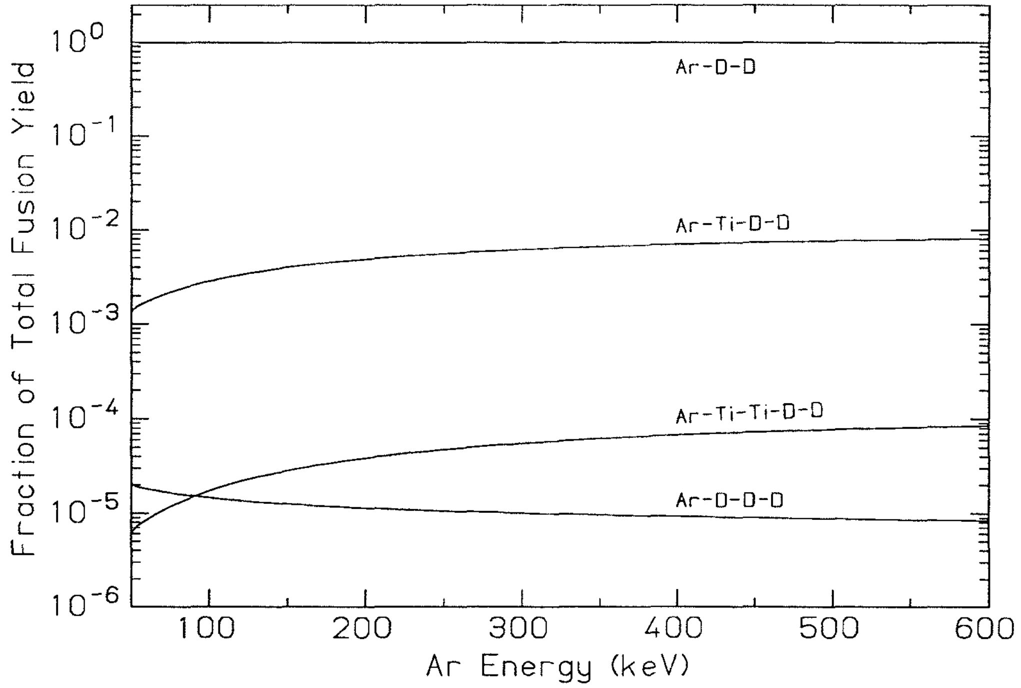

Figure 4.2b The relative contributions ($>10^{-6}$) to the total fusion yield for the chains shown in Fig 4.2a.

4.5.3 Comparison of Model with Experiment

The theoretical fusion yields are quite close to the experimental yields for both Ar and Xe irradiation. Theoretical fusion yields for four of the six potentials give an excellent fit to the experimental yields, one gives a marginally good fit, and the other is noticeably too high. The theoretical fusion yields for Ar irradiation of $TiD_{1.7}$ for all six interatomic potentials are compared with the experimental results for Ar in figure 4.3a. A similar comparison is made for Xe irradiation in figure 4.3b. The Lindhard $[c^2=3]$ potential gives the highest theoretical yield for both Ar and Xe, which can be seen to be somewhat higher than the experimental yields. All other potentials appear to be within the scatter of the experimental points. The reduced χ^2 for each potential compared to the experimental data is listed in Table 4.1. The χ^2 values for the two Lindhard potentials are noticeably larger than those for the other four potentials, which are nearly identical. For the final analysis, I chose the Thomas-Fermi-Sommerfeld (TFS) potential over the Lenz-Jensen (which had the same χ^2) because of its simpler form. Figure 4.4 compares the TFS theoretical fusion yields with the experimental yields for both Xe and Ar irradiation. The values are listed in Table 4.2.

The experimental fusion yields are in excellent agreement with those expected based on the linear binary collision cascade model. There is no need to consider additional processes (such as "cold fusion") to account for the experimental results. The collision cascade model shows that the fusion events occur mainly in the early stages of the collision cascade, with the dominant contribution coming from energetic deuterons created within the first three generations of collisions. Thus, the detection of D–D fusion products in this experiment is a direct observation of nuclear collisions occurring in the early stages of the collision cascade produced by heavy ion irradiation.

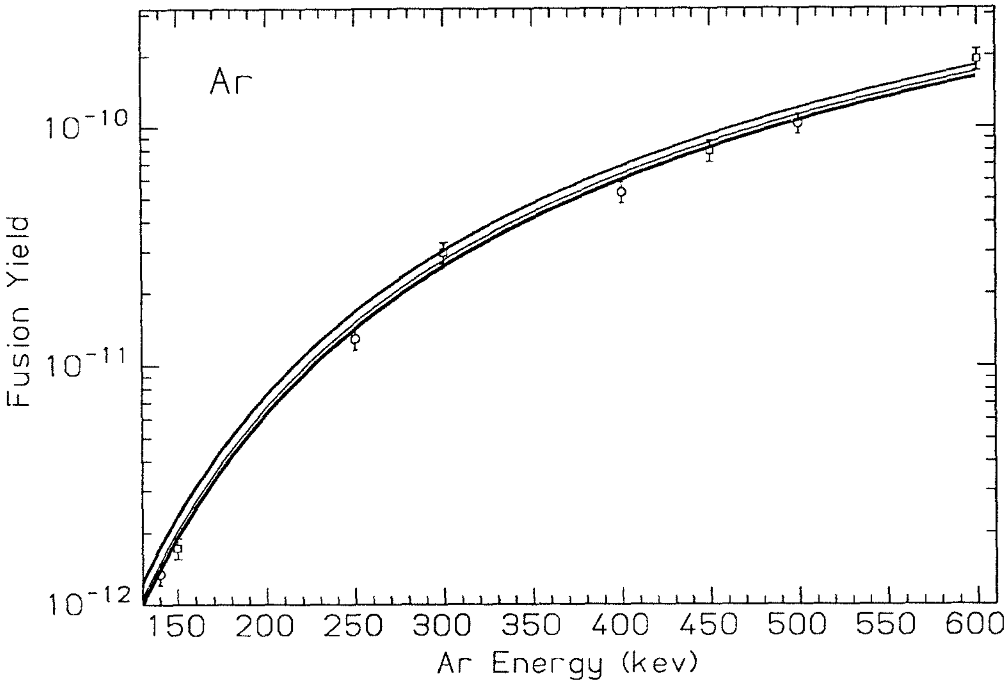

Figure 4.3a Comparison of theoretical fusion yields for six different interatomic potentials (lines) and experimental fusion yields (data points) for Ar irradiation of $TiD_{1.7}$.

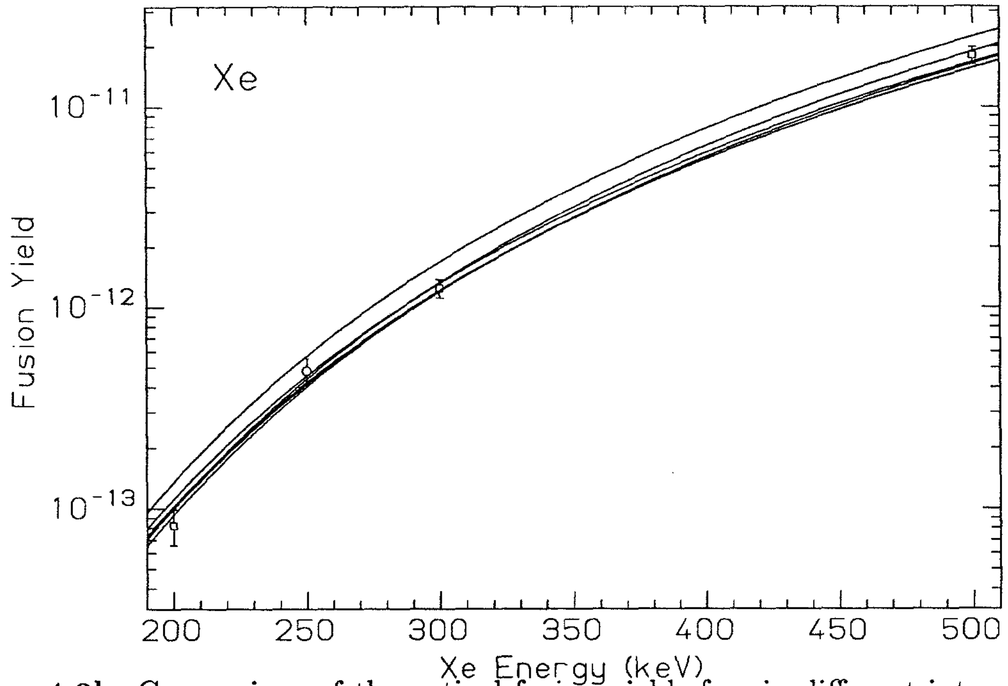

Figure 4.3b Comparison of theoretical fusion yields for six different interatomic potentials (lines) and experimental fusion yields (data points) for Xe irradiation of $TiD_{1.7}$.

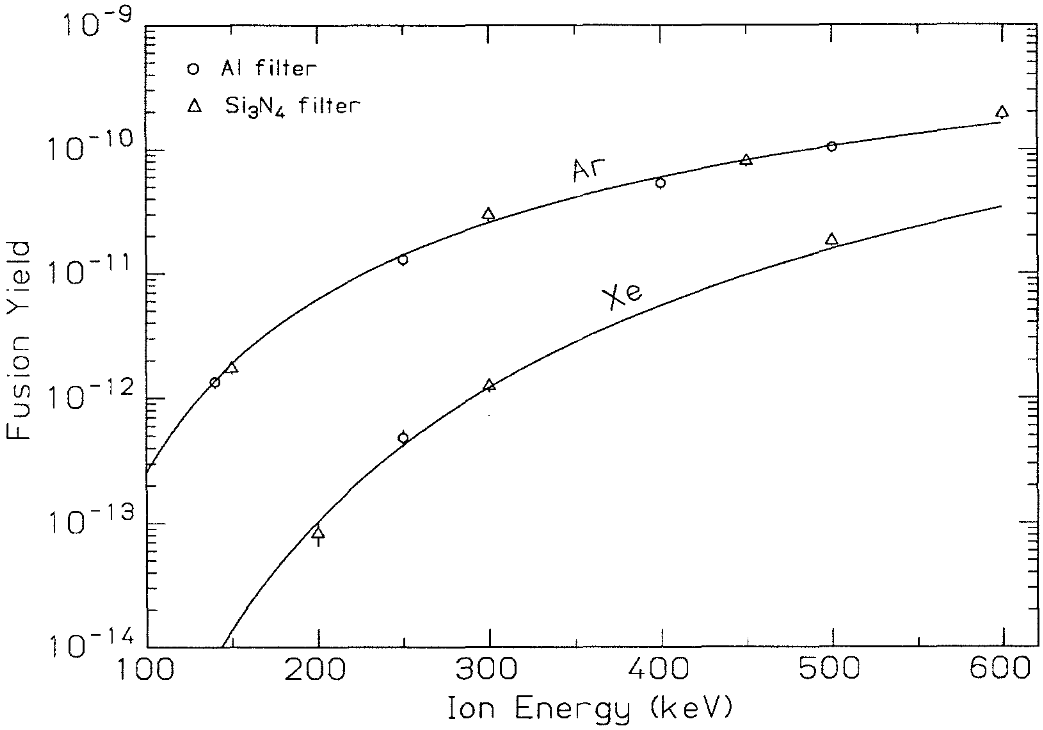

Figure 4.4 Comparison of theoretical (lines) and experimental (data points) fusion yields for Ar and Xe irradiation of $TiD_{1.7}$. Theoretical yields were calculated using the Thomas-Fermi-Sommerfeld interatomic potential, which gives the best fit to the experimental data.

Table 4.1 Reduced χ^2 values for theoretical fits to the experimental fusion cross sections using different interatomic potentials for Xe and Ar irradiation.

Potential	Reduced χ^2 Xe	 Ar	 Total
Thomas-Fermi-Sommerfeld	2.0	1.2	3.2
Lenz-Jensen	1.9	1.3	3.2
Molière	2.0	1.5	3.5
Bohr	1.3	2.4	3.7
Lindhard [c^2=1.8]	1.1	6.6	7.7
Lindhard [c^2=3.0]	7.9	15.4	23.3

Table 4.2 Experimental fusion yields and theoretical fusion yields calculated using the Thomas-Fermi-Sommerfeld interatomic potential for Ar and Xe irradiations of $TiD_{1.7}$.

Ion	Energy (keV)	Experimental Fusion Yield (fusion events/ion)	Theoretical Fusion Yield (fusion events/ion)
Xe	200	$(8.3 \pm 1.7) \times 10^{-14}$	1.03×10^{-13}
Xe	250	$(4.82 \pm 0.72) \times 10^{-13}$	4.22×10^{-13}
Xe	300	$(1.24 \pm 0.18) \times 10^{-12}$	1.21×10^{-12}
Xe	500	$(1.80 \pm 0.18) \times 10^{-11}$	1.56×10^{-11}
Ar	140	$(1.35 \pm 0.14) \times 10^{-12}$	1.38×10^{-12}
Ar	150	$(1.73 \pm 0.17) \times 10^{-12}$	1.88×10^{-12}
Ar	250	$(1.29 \pm 0.13) \times 10^{-11}$	1.40×10^{-11}
Ar	300	$(2.96 \pm 0.30) \times 10^{-11}$	2.56×10^{-11}
Ar	400	$(5.32 \pm 0.54) \times 10^{-11}$	5.95×10^{-11}
Ar	450	$(7.94 \pm 0.80) \times 10^{-11}$	8.12×10^{-11}
Ar	500	$(1.03 \pm 0.10) \times 10^{-10}$	1.06×10^{-10}
Ar	600	$(1.92 \pm 0.20) \times 10^{-10}$	1.61×10^{-10}

References

[1] J. F. Ziegler, J. P. Biersack, and U. Littmark, *The Stopping and Range of Ions in Solids*, Vol. 1 (Pergamon, New York, 1985).

[2] P. D. Townsend, J. C. Kelly, and N. E. W. Hartley, *Ion Implantation, Sputtering and their Applications* (Academic, London, 1976), pp. 19–21.

[3] J. P. Biersack and L G. Haggmark, Nucl. Instrum. Methods **174**, 257 (1980).

[4] J. P. Biersack and W. Eckstien, Appl. Phys. **A 34**, 73 (1984).

[5] C. Carraro, B. Q. Chen, S. Schramm, and S. E. Koonin, Phys. Rev. **A 42**, 1379 (1990).

[6] A. Krauss, H. W. Becker, H. P. Trautvetter, and C. Rolfs, Nucl. Phys. **A 465**, 150 (1987).

[7] J. P. Biersack, E. Ernst, A. Monge, and S. Roth, *Tables of Electronic and Nuclear Stopping Powers and Energy Straggling for Low Energy Ions* (Hahn -Meitner-Institut, Berlin, 1975), pp. 3–5.

[8] K. B. Winterbon, Rad. Effects **13**, 215 (1972).

[9] H. H. Anderson and J. F. Ziegler, *Hydrogen Stopping Powers and Ranges in All Elements* (Pergamon, New York, 1977).

Chapter 5

DOPPLER ANALYSIS OF PEAK SHAPES

During the irradiations utilizing the Si_3N_4 filter, it became apparent that the widths of the proton, triton, and helium signals varied with irradiating ion and energy; and that the energy of the peak positions shifted as well. As the same Si_3N_4 filter was used for all irradiations, and it was verified by backscattering analysis that after all irradiations were completed, the filter was virtually unchanged from its original state, the differences in the peak shapes must be due to differences in the collision cascades produced by the different irradiations.

The shape of the fusion product signals is a function of detector resolution, energy loss between the creation of the particle and its detection, and the distribution of Doppler shifts caused by the distribution of the deuteron–deuteron center-of-mass velocities relative to the detector. As the peak shapes are the result of a convolution of many processes (not all of which are precisely known), it would be difficult to analyze the Doppler shifts by manipulation of the experimental peaks. By modifying the binary collision cascade model discussed in Chapter 4, one can calculate the distribution of deuteron–deuteron center-of-mass velocities at the time of fusion and, by assuming an angular distribution of those velocities, compute theoretical peak shapes for the fusion products and compare with the experimentally obtained shapes. The analysis procedure is identical for protons, triton, and ^{3}He ions. As the proton signal is least effected by energy loss between creation and detection, analysis is focussed on the proton signal.

5.1 Processes Affecting Peak Shape

There are four factors that effect the detected energy of the fusion products. The first is the Doppler shift due to the motion of the center-of-mass (CM) frame of the colliding deuterons (from which the particles are emitted) relative to the lab frame (in which the particles are detected). This shift depends on the magnitude and direction of the velocity of the CM. The second is the energy loss of the particle while exiting the titanium deuteride film, which is a function of the depth at which the fusion event occurred. The third is the energy loss through the Si_3N_4 filter, which is a function of the angle (relative to the filter normal) at which the particle penetrates the filter. And the fourth is the detector resolution, which causes the detected energy of a mono-energetic beam of particles to have a Gaussian spread with a FWHM of 22 keV.

The energy loss of the fusion products on the outward path through the titanium deuteride is approximately 3.5 eV/Åfor 3.02 MeV protons, 15 eV/Åfor 1.01 MeV tritons, and 60 eV/Åfor ^{3}He ions [1]. The maximum depth at which fusion can occur is determined by the range of the incident ion. The largest range in this experiment is 3000 Å(for 600 keV ions) [2], which corresponds to an energy loss of 11, 45, and 180 keV for protons, tritons, and ^{3}He ions, respectively, produced at that depth. However, most fusion events occur in the high energy region of the collision cascade, which is significantly closer to the surface than the projected range of the ion, creating an energy loss distribution on the outward path peaked at zero and decreasing rapidly with depth. As the maximum energy loss for protons is 11 keV, the energy loss on the outward path can be ignored for protons.

From the detector–sample geometry, it is calculated that the distribution of incident angles for fusion products entering the detector through the filter is roughly Gaussian, with a mean value of 9° and a FWHM of 11°. Given this angular distribution, the energy loss distribution through the filter is calculated for each fusion product using a TRIM program similar to that of Ref. [3]. This energy loss distribution is convoluted with the detector resolution, giving the energy loss distribution detected for a mono-energetic beam of particles emitted from the sample surface (Table 5.1). The spectrum for these mono-energetic beams is compared with the experimental spectrum for 500 keV Xe^{++} irradiation in figure 5.1. The difference between the two spectra shows the effect of the Doppler shift and (for tritons and ^{3}He ions) the effect of energy loss for fusion events occurring at a depth in the sample.

Given energy distributions of fusion products exiting the sample surface, the detected energy distributions of these particles is found by convoluting those distributions with the detected energy loss distributions in Table 5.1.

Table 5.1 Energy loss distributions for mono-energetic beams of fusion products emitted from the surface.

Particle	Mean Energy Loss (keV)	Filter FWHM (keV)	Filter+Detector FWHM (keV)
proton	18	4.2	22.3
triton	75	10.0	24.1
^{3}He	306	21.6	30.7

5.2 Modeling the Deuteron Energy Spectrum

As discussed in Chapter 4, when an energetic ion I enters the titanium deuteride layer, it creates a series of collision cascade chains such as I–D and I–Ti–Ti, etc. Those chains resulting in fusion events must end in a D–D collision. For all cases

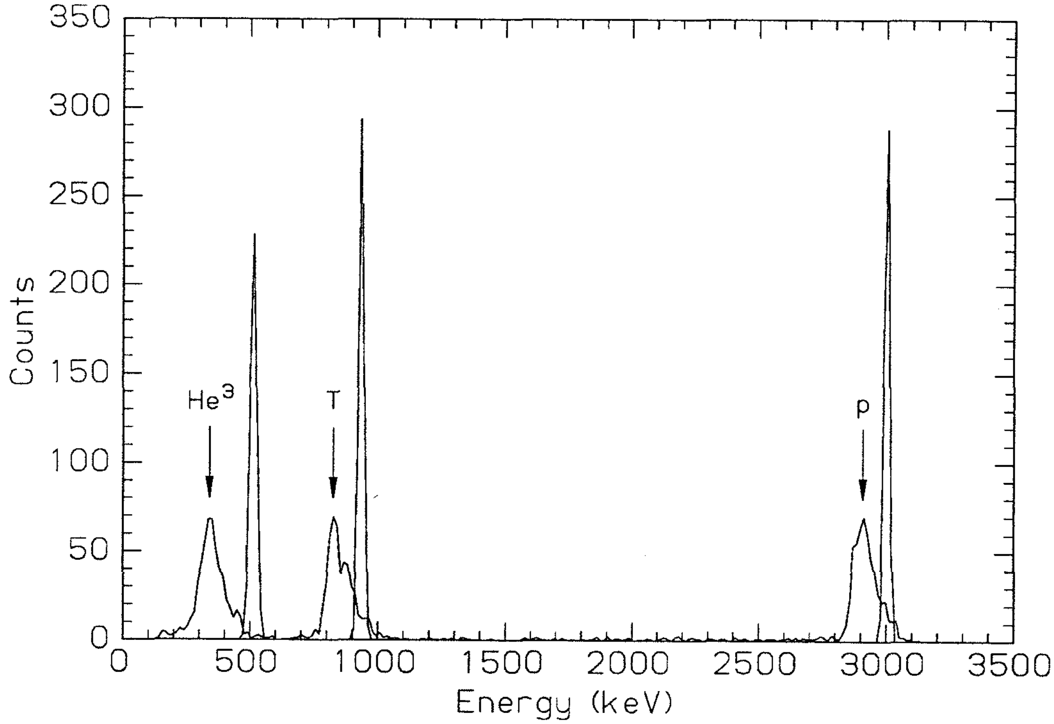

Figure 5.1 Comparison of theoretical and experimental fusion spectra for 500 keV Xe^{++} irradiation of $TiD_{1.7}$. Theoretical yields assume mono-energetic beams of 3.02 MeV protons, 1.01 MeV tritons, and 0.82 MeV ^3He ions emitted from the sample surface convoluted with the detected energy loss distribution of Table 5.1. The area under each theoretical signal is equal to the area under the corresponding experimental signal.

studied in this experiment, the fusion yield is adequately described by

$$Y_I = Y_{I\mathrm{DD}} + Y_{I\mathrm{TiDD}} + Y_{I\mathrm{TiTiDD}} \ . \tag{5.1}$$

In Chapter 4, these yields were calculated by starting with Y_{DD} and working backwards through the chain to the incident ion. In this method, an iterative equation for the fusion yield for an ion of energy E based on the yield for energy $E - \Delta E$ allows the simultaneous calculation of yields for all energies up to E. However, in calculating the yields in this way, the energy distributions of the atoms involved in the chain is not accessible.

In this section, the fusion yield will be calculated by starting with the incident ion and calculating the energy distribution of first generation D and Ti recoils, and then, given these distributions, calculating the energy distribution of second generation recoils, and so on. The fusion yield for a given chain is then calculated by computing the fusion yield for the energy distribution of the penultimate deuteron in the chain. (The final deuteron in the chain is at rest.) The fusion yield is calculated as a function of the incident deuteron energy at the moment of fusion. The total fusion yield for the incident ion is found by summing the fusion yields integrated over all deuteron energies for each chain. As an example, the fusion yield for Xe–Ti–Ti–D–D will be calculated.

Given an incident Xe ion with energy E_{Xe}, the energy distribution of titanium atoms produced by Xe–Ti collisions is given by

$$\nu_{\mathrm{XeTi}}(U) = \eta_{\mathrm{Ti}} \int_0^{E_{\mathrm{Xe}}} \frac{d\sigma(E,U)}{dU} \frac{dE}{\varepsilon_{\mathrm{Xe}}(E)} \ , \tag{5.2}$$

where $\nu_{\mathrm{XeTi}}(U)$ is the number of Ti atoms per unit energy with energy U, η_{Ti} is the atomic fraction of Ti in the target, $d\sigma(E,U)/dU$ is the differential scattering cross section for Xe–Ti collisions, and $\varepsilon_{\mathrm{Xe}}$ is the stopping cross section for Xe in $\mathrm{TiD}_{1.7}$.

Given the distribution $\nu_{\rm XeTi}$ of primary Ti recoils, the second generation of Ti recoils is found by using Eq. 5.2 multiplied by the number of Ti atoms per unit energy and integrated over all primary recoil Ti energies

$$\nu_{\rm XeTiTi}(U) = \eta_{\rm Ti} \int_0^{E_{\rm Ti,max}} dE_1 \int_0^{E_1} \nu_{\rm XeTi}(E_1) \frac{d\sigma(E,U)}{dU} \frac{dE}{\varepsilon_{\rm Ti}(E)} \,, \tag{5.3}$$

where $E_{\rm Ti,max}$ is $\gamma_{\rm XeTi} E_{\rm Xe}$. This formula can be generalized for calculation of n^{th} generation recoil distributions from $(n-1)^{th}$ distributions:

$$\nu_{{\rm Xe}\ldots ab}(U) = \eta_b \int_0^{E_{a,\rm max}} dE_1 \int_0^{E_1} \nu_{{\rm Xe}\ldots a}(E_1) \frac{d\sigma(E,U)}{dU} \frac{dE}{\varepsilon_a(E)} \,, \tag{5.4}$$

where a,b can be Ti or D, η_b is the atomic fraction of atom b, $d\sigma/dU$ differential scattering cross section for a–b collisions, and $E_{a,\rm max}$ is $\gamma_{\rm Xe\cdot} \cdots \gamma_{\cdot a} E_{\rm Xe}$. Given $\nu_{\rm XeTiTi}$, $\nu_{\rm XeTiTiD}$ is calculated using Eq. 5.4 with a=Ti, b=D, $\nu_{{\rm Xe}\ldots a}$=$\nu_{\rm XeTiTi}$, and $\nu_{{\rm Xe}\ldots ab}$=$\nu_{\rm XeTiTiD}$. At this point, the energy distribution of the penultimate deuteron of the chain has been calculated and can be used to determine the fusion yield of the chain. A similar procedure is used to calculate the energy distribution of the penultimate deuteron for all other chains.

The number of fusion events per unit energy occurring with a penultimate deuteron energy E_{fus} for the general chain $Xe \cdots D$ is a function of the number of these deuterons with energy E_{fus} or greater, because all these deuterons will lose energy and eventually have the possibility of causing a fusion event as they pass through the energy E_{fus}. Thus, the number of fusion events per unit energy at energy E_{fus} is given by

$$\nu_{{\rm Xe}\ldots{\rm D}fus}(E_{fus}) = \eta_{\rm D} \left(\int_{E_{fus}}^{E_{\rm D,max}} \nu_{{\rm Xe}\ldots{\rm D}}(E) dE \right) \frac{\sigma_f(E_{fus})}{\varepsilon_D(E_{fus})} \,. \tag{5.5}$$

The total fusion yield of the chain $Xe \cdots DD$ is found by integrating the number of fusion events per unit energy over all energies

$$Y_{{\rm Xe}\ldots{\rm DD}} = \int_0^{E_{\rm D,max}} \nu_{{\rm Xe}\ldots{\rm D}fus}(E) dE \,. \tag{5.6}$$

This equation gives exactly the same fusion yield as Eq. 4.6 for the same chain and incident ion energy because it is simply a rearrangement of the basic terms and a change in the order of integration from that of Eq. 4.6. The total fusion yields for each chain are summed (Eq. 5.1) to give the total fusion yield for the given incident ion and ion energy.

5.3 Model Results

To compute the energy distribution of deuterons at the moment of fusion and the total fusion yield, the integrals above must be solved by numerical integration, just as in Chapter 4. A similar conversion from integrals to summations was made, and simple rearrangements in the order of calculation were made to increase the efficiency of the computation. The same functions for stopping power, differential scattering cross section and fusion cross section as those used in Chapter 4, as well as the same energy increments were used to calculate the fusion yields here. Because of the large amount of memory needed to store the energy distributions of each atom in each chain of the collision cascade, the distributions can be calculated for only one ion energy at a time. Also, because no iterative equation, such as Eq. 4.10, exists for calculations in the forward direction, there is very little increase in calculation speed by combining calculations for different ion energies.

Calculations were made for 150, 300, 450, and 600 keV Ar and 200, 300, and 500 keV Xe, i.e., the experimental energies used with the Si_3N_4 filter. Because the Thomas-Fermi-Sommerfeld interatomic potential was shown (in Chapter 4) to give the best fit to experimental yields, it was the only potential used in these calculations. The fusion yields and energy distributions for the I–D–D, I–Ti–D–D, and I–Ti–Ti–D–D chains could be computed in less than 45 minutes on the μVAX.

The energy distribution for deuterons caused by 600 keV Ar^{++} irradiation is shown in figure 5.2a, and the distribution for 200 keV Xe^+ irradiation is shown in figure 5.2b. For the case of 600 keV Ar, the number of primary recoil deuterons is significantly higher than the number of deuterons in all higher generations for all deuteron energies. Thus, its contribution to the total fusion yield (99.2%) also dominates. For the case of 200 keV Xe, the number of primary recoil deuterons dominates at low energies. However, the maximum energy for primary recoil deuterons is 11.9 keV, while the maximum energy transferred to deuterons through the chain Xe–Ti–D is 24.3 keV (for 200 keV Xe). Above a deuteron energy of 11.9 keV, the number of deuterons from the Xe–Ti–D chain dominates.

The profiles of fusion yield as a function of deuteron energy at the time of fusion for all cases of Ar irradiation are shown in figure 5.3. The peak energy indicates the most probable deuteron energy at which fusion occurs, and is a compromise between high fusion cross section and high differential scattering cross section. These peaks are analogous to the Gamow peaks for fusion in solar interiors [4]. As the Ar energy is increased from 150 keV to 600 keV, the energy of the peak fusion yield increases slightly. However, for 150 keV Ar, the peak energy is 60% of the maximum deuteron energy, while for 600 keV Ar the peak energy is only 30% of the maximum deuteron energy. This indicates that as the ion energy is increased, the main contribution to the fusion yield comes from primary recoils in later and later stages of the cascade.

The profiles of fusion yield as a function of deuteron energy for all Xe irradiations are shown in figure 5.4a. An enlarged view of the fusion yield for 200 keV Xe irradiation is shown in figure 5.4b, with the contributions of the Xe–D–D and Xe–Ti–D–D chains shown with dashed lines. A small high energy tail can be seen for each of the peaks. This tail is due to the high-energy contribution of the Xe–Ti–D–D chain. The tail becomes increasingly predominant with decreasing Xe energies due to the increasing contribution of the Xe–Ti–D–D chain to the total fusion yield.

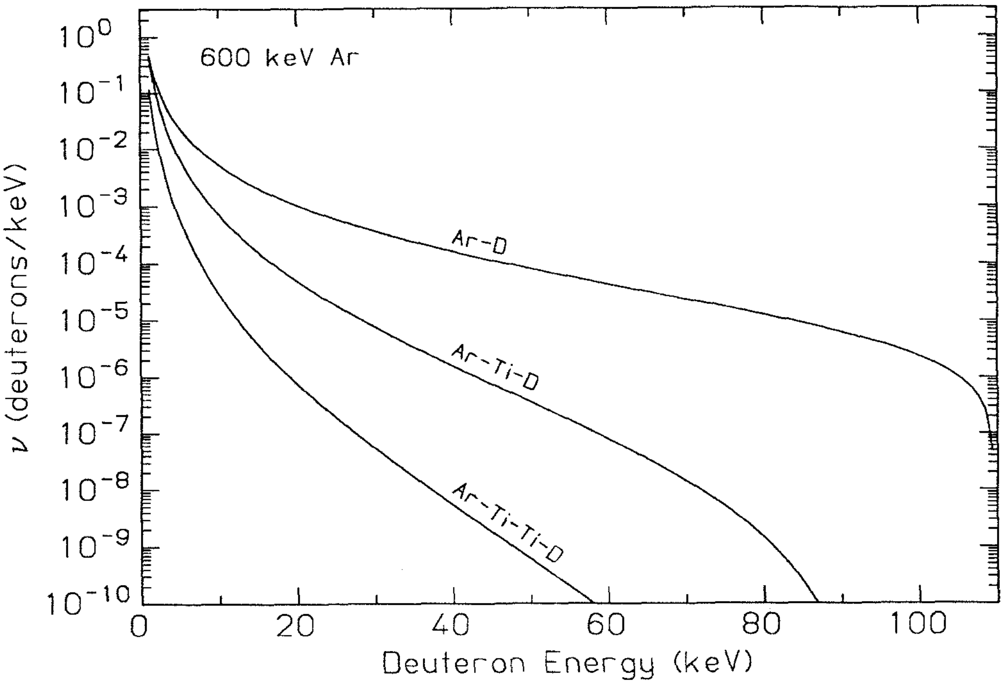

Figure 5.2a Theoretical deuteron energy distributions for 600 keV Ar^{++} irradiation for the three chains giving the largest contribution to the total fusion yield.

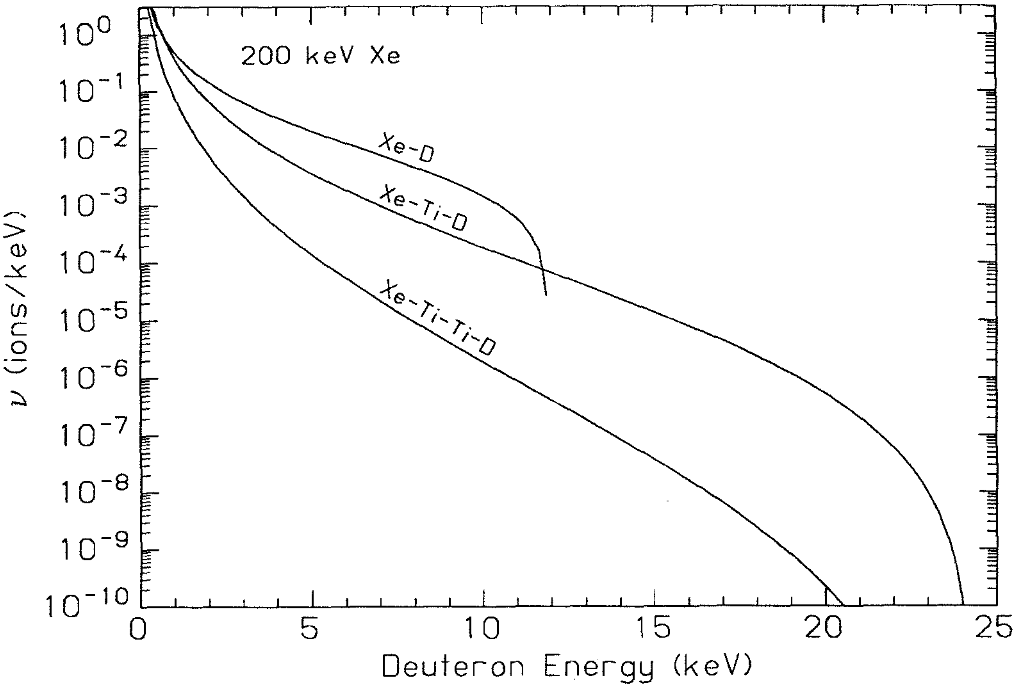

Figure 5.2b Theoretical deuteron energy distributions for 200 keV Xe^+ irradiation for the three chains giving the largest contribution to the total fusion yield. The maximum deuteron energy for the Xe–D chain is 11.9 keV.

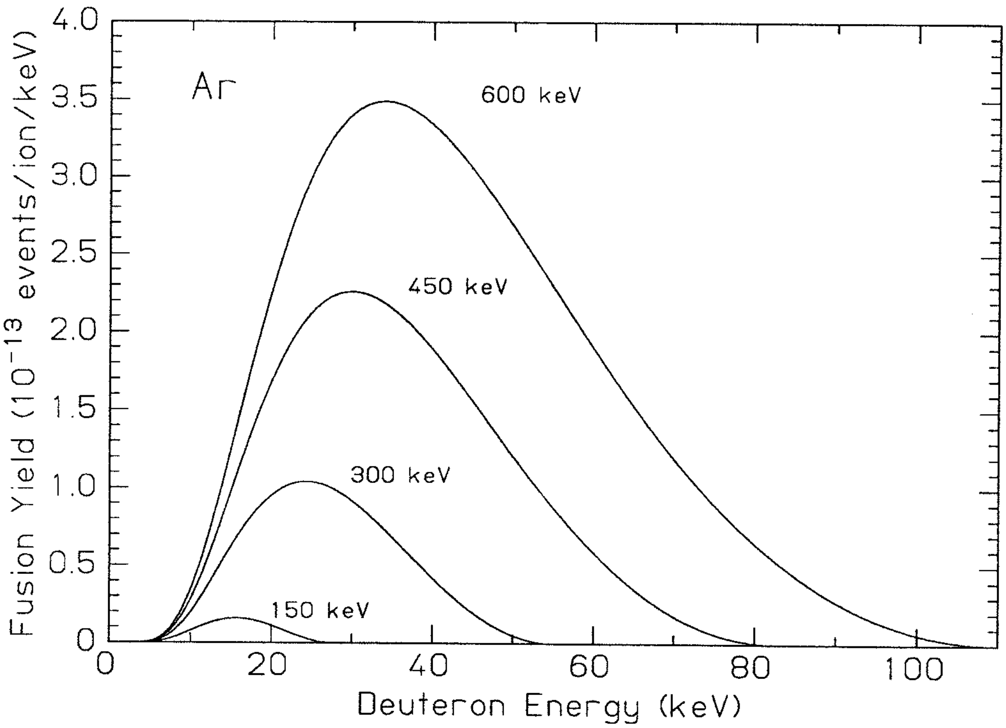

Figure 5.3 Theoretical fusion yield as a function of deuteron energy at the time of fusion for Ar irradiation at the energies used in the experiment. Each peak is dominated by the Ar–D–D chain contribution to greater than 99.2%.

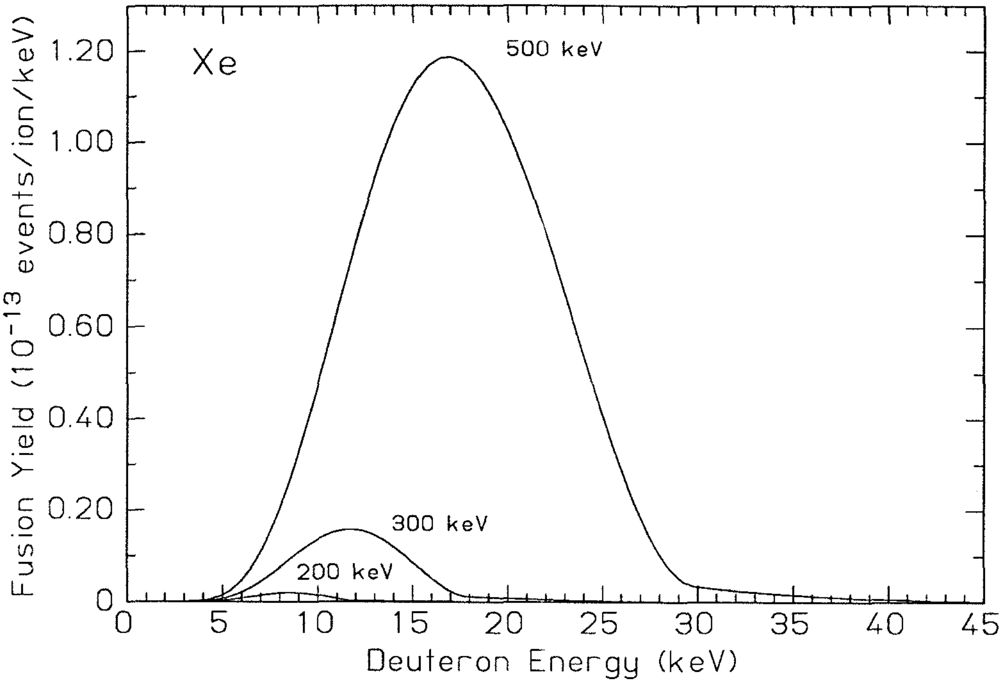

Figure 5.4a Theoretical fusion yield as a function of deuteron energy at the time of fusion for Xe irradiation at the energies used in the experiment. The high energy tails are due to the Xe–Ti–D–D chain contribution.

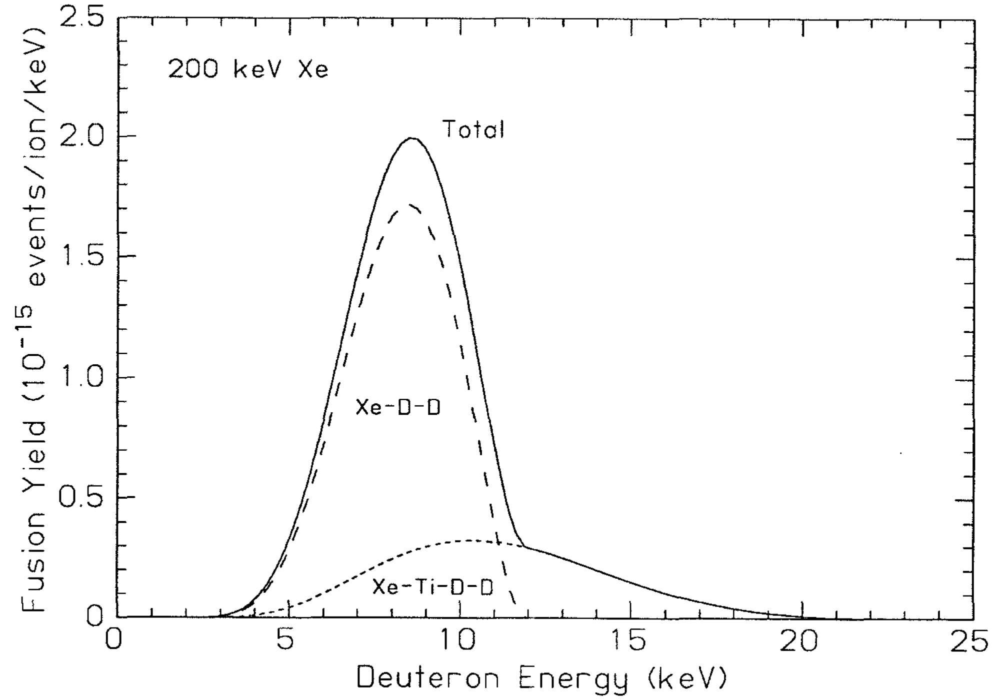

Figure 5.4b Enlarged view of the fusion yield for 200 keV Xe irradiation explicitly showing the contributions of the Xe–D–D and Xe–Ti–D–D chains.

5.4 Calculation of the Doppler Shift

The energy of the proton emitted in the D(d,p)T reaction is 3.02 MeV in the center-of-mass (CM) frame. The energy of the proton in the lab frame is Doppler shifted due to the velocity of the CM frame relative to the lab frame. To calculate the energy of the proton in the lab frame given its energy in the CM frame, the velocity of the CM frame and the angle between the CM velocity and the proton (CM) velocity must be known. Given an angle θ between the CM velocity and the proton CM velocity, the proton lab velocity is

$$\vec{v}_{p,lab} = \vec{v}_{p,cm} + \vec{v}_{cm} \tag{5.7}$$

$$\left|v_{p,lab}\right|^2 = \left(\left|v_{p,cm}\right| + \left|v_{cm}\right|\cos\theta\right)^2 + \left(\left|v_{cm}\right|\sin\theta\right)^2 \ , \tag{5.8}$$

where $\vec{v}_{p,lab}$ is the proton velocity in the lab frame, $\vec{v}_{p,cm}$ is the proton velocity in the CM frame, and $\vec{v}_{cm}$ is the velocity of the CM frame relative to the lab frame. For an ion of rest mass m_0 and kinetic energy E, the velocity v is

$$v = c\left[1 - \left(\frac{m_0c^2}{m_0c^2 + E}\right)^2\right]^{1/2} \quad \text{(relativistic).} \tag{5.9}$$

The relativistic formula is used to convert between energy and velocity because the relativistic correction (0.25% for 3 MeV protons) is greater than the energy width of a single channel of the MCA spectrum. Relativistic velocity addition for conversion to lab-frame velocity is not necessary since the maximum correction (~0.04%) is too small to affect the observed spectrum.

Given the distribution of deuteron energies (in the lab frame) immediately before fusion calculated in Section 5.3, the lab-frame velocity distribution is found using Eq. 5.9. Since the collision is between particles of equal mass, the CM velocity is 1/2 of the lab-frame velocity.

Since the Doppler shift is dependent on the angle between the proton velocity and the CM velocity, an angular distribution of the CM velocities must be assumed.

This angular distribution lies somewhere between a unidirectional beam directly into the sample and total isotropy. An isotropic angular distribution would produce a distribution of Doppler shifts symmetric around zero, i.e., positive and negative shifts in velocity are equally likely. A unidirectional distribution would produce the narrowest distribution of proton velocities. From the experimental data, an isotropic angular distribution is inappropriate because the proton signal is not symmetric around 3.0 MeV (3.02 MeV minus the energy loss through the filter), and the unidirectional distribution produces a proton signal that is too sharply peaked compared to the experimental peaks. However, the experimental data appear to be closer to the unidirectional than the isotropic angular distribution.

Because an accurate accounting of angular distributions as well as energy distributions would square the amount of information needed to be stored for each atom of each chain, it was not possible to keep track of angular distributions in the model calculations. Determining the precise angular distribution of the D–D CM velocities requires quite complex convolutions of different angular distributions in three-dimensional space for each nuclear collision from the initial entry of the ion into the sample up to the fusion event. The number of possible collision series terminating with a given D energy is quite large, and all must be considered to achieve a precise angular distribution. Such an analysis will not be attempted here. Instead, an approximate angular distribution will be developed, which allows a rough analysis of the experimental data in terms of the deuteron energy at the time of fusion.

From a phenomenological viewpoint, the deuterons with the maximum energy transferrable from the incident ion will have a very narrow angular distribution because they are the result of head-on collisions, and therefore must be travelling in the same direction as the incident ions. The lower the deuteron energy, the more likely it has been involved in nuclear collisions resulting in angular deviations. Assuming a Gaussian distribution of angles centered around the incident ion direction (which is 130° from the detector direction), the weight of the contribution of a given angle θ is

$$w(\theta) = \frac{1}{\sqrt{2\pi}\ \sigma(T)} \exp\left[-\frac{(\theta - 130^\circ)^2}{2\sigma^2(T)}\right] , \tag{5.10}$$

where θ is in degrees, T is the deuteron energy at the time of fusion, and $\sigma(T)$ is the standard deviation of the angular spread for energy T.

The energy loss mechanisms resulting in a deuteron energy (T) at the time of fusion less than the maximum value (T_{max}) are nuclear and electronic energy loss of the incident ion and atoms preceding the deuteron in the chain ($\Delta T_{I,nuc}$,$\Delta T_{I,ele}$), a less-than-maximum energy transfer in the nuclear collision with the preceding atom (ΔT_{col}), and nuclear and electronic energy loss of the deuteron before fusion occurs ($\Delta T_{\mathrm{D},nuc}$,$\Delta T_{\mathrm{D},ele}$), i.e.,

$$T = T_{\mathrm{max}} - \Delta T_{I,nuc} - \Delta T_{I,ele} - \Delta T_{col} - \Delta T_{\mathrm{D},nuc} - \Delta T_{\mathrm{D},ele} \ . \tag{5.11}$$

Because the electronic energy losses do not result in angular deviation, only the nuclear stopping (collisions) terms are considered in calculating the angular distribution of deuterons with energy T. The nuclear energy loss of the deuteron accounts for less than 10% of its total energy loss for energies greater than 5 keV [3] (the lowest deuteron energy which has a significant contribution to the total fusion yield). Nuclear energy loss accounts for approximately 40% and 70% of the total energy loss for Ar and Xe ions, respectively for the range of energies in this experiment [3].

The relationship between energy transferred to the deuteron and scattering angle of the deuteron in the lab frame is [5]

$$T = \frac{4M_1M_2}{(M_1 + M_2)^2} E_1 \cos^2\theta \equiv T_{\mathrm{max}} \cos^2\theta \ , \tag{5.12}$$

where M_1 and M_2 are the masses of the incident and scattered particles, respectively, E_1 is the energy of the incident particle immediately before the collision, and θ is the angle between the direction of the incident particle before the collision and the direction of the scattered particle after the collision. The equation can be inverted to give the scattering angle as a function of the energy transfer

$$\theta = \cos^{-1}\left[\left(\frac{T}{T_{\max}}\right)^{1/2}\right] \equiv \cos^{-1}\left[\left(\frac{T_{\max} - \Delta T}{T_{\max}}\right)^{1/2}\right] , \tag{5.13}$$

where $\Delta T = T_{\max} - T$ is the difference in energy between the maximum energy transfer and the actual energy transfer.

Since the relative contributions of the different energy loss terms of Eq. 5.11 are unknown, a reasonable first-order approach is to combine all nuclear collision terms together to give a characteristic scattering angle. For this approach, the standard deviation $\sigma(T)$ of the angular distribution is

$$\sigma(T) = \cos^{-1}\left[\left(\frac{T_{\max} - \eta_{nvc}(T_{\max} - T)}{T_{\max}}\right)^{1/2}\right] , \tag{5.14}$$

where η_{nuc} is the fraction of the difference between $T_{\max}$ and T due to nuclear collisions. This functional form of $\sigma(T)$ is used with Eq. 5.10 to specify the angular distribution.

Using the deuteron energy distributions calculated in Section 5.3 and angular distributions determined by Eq. 5.10, the proton energy spectrum is calculated by setting up 1 keV wide bins for the proton energy, determining the bin into which a proton produced by a certain combination of CM energy and angle will fall, and adding the product of the angular weight and the energy weight to the bin. This procedure is followed for the entire spectrum of energies and angles. The resulting spectrum is then convoluted with the detected energy loss distribution of Section 5.1 to give the theoretical detected proton spectrum. For cases in which more than one collision chain gives a significant contribution to the fusion yield (such as for Xe irradiation), this transformation must be done separately for each chain because each chain will have its own set of angular distributions.

5.5 Comparison with Experiment

The transformation described above was performed for the theoretical deuteron distributions for 150, 300, 450, and 600 keV Ar and 200, 300, and 500 keV Xe irradiations, treating η_{nuc} as an adjustable fitting parameter. The best fits to the experimental data for 600 keV Ar and 200 keV Xe are shown in figures 5.5a and 5.5b, respectively, with the area under the theoretical curves normalized to match that of the experimental curves. The fits are compared to those assuming a unidirectional distribution directly into the sample, i.e., $\theta = 130°$.

For all Ar irradiations, the best fit to the experimental spectra is achieved using η_{nuc}=33. For all Xe irradiations η_{nuc}=40 gives the best fit. The larger η_{nuc} value for Xe irradiations is consistent with the fact that nuclear stopping gives a larger contribution to the energy loss of Xe than to that of Ar. Although fits to both Ar and Xe data are rather good, the fits to Xe data are poorer than those to Ar data, which is probably due to the more complicated collision chains involved in producing fusion for Xe irradiation.

Although the precise angular distribution of D–D CM velocities was not computed in the binary collision cascade model presented here, the calculated distribution of deuteron energies coupled with the simple-minded approximation of the angular distribution is sufficient to model the experimental proton signals accurately. Similar fits to the triton and ^{3}He signals can be made, but the fits are poorer due to the additional (unknown) energy distribution due to the energy loss of those particles upon exiting the titanium deuteride. If a more precise angular

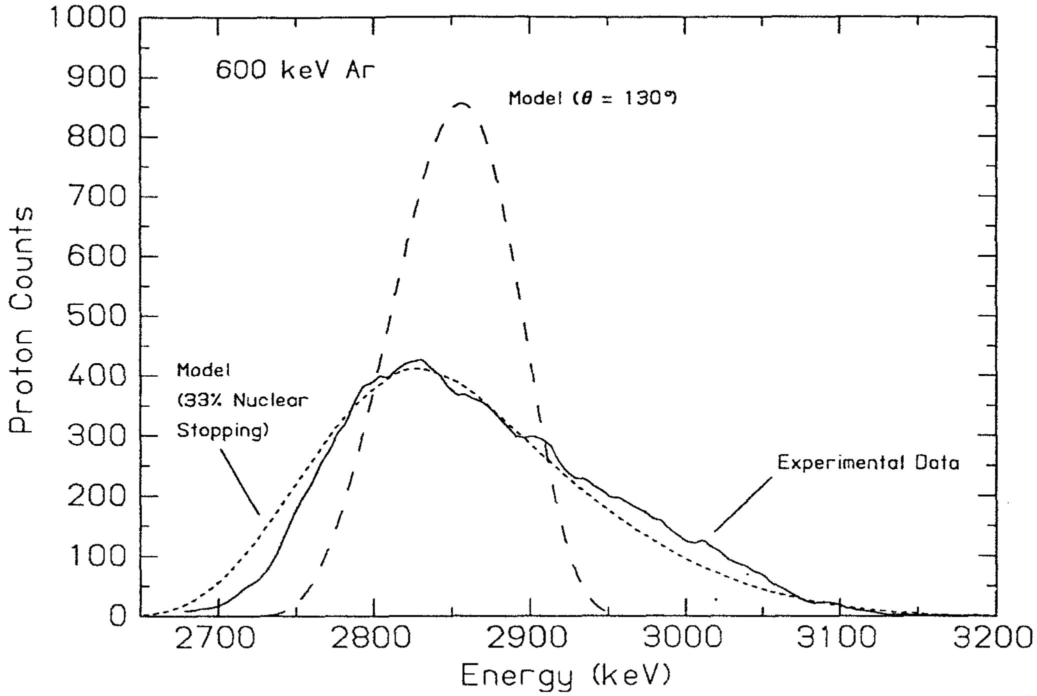

Figure 5.5a Comparison of unidirectional ($\theta = 130°$) and distributed angle (with 33% Nuclear Stopping) models and the experimental proton signal for 600 keV Ar^{++} irradiation.

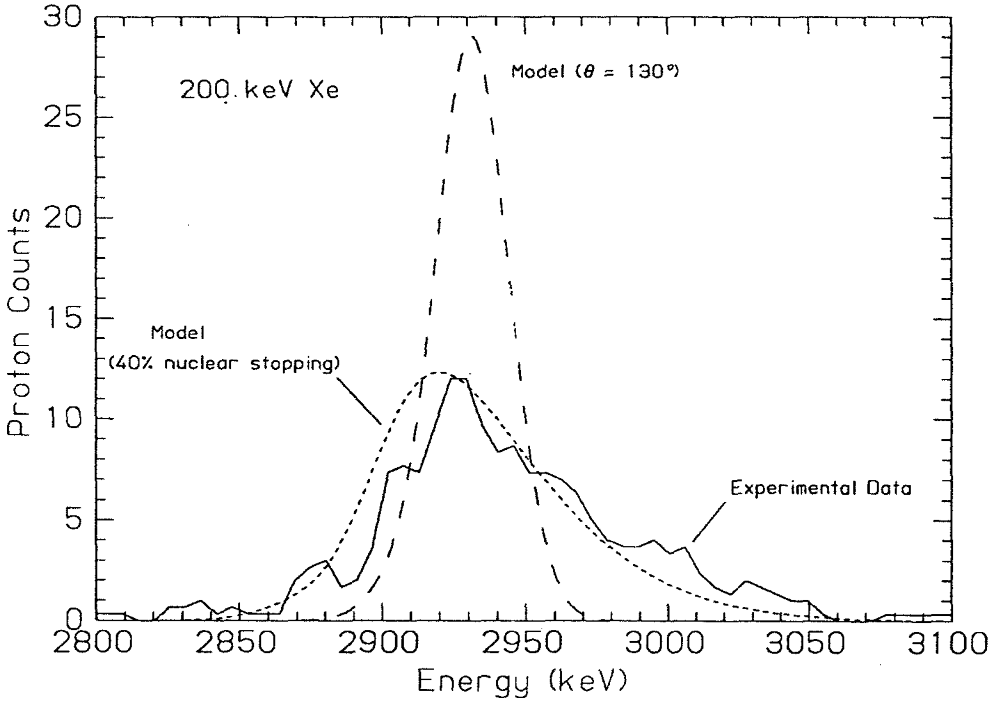

Figure 5.5b Comparison of unidirectional ($\theta = 130°$) and distributed angle (with 40% Nuclear Stopping) models and the experimental proton signal for 200 keV Xe^{+} irradiation.

distribution could be computed, it might be used to extract information about the depth distribution of fusion events from the ^{3}He signal, where the effects of depth distribution are most noticeable.

References

[1] H. H. Anderson and J. F. Ziegler, *Hydrogen Stopping Powers and Ranges in All Elements* (Pergamon, New York, 1977).

[2] J. F. Ziegler, J. P. Biersack, and U. Littmark, *The Stopping and Range of Ions in Solids*, Vol. 1 (Pergamon, New York, 1985).

[3] J. P. Biersack, and L. G. Haggmark, Nucl. Instrum. Methods **174**, 257 (1980).

[4] D. D. Clayton, *Principles of Stellar Evolution and Nucleosynthesis* (McGraw-Hill, New York, 1968), Ch. 4.

[5] J. B. Marion, *Classical Dynamics of Particles and Systems*, 2nd edition (Academic, New York, 1970).

Chapter 6

CONSIDERATIONS ON APPLICATIONS TO MATERIALS ANALYSIS

6.1 Comparison with Existing Techniques

As was shown in Chapter 4, the binary collision cascade model quite accurately (within ~10%) predicts the fusion yield for $TiD_{1.7}$ irradiated with Ar and Xe ions. Assuming the model accurately predicts fusion yields for arbitrary deuterium concentrations, one should be able to irradiate a film of unknown deuterium concentration and, using the experimentally obtained fusion yield, compute the deuterium concentration based on the predictions of the model presented here. Thus, irradiation of deuterium-containing materials with heavy ions could be used as a method of determining the average deuterium concentration in the region within approximately 100 nm of the sample surface. The first two questions that come to mind when considering the use of this technique for determining deuterium concentrations are (1) how can the technique be optimized in terms of accuracy, simplicity, and minimum detectable deuterium concentration, and (2) how would this optimum technique compare with currently used methods.

Currently used methods of hydrogen (and deuterium) profiling include Forward Recoil Elastic Scattering (FRES), Secondary Ion Mass Spectrometry (SIMS), and Nuclear Reaction Analysis (NRA) using beams of various ions in the MeV range [1,2,3].

Two FRES methods have been utilized. The first method involves irradiating the sample with a hydrogen beam and detecting the simultaneous emission of protons at ±45° from the incident beam direction [4]. This method has the drawback that samples must be self-supporting films thin enough to allow the clean transmission of the analyzing beam (generally a few MeV) through the sample. The second method involves glancing-angle incident beams of He and heavier ions with an energy of approximately 1 MeV/amu, and the detection of forward scattered hydrogen or deuterium [5,6]. In this method, mylar or aluminum filters ($\sim$10–100 μm thick) must be placed in front of the detector to remove forward scattered incident ions. Both techniques require the use of a standard to convert the spectrum to hydrogen concentration.

SIMS, which mass analyzes ions sputtered from the sample surface during low-energy (100 eV to 10 keV) ion bombardment, can generally detect hydrogen or deuterium down to concentrations of roughly 0.01 at%. However, accurate absolute concentrations cannot be determined, even with the use of standards, because of the severe effects of preferential sputtering, the effects of the matrix material on the charge state of the emitted particles, and residual hydrogen in the vacuum system, none of which can be accurately corrected for.

The third method, NRA, which detects backscattered particles with the characteristic energy of the nuclear reaction, can detect hydrogen or deuterium (depending on the nuclear reaction utilized) down to approximately 0.1 at% (again, depending on the reaction). Typical reactions used are ^{1}H(^{19}F,$\alpha\gamma$)^{16}O using 16–18 MeV ^{19}F ions [7], and ^{1}H(^{11}B,α)$\alpha\alpha$ using 2 MeV ^{11}B ions [8] for hydrogen, and D(^{3}He,p)^{4}He using 1.3 MeV ^{3}He beams [9]. NRA gives absolute measurements of the hydrogen or deuterium concentration without the need for standards. However, the sensitivity is limited by the fact that the signals are usually superimposed on a background signal.

The advantages of determining deuterium concentrations using the method of the present work, compared to the above methods, are (1) absolute concentrations are measured (no standard is necessary), (2) low energy ions (~500 keV) can be used, (3) insensitivity to hydrogen adsorbed during irradiation, and (4) there is virtually no background in the region of the proton signal used for the analysis. The disadvantages of using this method are (1) relatively low yields, (2) very little depth profiling capability, and (3) deuterium must be substituted for hydrogen.

6.2 Optimum Parameters for Measuring Deuterium Concentration

To optimize the utility of heavy-ion-induced fusion as a method of determining deuterium concentration, the optimum ion and ion energy must be determined. The goals to be considered, in order of importance, are (1) maximizing the fusion yield, (2) minimizing the error created by dilution of the deuterium concentration by addition of the irradiating species, and (3) minimizing the effect of the matrix on the fusion yield. Fortunately, the three goals are not in conflict with each other.

From Fig. 4.4, it is clear that increasing the ion energy increases the fusion yield, with a levelling off at the highest energies (due to the increase in the fraction of energy lost to electronic stopping and the levelling off of the increase in the fusion cross section). Also, the fusion yield for Ar is greater than that for Xe (due to increased energy transfer to the deuteron). Theoretical fusion yields were calculated for He, O, Ne, and Si at energies up to 1 MeV (Fig. 6.1). For energies above 500 keV, Ar gives the highest yield. As the energy decreases, the highest yield is obtained for lower mass ions. At the highest energy available to our ion implanter (600 keV), Ar, Si, or Ne beams will give roughly equivalent fusion yields. In that beams of inert gasses are easiest to obtain and have the largest currents on our implanter, Ar or Ne would be preferable.

To minimize the dilution effect of the incident beam, a lighter ion is preferable

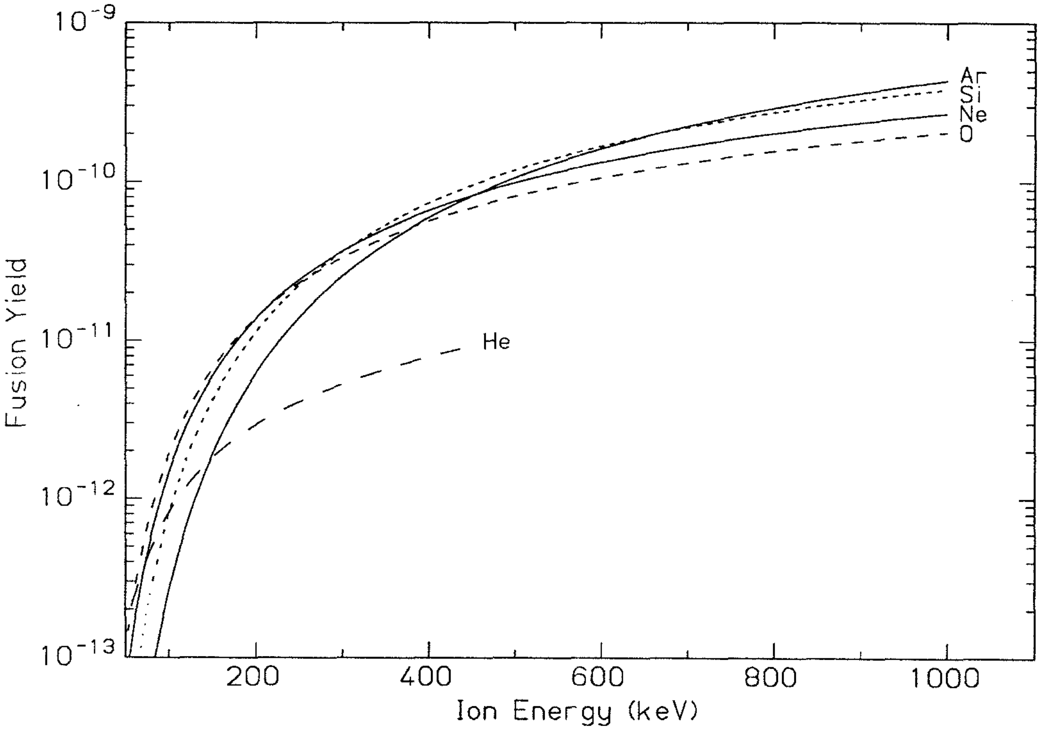

Figure 6.1 Comparison of theoretical fusion yields for irradiation of $TiD_{1.7}$ with various ions.

over a heavier ion because it penetrates farther into the sample and has a smaller sputtering coefficient. Thus, a higher dose of the lighter ion will be necessary to sputter away enough material to expose the implanted ion profile to the surface and dilute the deuterium in the region where a majority of the fusion events occur. Also, the peak concentration of the lighter ion will be smaller than that of the heavier ion due to increased range straggling. Therefore, if two ions of a particular energy give roughly the same fusion yield, the lighter of the two will have a smaller error due to the dilution effect. By the same arguments, a higher energy ion is preferable to a lower energy one.

Finally, the effect of the matrix element M containing the deuterium must be considered. The presence of the matrix has two effects on the fusion yield. The first is in its contribution to the stopping power of the incident ion I and energetic recoils, which is easily calculated. The second is in the fusion events occurring in chains in which it is involved, i.e., I–M–D–D, etc. To take into account the effect of these chains, the contribution to the total fusion yield for each chain must be calculated, which greatly increases the complexity of the calculations required. The ideal situation for ease of calculation of the fusion yield for a given irradiation is for the direct I–D–D chain to dominate. In this case, only the fusion yield for the I–D–D chain must be calculated. Therefore, to minimize the effect of the matrix and simplify the theoretical calculation of the fusion yield, an ion should be chosen that minimizes the transfer of energy to the deuteron via the I–M–D chain. For titanium deuteride samples, the fusion yield I–D–D dominates over all other chains for both Ar (~99.2%) and Ne (~99.8%) irradiation for energies up to 1 MeV. Therefore, the error involved in ignoring all other chains is negligible.

For titanium deuteride, considering fusion yields, dilution effect, simplicity of calculation, and available beam current on our implanter, Ne is the optimum ion for energies below 500 keV, and Ar is the optimum ion for energies above 500 keV. Figure 6.2 shows the theoretical fusion yields as a function of deuterium concentration in titanium deuteride for 1 MeV and 500 keV Ar and Ne irradiations. At 500 keV, the yields for Ar and Ne are nearly identical for all deuterium concentrations. In this case, Ne would be preferred due to its smaller dilution effect. At 1 MeV, the Ar fusion yield is larger than that of Ne by a large enough amount to make Ar irradiation preferable to Ne irradiation.

Since there is virtually no background in the region of the proton peak, the detection limit of heavy-ion-induced fusion analysis is determined by the fusion yield times the maximum dose of the irradiating ion that can be used without significantly affecting the stoichiometry of the sample in the region of analysis (or the maximum dose one is willing to use). Assume a 5 μA beam current for two hours ($\sim$2.5 x 10^{17} ions) to be the maximum dose. Assuming a precision of approximately 10% is desired, a minimum of 100 counts must be collected. For a detector solid angle of 50 mSr and isotropic angular distribution of emitted protons, 25000 fusion events must occur. This corresponds to a fusion yield of 10^{-13}. If this value is taken as the detection limit (for a 10% accuracy), the detection limit for 500 keV Ar or Ne is approximately 4 at% in titanium. For irradiations at 1 MeV, the detection limit is 3 at% for Ne and 2 at% for Ar. These values are somewhat higher than the range of those for the nuclear reaction analysis methods described above.

The model of the binary collision cascade has been shown to accurately predict the fusion yield for Ar and Xe irradiation of $TiD_{1.7}$. The above calculations show that the method of measuring deuterium content by D–D fusion induced by heavy-ion irradiation is expected to be on a par with other nuclear reaction analysis methods in its ability to measure the average deuterium concentration within the surface region of a titanium sample. Further research with this technique may lead

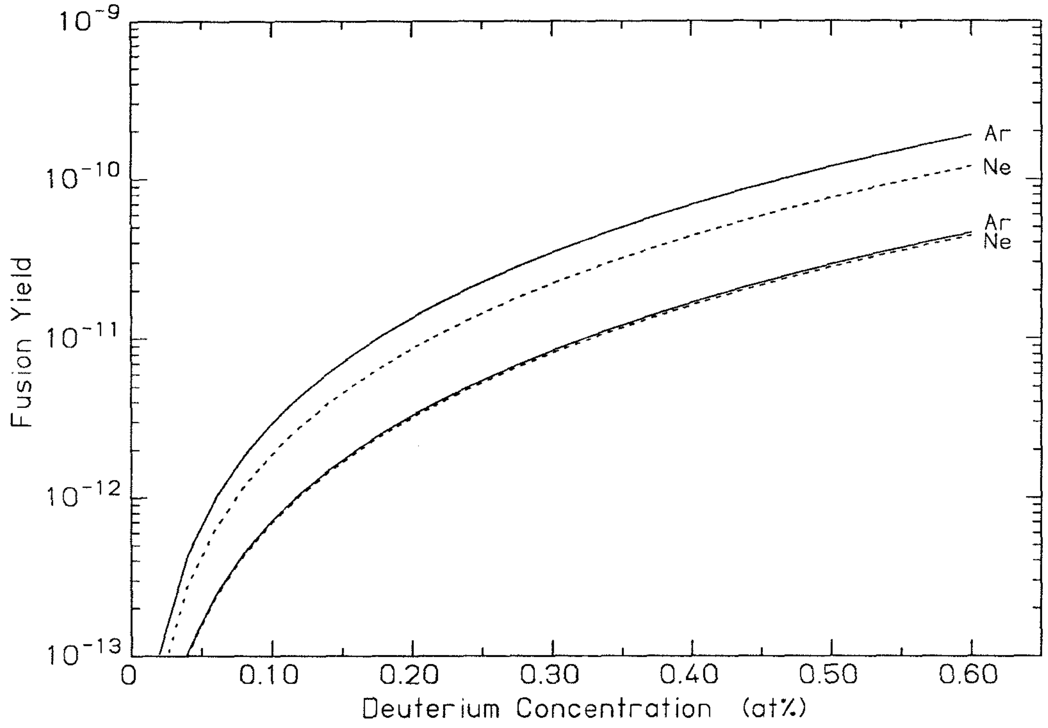

Figure 6.2 Theoretical fusion yields as a function of deuterium concentration for 1 MeV and 500 keV Ar and Ne ions. The detection limit for 500 keV ions is 4 at%, and for 1 MeV, it is 3 at% for Ne and 2 at% for Ar.

to the development of a method of analysis suitable for use on ion implanters with an energy range of a few hundred kV.

References

[1] J. F. Ziegler, C. P. Wu, P. Williams, C. W. White, B. Terreault, B. M. U. Scherzer, R. L. Schulte, E. J. Schneid, W. W. Magee, E. Ligeon, et al., Nucl. Instrum. Methods **149**, 19 (1978).

[2] P. D. Townsend, J. C. Kelly, and N. E. W. Hartley, *Ion Implantation, Sputtering and their Applications* (Academic, London, 1976).

[3] W. K. Chu, J. W. Mayer, and M-A. Nicolet, *Backscattering Spectrometry* (Academic Press, New York, 1978).

[4] B. L. Cohen, C. L. Fink, and J. D. Degnan, J. Appl. Phys. **43**, 19 (1972).

[5] T. T. Bardin, J. G. Pronko, and A. Joshi, Thin Solid Films **119**, 429 (1984).

[6] B. Terreault, J. G. Martel, R. G. St-Jacques, and J. L'Ecuyer, J Vac. Sci. Technol. **14**,492 (1977).

[7] D. A. Leich and T. A. Tombrello, Nucl. Instrum. Methods **108**, 67 (1973).

[8] E. Ligeon and A. Guivarc'h, Rad Eff. **22**, 101 (1974).

[9] P.P. Pronko and J. G. Pronko, Phys. Rev. **B 9**, 2870 (1974).

Appendix 1

FABRICATION OF THIN SI$_3$N$_4$ FILTERS

The purpose of the Si$_3$N$_4$ filter is to block sputtered particles and backscattered ions from reaching the detector, while allowing the fusion products to pass through with as little energy loss as possible. The most penetrating of the backscattered and sputtered particles created in this experiment are sputtered deuterons, which can have a maximum energy of ~100 keV (for 600 keV Ar^{++} irradiation). A Si$_3$N$_4$ layer 750 nm thick is required to full stop these particles.

The detector is a silicon surface-barrier detector with a diameter of 16.75 mm. The active area of the detector is a circle of 5.6 mm diameter (25 mm^2). The filter design is a 16.75 mm square of silicon (for easy alignment over the detector) with a 8 mm diameter circular window of Si$_3$N$_4$ in the center. The diameter of the window is large enough to avoid blocking the line of sight between any point on the sample and the active area of the detector.

The fabrication procedure began with a 4" $\langle 100 \rangle$ Si wafer coated on both sides with a layer of Si$_3$N$_4$ produced by low-pressure chemical vapor deposition (LPCVD). The thickness of the surface layer was determined by ellipsometry to be 940 nm. A mask was designed to fit 18 filters on the wafer, each separated from the others by a 100 μm scribe line for easy removal of the filters from the wafer (Fig. A1.1a). Photoresist was spun onto the back side of the wafer, and the mask placed over it so that the scribe lines were parallel to the $\langle 110 \rangle$ notch. The back side was then exposed to ultraviolet light. The black region of the mask prevented exposure of the photoresist, leaving it intact. The photoresist under the clear regions was exposed and removed, leaving bare Si$_3$N$_4$ (Fig. A1.1b). The exposed back-side Si$_3$N$_4$ was removed using a SF_6 RF plasma etch. After plasma etching, the photoresist layer was removed (Fig. A1.1c).

The exposed silicon was etched using an anisotropic silicon etch (EDP), which preferentially etches $\langle 100 \rangle$ Si. The etch is stopped by $\langle 111 \rangle$ planes. Therefore, the etch walls will not be vertical, but will slope inward at ~35°. Thus, the scribe lines do not etch all the way through the Si, but become groves. The diameter of the circles in the mask were made to be 8.65 mm to insure an 8 mm circle on the front side (Fig. A1.1d). The EDP etch was heated to 98°C and constantly stirred using a magnetic stirrer. The etch rate was ~50 μm/hour and took approximately ten hours to complete. After etching, the wafer was rinsed in de-ionized water and very carefully blown dry with flowing nitrogen. Finally, the individual filters were carefully separated. The finish filter is shown in figure A1.1e.

The Si_3N_4 layer was characterized using 2 MeV He^{++} backscattering spectrometry. The layer composition was determined to be $Si_3N_{3.32}$, and the areal density to be 5.25×10^{18} atoms/cm^2, which corresponds to roughly 540 nm of Si_3N_4 assuming a specific gravity of 3.44 g/cm^3.

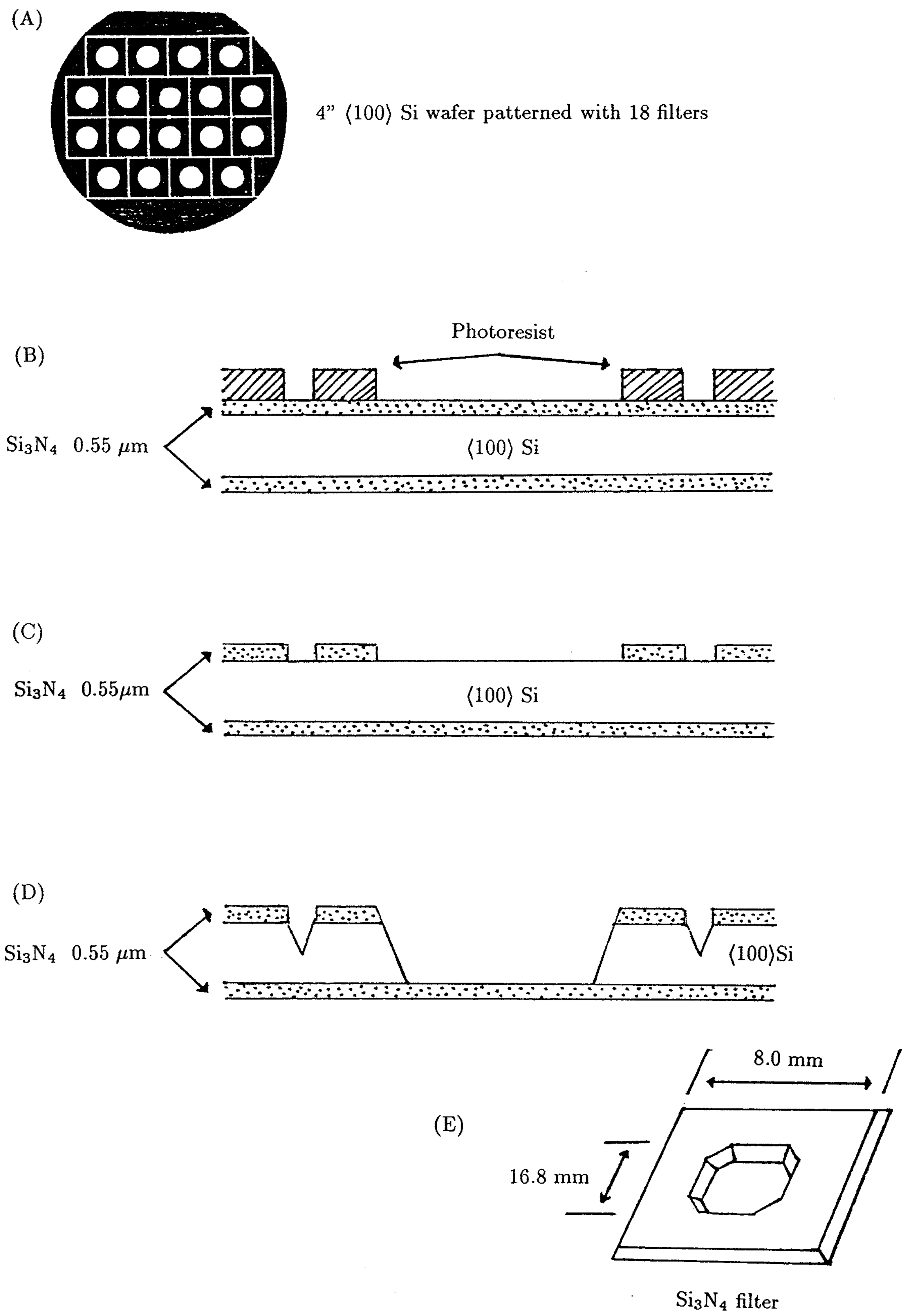

Figure A1.1 Procedure for fabricating thin Si_3N_4 filters.

Appendix 2

FORTRAN PROGRAM USED TO CALCULATE FUSION YIELDS

This FORTRAN program was used to calculate the theoretical fusion yields for Ar and Xe irradiation of titanium deuteride. It is based on the analysis and equations of Chapter 4. It is easily modified for use with other ions and/or other targets. Explanations of the necessary modifications are given in the program listing. It is set up so that the energy step ΔE is one thousandth of the incident beam energy; however, since the fusion yield as a function of energy is quite smooth, only every tenth of these thousand points are saved in the output file. The output file is a series of 100 triplets of energy, fusion yield, and uncertainty (which has been set to zero), as well as header information used by the plotting program NUFIT (a descendent of NAGFIT). The input parameters are ion (Ar or Xe), ion energy, interatomic potential (one of six choices), and deuterium concentration in the titanium deuteride film.

This version of the program is not designed for optimum speed, but to give maximum clarity of design. It is written in FORTRAN 4 and contains no machine specific functions, other than input, output, and file structure. This version runs about half as fast as the optimum version, which combines the calculation of several branches into a single step. Run time of this version on our μVAX is approximately 2.5 hours.

```
      program fusion
C
C     This algorithm calculates the  D(d,p)T fusion yield for heavy ion
C     irradiation of metal deuterides.   Any ion or metal matrix can be
C     used  (See note below).    Fusion yields  are calculated  for the
C     first 3 generations of recoils, plus one of the fourth generation.
C     The fusion  yield of  all chains  involving the  incident ion are
C     summed to give the total fusion yield for the ion.
C     ****************************************************************
C     *  Note:  To modify the incident ion simply modify Ma(3) and Z(3) *
C     *  To modify the metal matrix element modify Ma(1) and Z(1) and   *
C     *  modify the coefficients for the electronic stopping of deuter- *
C     *  ons in the function delestp(E).                                *
C     ****************************************************************
C
      real*8 Ma(3),Z(3),I0(3),pi,a0,e2,Me
      real*8 Ydd(2000),Yidd(2000),Yddd(2000),Ymdd(2000),
     +         Yiddd(2000),Yimdd(2000),Ydddd(2000),Ymddd(2000),
     +         Ydmdd(2000),Ymmdd(2000),Yidddd(2000),Yimddd(2000),
     +         Yidmdd(2000),Yimmdd(2000),Ymmmdd(2000),Yimmmdd(2000),
     +         Ytot(2000)
      real*8 E,E0,E_d_max,E_m_max,stp
      character fileout*30,file*22,labl*4
      real*8 conv_n1,conv_n2,conv_e1,conv_e2,conv_e3,conv_e4
      real*8 xd,a,gamma
      common /info1/ xd,a(3,2),conv_n1(3,2),conv_n2(3,2),conv_e1(3,2),
     +                 conv_e2(3),conv_e3(3,2),conv_e4(3,2),gamma(3,2)
      real*8 delE,atfrac
      integer ipot,loop
      common /info2/ delE(3),atfrac(3),ipot,loop
      real*8 lambda,m,q
      common /coef/ lambda(6),m(6),q(6)
C
C     *******       Setup of Parameters for dscs          ********
C     *******  (Differential Scattering Cross Section)   *******
C
      lambda(1) = 1.70    ! Thomas-Fermi-Sommerfeld
      m(1) = 0.311
      q(1) = 0.588
      lambda(2) = 2.37    ! Bohr
      m(2) = 0.103
      q(2) = 0.570
      lambda(3) = 2.92    ! Lenz-Jensen
      m(3) = 0.191
      q(3) = 0.512
      lambda(4) = 0.625   ! Lindhard  (c^2 = 1.8)
      m(4) = 1.0/3.0
      q(4) = 1.24
      lambda(5) = 0.879   ! Lindhard  (c^2 = 3)
      m(5) = 1.0/3.0
      q(5) = 1.24
      lambda(6) = 3.07    ! Moliere
      m(6) = 0.216
      q(6) = 0.530
C
C     **************  Input Initial Parameters  ***************
C
110   format(/,' Enter [1] for Ar  or  [2] for Xe irradiation: ',$)
120   format(' Enter the incident ion energy [keV]: ',$)
130   format(' Enter the Interatomic Potential Number: ',$)
140   format(' Enter the amount of Dueterium in the film TilDx: ',$)
      write(6,110)
```

```
      read(5,*) ion
      write(6,120)
      read(5,*) E0
      E0=E0*1000.00       ! Convert Energy to eV
      write(6,130)
      read(5,*) ipot
      write(6,140)
      read(5,*) xd
      call labels(labl,ilen2)
C
C     ************  Setup of the Common Variables  ************
C
C     **  constants  **
      loop=1000     ! The number of divisions in the distributions
      pi=3.1415926
      a0=0.529172   ! Bohr radius in Angstroms
      e2=14.3996    ! Electron charge squared in units of keV Angstroms
      Me=5.485802E-04     ! Electron mass in amu
C     **  target and ion properties  **
      atfrac(1)=1.0/(1.0+xd)          ! Metal atomic fraction
      atfrac(2)=xd/(1.0+xd)           ! Deuterium atomic fraction
      Z(1)=22.0                       ! Metal Matrix (Ti)  - Atomic Number
      Ma(1)=47.879              !                       Mass (amu)
      Z(2)=1.0                        ! Deuterium  -  Atomic Number
      Ma(2)=2.01594             !               Mass (amu)
      Z(3)=18.0                       ! Irrad. Ion (Ar) - Atomic Number
      Ma(3)=39.948              !                    Mass (amu)
      if (ion .eq. 2) Z(3)=54.0 ! Irrad. Ion (Xe) -  Atomic Number
      if (ion .eq. 2) Ma(3)=131.305   !                    Mass (amu)
      I0(1)=9.76+58.5/(Z(1)**1.19)    ! Formula for Z >= 13 Bethe-Bloch
      I0(2)=12.0+7.0/Z(2)       ! Formula for Z <  13 Bethe-Bloch
C     **  interaction parameters  **
      do 200 i=1,3
        conv_e2(i)=Ma(i)*Z(i)**(4.0/3.0)
        do 200 j=1,2
          a(i,j)=0.8853*a0/(Z(i)**0.50 + Z(j)**0.50)**(2.0/3.0)
          conv_n1(i,j)=a(i,j)/(Z(i)*Z(j)*e2*(1.0+Ma(i)/Ma(j)))
          conv_n2(i,j)=2.0*pi*a(i,j)*Z(i)*Z(j)*e2/(1.0+Ma(j)/Ma(i))
          conv_e1(i,j)=1.216091*Z(i)**(7.0/6.0)*Z(j)/
     +               ((Z(i)**(2.0/3.0)+Z(j)**(2.0/3.0))**1.5*Ma(i)**0.50)
          conv_e3(i,j)=4.0*Me/(Ma(i)*Z(j)*I0(j))
          conv_e4(i,j)=8.0*pi*e2**2.0*Z(i)**2.0/I0(j)
          gamma(i,j)=4.0*Ma(i)*Ma(j)/((Ma(i)+Ma(j))**2.0)
200   continue
C     **  characteristic energies  **
      E_m_max=E0*gamma(3,1)                       ! Max Metal energy (eV)
      E_d_max=max(E0*gamma(3,2),E_m_max*gamma(1,2))     !Max D energy(eV)
      delE(1)=E_m_max/float(loop)           ! Energy step for M ions (eV)
      delE(2)=E_d_max/float(loop)           ! Energy step for D ions (eV)
      delE(3)=E0/float(loop)                ! Energy step for I ions (eV)
C
C     **************  Calculation of D-D Yield  **************
C
C     Using iterative Eq. 4.9 of Thesis, where
C          stp = epsilon_D
C          atfrac(2) = eta_D
C
      stp = xnucstp(2,delE(2)) + delestp(delE(2))
      Ydd(1) = atfrac(2)*fcs(delE(2))*delE(2)/stp
      do 250 i=2,loop
        E=float(i)*delE(2)
        stp = xnucstp(2,E) + delestp(E)
```

```
        Ydd(i) = Ydd(i-1) + atfrac(2)*fcs(E)*delE(2)/stp
250   continue
C
C     ******  Calculation of Higher Generation Yields  ********
C
C     Call a subroutine which uses iterative Eq. 4.10 of thesis
C
C     **  First generation recoils  **
      call fuse(2,2,Ydd,Yddd)         ! D-D-D Yield
      call fuse(1,2,Ydd,Ymdd)         ! M-D-D Yield
      call fuse(3,2,Ydd,Yidd)         ! I-D-D Yield
C     **  Second generation recoils  **
      call fuse(2,2,Yddd,Ydddd) ! D-D-D-D Yield
      call fuse(1,2,Yddd,Ymddd) ! M-D-D-D Yield
      call fuse(3,2,Yddd,Yiddd) ! I-D-D-D Yield
      call fuse(2,1,Ymdd,Ydmdd) ! D-M-D-D Yield
      call fuse(1,1,Ymdd,Ymmdd) ! M-M-D-D Yield
      call fuse(3,1,Ymdd,Yimdd) ! I-M-D-D Yield
C     **  Third generation recoils  **
      call fuse(3,2,Ydddd,Yidddd)     ! I-D-D-D-D Yield
      call fuse(3,2,Ydmdd,Yidmdd)     ! I-D-M-D-D Yield
      call fuse(3,1,Ymddd,Yimddd)     ! I-M-D-D-D Yield
      call fuse(3,1,Ymmdd,Yimmdd)     ! I-M-M-D-D Yield
C     **  Fourth generation recoils  **
      call fuse(1,1,Ymmdd,Ymmmdd)     ! M-M-M-D-D Yield
      call fuse(3,1,Ymmmdd,Yimmmdd)   ! I-M-M-M-D-D Yield
C
C     *********  Calculation of Total Fusion Yield  ***********
C
      do 500, i=1,loop
        Ytot(i)= Yidd(i) +  Yiddd(i) + Yidddd(i) +  Yidmdd(i) +
     +             Yimdd(i) + Yimddd(i) + Yimmdd(i) + Yimmmdd(i)
500   continue
C
C     ********************  Store Results  *******************
C
      call titler('Idd',3,labl,ilen2,fileout)
      call stofus(fileout,3,Yidd,
     +               ' Ion-D-D Fusion Yield         ')
      call titler('Iddd',4,labl,ilen2,fileout)
      call stofus(fileout,3,Yiddd,
     +               ' Ion-D-D-D Fusion Yield       ')
      call titler('Idddd',5,labl,ilen2,fileout)
      call stofus(fileout,3,Yidddd,
     +               ' Ion-D-D-D-D Fusion Yield     ')
      call titler('Itidd',5,labl,ilen2,fileout)
      call stofus(fileout,3,Yimdd,
     +               ' Ion-Ti-D-D Fusion Yield      ')
      call titler('Ititidd',7,labl,ilen2,fileout)
      call stofus(fileout,3,Yimmdd,
     +               ' Ion-Ti-Ti-D-D Fusion Yield   ')
      call titler('Itititidd',9,labl,ilen2,fileout)
      call stofus(fileout,3,Yimmmdd,
     +               ' Ion-Ti-Ti-Ti-D-D Fusion Yield')
      call titler('Itiddd',6,labl,ilen2,fileout)
      call stofus(fileout,3,Yimddd,
     +               ' Ion-Ti-D-D-D Fusion Yield    ')
      call titler('Idtidd',6,labl,ilen2,fileout)
      call stofus(fileout,3,Yidmdd,
     +               ' Ion-D-Ti-D-D Fusion Yield    ')
      call titler('Ytot',4,labl,ilen2,fileout)
      call stofus(fileout,3,Ytot,
```

```
     +              ' Total Fusion Yield         ')
1000 continue
      end
C     *****************************************************************
      function xnucstp(ion,energy)
C     *  This gives the nuclear stopping power (epsilon_n) in units of  *
C     *  eV Angstrom^2/atom for ion (ion) of energy (energy) (eV) in a  *
C     *  target of M(1)D(xd). The formulae used are from J.P. Biersack, *
C     *  E. Ernst,  A. Monge,  and  S. Roth,  Tables of Electronic and  *
C     *  Nuclear Stopping Powers, and Energy Straggling for Low Energy  *
C     *  Ions (Han-Meitner, Berlin, 1975)p. 4                           *
C     *       epsi_m = reduced mass for collision with metal            *
C     *       epsi_d = reduced mass for collision with deuteron         *
C     *       Sn_m   = nuclear stopping in pure metal                   *
C     *       Sn_d   = nuclear stopping in pure deuterium               *
C     *****************************************************************
      real*8 epsi_m,epsi_d,Sn_m,Sn_d,energy,xnucstp
      real*8 conv_n1,conv_n2,conv_e1,conv_e2,conv_e3,conv_e4
      real*8 xd,a,gamma
      common /info1/ xd,a(3,2),conv_n1(3,2),conv_n2(3,2),conv_e1(3,2),
     +                 conv_e2(3),conv_e3(3,2),conv_e4(3,2),gamma(3,2)
      epsi_m=conv_n1(ion,1)*energy
      Sn_m=conv_n2(ion,1)*log(epsi_m)/(epsi_m-(epsi_m)**(-0.50))
      epsi_d =conv_n1(ion,2)*energy
      Sn_d =conv_n2(ion,2)*log(epsi_d)/(epsi_d-(epsi_d)**(-0.50))
      xnucstp=(Sn_m + xd*Sn_d)/(1.0+xd)     ! Addition by Bragg's Rule
      return
      end
C     *****************************************************************
      function elestp(ion,energy)
C     *  This gives the electronic stopping power (epsilon_e) in units  *
C     *  of eV Angstroms^2/atom  for ion (ion) of energy (energy) (eV)  *
C     *  in a target of M(1)D(xd). The formulae are from the same ref.  *
C     *  as the nuclear stopping power.                                 *
C     *       Sl(i) = Lindhard-Scharff formula electronic stopping for  *
C     *               stopping in (i=1) metal  and (i=2) deuterium      *
C     *       Sb(i) = Bethe-Bloch formula electronic stopping for       *
C     *               stopping in (i=1) metal  and (i=2) deuterium      *
C     *       Se(i) = Interpolation between L-S and B-B stopping        *
C     *       conv_e2(ion,i) = energy below which electronic stopping   *
C     *                        is adequately described by Sl(i) alone   *
C     *       epsi_b = 'reduced' Bethe-Bloch energy                     *
C     *  See Eqs. 1.3, 1.4, and 1.5 of thesis                           *
C     *****************************************************************
      real*8 Sl(2),Sb(2),Se(2),epsi_b,energy,elestp
      real*8 conv_n1,conv_n2,conv_e1,conv_e2,conv_e3,conv_e4
      real*8 xd,a,gamma
      common /info1/ xd,a(3,2),conv_n1(3,2),conv_n2(3,2),conv_e1(3,2),
     +                 conv_e2(3),conv_e3(3,2),conv_e4(3,2),gamma(3,2)
      do 200 i=1,2
        Sl(i)=conv_e1(ion,i)*energy**0.50
        if (conv_e2(ion)*energy .gt. 10.0) go to 100
        Se(i)=Sl(i)
        go to 200
100     continue
        epsi_b=conv_e3(ion,i)*energy
        Sb(i)=conv_e4(ion,i)*log(epsi_b+1.0+5.0/epsi_b)/epsi_b
        Se(i)=1.0/(1.0/Sl(i)+1.0/Sb(i))
200   continue
      elestp=(Se(1) + xd*Se(2))/(1.0+xd)    ! Addition by Bragg's Rule
      return
      end
```

```
C     *****************************************************************
      function delestp(energy)
C     *  This gives the electronic stopping power (epsilon_e) in units  *
C     *  of eV Angstroms^2/atom  for deuterons of energy (energy) (eV)  *
C     *  in a target of  M(1)D(xd).   Coefficients obtained from H. H.  *
C     *  Anderson  and  J. F. Ziegler,   Hydrogen Stopping Powers  and  *
C     *  Ranges in All Elements (Pergamon, New York, 1977).  These are  *
C     *  best fits to experimental data.                                *
C     *****************************************************************
      real*8 Se_d,Sl_d,Sh_d,Se_ti,Sl_ti,Sh_ti,E,energy,delestp
      real*8 conv_n1,conv_n2,conv_e1,conv_e2,conv_e3,conv_e4
      reak*8 xd,a,gamma
      common /info1/ xd,a(3,2),conv_n1(3,2),conv_n2(3,2),conv_e1(3,2),
     +                conv_e2(3),conv_e3(3,2),conv_e4(3,2),gamma(3,2)
      E=energy/(2.01594*1000.0) ! E in units of keV/amu
      if (E .ge. 10.00) go to 200
      Se_d = 1.262*(E**0.50)
      Se_ti= 4.862*(E**0.50)                ! in Units of 1E-15 eV cm^2
      go to 300
200   continue
      Sl_d =1.45*(E**0.45)
      Sh_d =242.6*log(1.0+(1.2E+4/E)+(0.1159*E))/E
      Se_d =1.0/(1.0/Sl_d + 1.0/Sh_d)
      Sl_ti=5.496*(E**0.45)
      Sh_ti=5165.0*log(1.0+(568.5/E)+(9.474E-3*E))/E
      Se_ti=1.0/(1.0/Sl_ti + 1.0/Sh_ti)     ! in Units of 1E-15 eV cm^2
300   continue
      delestp=10.0*(Se_ti + xd*Se_d)/(1.0+xd)! in Units of eV A^2/atom
      return
      end
C     *****************************************************************
      function dscs(ion,E,itarg,U,i)
C     *  This gives the  differential scattering cross section in units *
C     *  of  Angstrom^2/eV  for an incident ion (ion)  of energy E (eV) *
C     *  to collide  with an atom  itarg  and  give it  energy U (eV).  *
C     *  Formula is from P.D. Townsend, J.C. Kelly, and N.E.W. Hartley, *
C     *  Ion Implantation, Sputtering and Their Applications (Academic, *
C     *  London, 1976) pp 19-21.  The fitting parameters lambda,m,q are *
C     *  obtained from K.B. Winterbon, Rad. Eff. 13 (1972) 215.         *
C     *     Input Parameter i = number of interatomic pontential used   *
C     *     See Eq. 4.8 of thesis  [conv_n1(ion,itarg) = c_r]           *
C     *****************************************************************
      real*8 t,E,U,dscs
      real*8 lambda,m,q
      common /coef/ lambda(6),m(6),q(6)
      real*8 conv_n1,conv_n2,conv_e1,conv_e2,conv_e3,conv_e4
      real*8 xd,a,gamma
      common /info1/ xd,a(3,2),conv_n1(3,2),conv_n2(3,2),conv_e1(3,2),
     +                conv_e2(3),conv_e3(3,2),conv_e4(3,2),gamma(3,2)
      t=conv_n1(ion,itarg)**2.0*E*U/gamma(ion,itarg)
      dscs=(3.1415926/2.0)*a(ion,itarg)**2.0*lambda(i)*(t**(-m(i)))*
     +  ((1.0+(2.0*lambda(i)*t**(1.0-m(i)))**q(i))**(-1.0/q(i)))/U
      return
      end
C     *****************************************************************
      function fcs(E_lab)
C     *  This gives  the nuclear fusion cross section for  a  deuteron  *
C     *  with an energy  E_lab (eV)  in the laboratory frame of fusing  *
C     *  with a stationary deuterium atom in the target by the reation  *
C     *  D(d,p)T using the approximation  S(E)=S0 + S1*E + 0.5*S2*E^2.  *
C     *  Units of the cross section  are  Angstrom^2.  S(E) parameters  *
C     *  taken from  A. Krauss,  H.W. Becker, H.P. Trautvetter, and C.  *
```

```
C     *  Rolfs, Nuclear Physics A 465 (1987) 150.                         *
C     *       See Eq. 4.7 of thesis                                        *
C     ***********************************************************************
      real*8 b,S0,S1,S2,E_cm,E_lab,fcs
      b=31.39        ! units of keV^1/2
      S0=5.290E-07   ! units of keV Angstrom^2
      S1=1.900E-10   ! units of Angstrom^2
      S2=3.840E-11   ! units of Angstrom^2/keV
      E_cm=0.500*(E_lab/1000.0) ! E_cm in keV, E_lab in eV
      fcs=(S0+S1*E_cm+0.50*S2*E_cm**2.0)*exp(-b/E_cm**0.500)/E_cm
      return
      end
C     *********************************************************
C     *                    SUBROUTINE FUSE                    *
C     *********************************************************
C     Calculation of  fusion yield Yout  given fusion yield Yin
C     using iterative Eq. 4.10 of thesis, where:
C          Yin   = Yb...D
C          Yout  = Yab...D
C          stp   = epsilon_a
C          atfrac(itarg) = eta_b
C
      subroutine fuse(ion,itarg,Yin,Yout)
      real*8 Yin(2000),Yout(2000),delU,U,E,sum,stp
      real*8 conv_n1,conv_n2,conv_e1,conv_e2,conv_e3,conv_e4
      real*8 xd,a,gamma
      common /info1/ xd,a(3,2),conv_n1(3,2),conv_n2(3,2),conv_e1(3,2),
     +                  conv_e2(3),conv_e3(3,2),conv_e4(3,2),gamma(3,2)
      real*8 delE,atfrac
      integer ipot,loop
      common /info2/ delE(3),atfrac(3),ipot,loop
C
C     *************  Calculation of Yab...DD(1)  **************
C
      m = int(delE(ion)*gamma(ion,itarg)/delE(itarg))+1
      delU =  delE(ion)*gamma(ion,itarg)/float(m)
      sum = 0.00
      do 100 j=1,n
        U=float(j)*delU
        n1 = int(U/delE(itarg)+0.50)
        sum = sum + Yin(n1)*dscs(ion,delE(ion),itarg,U,ipot)
100   continue
      if (ion .ne. 2) stp=xnucstp(ion,delE(ion))+elestp(ion,delE(ion))
      if (ion .eq. 2) stp=xnucstp(ion,delE(ion))+delestp(delE(ion))
      Yout(1) = atfrac(itarg)*sum*delU*delE(ion)/stp
C
C     ********  Iterative Calculation of Yab...DD(i)  *********
C
      do 300 i=2,loop
        E = float(i)*delE(ion)
        m = int(E*gamma(ion,itarg)/delE(itarg))+1
        delU =  E*gamma(ion,itarg)/float(m)
        sum = 0.00
        do 200 j=1,m
          U=float(j)*delU
          n1=int(U/delE(itarg)+0.50)
          sum = sum +  Yin(n1)*dscs(ion,E,itarg,U,ipot)
200     continue
        if (ion .ne. 2) stp = xnucstp(ion,E) + elestp(ion,E)
        if (ion .eq. 2) stp = xnucstp(ion,E) + delestp(E)
        Yout(i) = Yout(i-1) + atfrac(itarg)*sum*delU*delE(ion)/stp
300   continue
```

```
      return
      end
C     ********************************************************
C     *                  SUBROUTINE LABELS                   *
C     ********************************************************
C     This  section  collects  and determines  the length  of a
C     label to be  appended to the file names  to differentiate
C     between different runs of the program.
C
      subroutine labels(labl,ilen)
      character xchar*4,labl*4
      write(6,10)
10    format(' Enter a label up to 4 characters long: ',$)
      read(5,20) xchar
20    format(A4)
      key=0
      do 100, i=1,4
        if (xchar(i:i) .eq. ' ' .and. key .eq. 1) go to 200
        if (xchar(i:i) .ne. ' ' .and. key .eq. 0) ibeg=i
        if (xchar(i:i) .ne. ' ') key=1
100   continue
      i=5
200   continue
      ilen=i-ibeg
      if (key .eq. 0) ilen=0
      labl(1:ilen)=xchar(ibeg:i-1)
      if (ilen .lt. 4) labl(ilen+1:4)='    '
      return
      end
C     ********************************************************
C     *                  SUBROUTINE TITLER                   *
C     ********************************************************
C     This section appends the identifying label and the exten-
C     tion '.fit' to each output file.
C
      subroutine titler(file,ilen1,labl,ilen2,fileout)
      character fileout*30,file*22,labl*4
      itot=ilen1+ilen2+4
      fileout(1:ilen1)=file(1:ilen1)
      fileout(ilen1+1:ilen1+ilen2)=labl(1:ilen2)
      fileout(ilen1+ilen2+1:itot)='.fit'
      if (itot .lt. 30) fileout(itot+1:30)='                         '
      return
      end
C     ********************************************************
C     *                  SUBROUTINE STOFUS                   *
C     ********************************************************
C     This section stores "thick target" fusion yield vs energy
C     in a form readable by NUFIT.  For convenience, the uncer-
C     tainty in the yield values is stored as zero. To conserve
C     space,  only every tenth value is stored.   As the yields
C     are  smooth  functions of energy,  no significant info is
C     lost.
C
      subroutine stofus(fileout,ion,Y,label)
      real*8 Y(2000),E
      character fileout*30,label*30
      real*8 delE,atfrac
      integer ipot,loop
      common /info2/ delE(3),atfrac(3),ipot,loop
      open(unit=1,status='NEW',file=fileout)
      delY=0.000000E+00
```

```
      write(1,1010) label       ! plot label
      write(1,1020)             ! x-axis label
      write(1,1030)             ! y-axis label
      write(1,1040)             ! fitting parameters (connect points)
      do 100 i=1,loop/10
        E=delE(ion)*10.0*float(i)/1000.0
        write(1,1050) E,Y(I*10),delY
100   continue
      close(unit=1)
      write(6,1000) fileout
1000  format(' Fusion Profile saved in file  :  ',A30)
1010  format(' ',A30)
1020  format(' Ion Energy (keV)')
1030  format(' Fusion Yield')
1040  format(12X,'9',11X,'1',/,'  0.0000000000000000E+00',/,
     +         11X,'0',/,11X,'0')
1050  format(1X,1PG14.6,',',1PG14.6,',',1PG14.6)
      return
      end
```